

The Electrochemistry of Organic Nanoparticles

A thesis submitted for the degree of

Doctor of Philosophy

in Physical & Theoretical Chemistry

Xiaofei ZHOU

St Cross College

Hilary Term 2016

Contents

Abstract ..... **v**

Acknowledgement ..... **vi**

List of Publications ..... **viii**

Glossary ..... **ix**

Chapter 1 Fundamentals of Electrochemistry **1**

1.1 Equilibrium Electrochemistry 1

1.2 Dynamic Electrochemistry 3

1.2.1 Electrode Kinetics 4

1.2.2 Mass Transport 6

1.3 The Electrical Double Layer 10

1.4 The Electrochemical Cell 12

1.4.1 Working Electrodes 15

1.4.2 Reference Electrodes 16

1.4.3 Counter Electrodes 17

1.5 Electrochemical Techniques 18

1.5.1 Cyclic Voltammetry 18

1.5.2 Chronoamperometry 24

References 28

Chapter 2 Nanoparticles and Existing Technologies **31**

2.1 Synthesis of Organic Nanoparticles 32

2.2 The Modification of Electrodes 34

2.2.1 Drop Casting Techniques 34

2.2.2 “Sticky Electrodes” 35

2.3 Stripping Voltammetry 37

2.4 Nano-impacts 39

2.5 Characterization of Nanoparticles 46

2.5.1 Scanning Electron Microscopy 46

2.5.2 Dynamic Light Scattering 48

2.5.3 Nanoparticle Tracking Analysis 50

2.5.4 Ultraviolet-visible Spectroscopy 51

References 52

Chapter 3 Electrochemical Sizing of Monomeric Organic Nanoparticles 58

3.1 Introduction 59

3.2 Experimental Section 60
3.2.1 Chemicals and Materials 60
3.2.2 Synthesis of Indigo Nanoparticles 61
3.2.3 Characterisation of Indigo Nanoparticles 61
3.2.4 Cyclic Voltammetry of Indigo Nanoparticles 62
3.2.5 Electrochemical Sizing of Indigo Nanoparticles 62

3.3 Results and Discussion 63
3.3.1 DLS Characterization of Indigo Nanoparticles 63
3.3.2 Cyclic Voltammetry of Indigo Nanoparticles 64
3.3.3 Electrochemical Sizing of Indigo Nanoparticles 65

3.4 Conclusions 70

References 72

Chapter 4 Electrochemical Detection and Characterization of Polymeric Nanoparticles 74

4.1 Introduction 75

4.2 Experimental Section 76
4.2.1 Chemicals and Materials 76
4.2.2 Synthesis of PVK Nanoparticles 77
4.2.3 Characterization of PVK Nanoparticles 78
4.2.4 Electrochemical Characterization of PVK Nanoparticles 78
4.2.5 PVK Nanoparticle Sticking 79
4.2.6 PVK Nanoparticle Sensing in Aqueous Solution 79

4.3 Results and Discussion 79
4.3.1 NTA Characterisation of PVK Nanoparticles 79
4.3.2 Determination of Electrons Transfer to Poly (N-vinylcarbazole) Nanoparticles 80
4.3.3 Detection of Organic Poly (N-vinylcarbazole) Nanoparticles Using the Sticking and Sensing Method 84

4.4 Conclusions 87

References 88

Chapter 5 Doping of Single Polymeric Nanoparticles 90

5.1 Introduction 91

5.2 Experimental Section 92
5.2.1Chemicals and Materials 92
5.2.2 Synthesis of PVK Nanoparticles 92
5.2.3 Characterization of PVK Nanoparticles 92
5.2.4 Cyclic Voltammetry of PVK Nanoparticles 93
5.2.5 Nano-impacts of PVK Nanoparticles 93

5.3 Results and discussion 94
5.3.1 DLS Characterisation of PVK Nanoparticles 94
5.3.2 Cyclic Voltammetry of PVK Nanoparticles 95
5.3.3 Doping of Single PVK Nanoparticles 97

5.4 Conclusions 101

References 103

Chapter 6 Electrochemistry and Nano-impacts of Bifunctional Organic Nanoparticles 105

6.1 Introduction 106

6.2 Experimental Section 107
6.2.1 Chemicals and Materials 107
6.2.2 Synthesis of OBD Nanoparticles 107
6.2.3 Characterization of OBD Nanoparticles 108
6.2.4 Cyclic Voltammetry of OBD in Organic Solvent 108
6.2.5 Cyclic Voltammetry of OBD Nanoparticles in Aqueous Solution 108
6.2.6 Nano-impacts of OBD Nanoparticles 109

6.3 Results and Discussion 109
6.3.1 Electrochemical Characterization of Molecular OBD Dissolved in Acetonitrile 110
6.3.2 Electrochemical Characterization of OBD Nanoparticles in Aqueous Solution 114
6.3.3 Nano-impacts of OBD Nanoparticles 116
6.3.4 Electrochemical Sizing and DLS Sizing of OBD Nanoparticles 120

6.4 Conclusions 121

References 123

Chapter 7 Contrasts between Single Nanoparticle and Ensemble Electron Transfer: The Oxidation and Reduction of DPPH Nanoparticles in Aqueous Media.....125

7.1 Introduction.....126

7.2 Experimental Section.....129
7.2.1 Chemicals and Materials.....129
7.2.2 UV-Vis Spectroscopy.....129
7.2.3 Synthesis of DPPH Nanoparticles.....129
7.2.4 Characterisation of DPPH Nanoparticles.....130
7.2.5 Cyclic Voltammetry of Molecular DPPH in Organic Solvent.....130
7.2.6 Cyclic Voltammetry of DPPH Nanoparticles in Aqueous Solution.....131
7.2.7 Nano-impacts of DPPH Nanoparticles.....131

7.3 Results and Discussion.....132
7.3.1 UV-Vis Spectroscopy of DPPH in Acetone.....132
7.3.2 Electrochemistry of DPPH in Acetonitrile/TBAP.....133
7.3.3 Electrochemical Characterization of DPPH Nanoparticles Drop Cast on an Electrode Surface.....137
7.3.4 Nano-impacts of DPPH nanoparticles.....144

7.4 Conclusions.....154

References.....155

Chapter 8 Ion Insertion into Individual 7,7,8,8-Tetracyanoquinodimethane (TCNQ) Nanoparticles.....159

8.1 Introduction.....160

8.2 Experimental.....162
8.2.1 Chemicals and Materials.....162
8.2.2 Synthesis of TCNQ Nanoparticles.....162
8.2.3 Characterisation of TCNQ Nanoparticles.....163
8.2.4 Cyclic Voltammetry of TCNQ Nanoparticles.....163
8.2.5 Ion Insertion into Single TCNQ Nanoparticles.....164

8.3 Results and Discussion.....164
8.3.1 DLS measurements of TCNQ Nanoparticles.....165
8.3.2 SEM measurements of TCNQ Nanoparticles.....165
8.3.3 Cyclic Voltammograms of Ensembles of TCNQ Nanoparticles.....168
8.3.4 Nano-impacts of individual TCNQ nanoparticles.....173
8.3.5 Quantification of Potassium and Sodium Insertion into Individual TCNQ Nanoparticles.....176

8.4 Conclusions.....181

References.....183

Chapter 9 Overall Conclusions.....186

Abstract

This thesis presents the experimental work with the main aim of developing a new approach for the study and characterization of organic nanoparticles by using electrochemical method in aqueous solution.

The first chapter introduces the principles and techniques of electrochemistry while the second chapter gives a brief introduction to the synthesis of organic nanoparticles, the modification of electrodes and the monitor of organic nanoparticles via electrochemical and existing characterization techniques.

This thesis reports the experimental work on detecting a variety of organic nanoparticles synthesized by reprecipitation method via two main electrochemical methods. For stripping voltammetry, the reduction/oxidation potential of organic nanoparticles in aqueous solution was obtained and the number of electrons transferred was quantified by analytical expressions for reductive/oxidative peaks. For the novel electrochemical method "nano-impacts", a suitable potentiostatted electrode is immersed in an organic nanoparticles solution so that reduction/ oxidation of a single organic nanoparticle upon its collision on the surface of the electrode. It is shown that this method is capable to characterize the size of monomeric organic nanoparticles and bifunctional organic nanoparticles, the doping of polymeric nanoparticles and the ion-insertion of individual organic nanoparticles. Sticking and stripping technique was also successfully applied to quantify and immobilize the polymeric nanoparticles in aqueous solution.

Acknowledgement

First, I would like to express my special appreciation and thanks to my supervisor, Professor Richard G. Compton, for taking me on as a DPhil student in his research group. You have been a tremendous mentor offering priceless help and guidance and advice on both research and career development to me. I will never forget the speech you gave to celebrate my Chinese Outstanding Student Award in Chinese Embassy, which encouraged and inspired me during my time here in Oxford. I also thank Professor Zhengwen Fu in who introduced me to the electrochemistry world beyond the lithium battery and encouraged me in Fudan University. I would not have found my way of research and study in the University of Oxford without you.

Thank you to all the past and present group members of the Compton group for making the group a family. In particular, thanks to Dr. Wei Cheng for his helpful consultation and stimulating discussion for my research. You are more like an elder brother rather than a partner for giving guidance and helping with my writing. Thank you to Dr. Christopher Batchelor-McAuley and Prof. Kristina Tschulik for giving me immeasurable support during my first year and training me on various experimental techniques. To Dr. Lior Sepunaru and Dr. Sven Ernst, thank you for spending the free time talking and breathing the fresh air with me. Thank you the other members of my year group, Peilin, Patty, Hershuang and Rita, with whom I have shared this precious experience over the past three years. I will draw a perfect full stop for our five. To Qian, Lin, Ying, Emma, Ivana, Shaltiel, Crystal, Enno, Blake, Kenichi, Xiuting, Chuhong, Stan, Mendy and other members of the group, thank you all for the memorable lunches, dinners, parties, laughers

and never ending support. I missed the days when we met out of working hours in the lab or office and saying ‘you are still here!’

To Dr. Kerstin Jurkschat and Dr. Chris Salter, thank you for giving instructions and providing guidance with NTA, DLS and SEM measurements.

I am also very grateful to my college, St Cross College, who has provided me a home, lots of dinners and training opportunities. Thank you to Dr. Dave Waters, my college senior tutor, for taking care of me and providing me significant career advice.

I also wish to give special thanks to my dear friends, Juliane, Chuang, Jian, Yu, Zhongzhen, Hanwen, Hongjia and OxNB for their generous support and treasured friendship. Thanks to all other friends blooming during my three years life in Oxford.

Last but not least, I would like to say thank you to my family for their love, care, encouragement and support through all these years. Your help and understanding are most important to me.

List of Publications

The publications are listed in chronological order.

Electrochemical Sizing of Organic Nanoparticles

W Cheng, XF Zhou, RG Compton, *Angewandte Chemie International Edition*, 52, (2013), 12980-12982.

Electrochemical Detection and Characterisation of Polymer Nanoparticles

XF Zhou, W Cheng, C Batchelor-McAuley, K Tschulik, RG Compton, *Electroanalysis*, 26, (2014), 248-253.

Nano-impacts of Bifunctional Organic Nanoparticles

XF Zhou, W Cheng, RG Compton, *Nanoscale*, 6, (2014), 6873-6878.

Doping of Single Polymeric Nanoparticles

XF Zhou, W Cheng, RG Compton, *Angewandte Chemie, International Edition*, 53, (2014), 12587-12589.

Contrasts between Single Nanoparticle and Ensemble Electron Transfer: Oxidation and Reduction of DPPH Nanoparticles in Aqueous Media

XF Zhou, W Cheng, RG Compton, *ChemElectroChem* 2, (2015): 691-699.

Ion Insertion into Individual 7, 7, 8, 8-Tetracyanoquinodimethane Nanoparticles

XF Zhou, W Cheng, RG Compton, *Nanoscale* 7, (2015): 15719-15726.

Glossary

Roman Symbols

Symbol	Definition	Units
A	Area	m^2
A_r	Relative atomic mass	
C	Concentration	mol m^{-3}
C_{OBD}	Concentration of OBD in acetonitrile	mol m^{-3}
C_{DPPH}	Concentration of DPPH in acetonitrile	mol m^{-3}
D	Diffusion coefficient	m^2 s^{-1}
D_{np}	Diameter of nanoparticle	m
E	Equilibrium potential	V
e	Electric charge (1.6×10^{-19})	C
E^0	Standard electrode potential	V
E_f^0	Formal potential	V
F	Faraday constant, (96485)	C mol^{-1}
I	Current	A
I_P	Peak current	A
I_{ss}	Steady-state current	A
j	Faradaic flux	mol m^{-2} s^{-1}
j_d	Diffusional flux	mol m^{-2} s^{-1}

j_m	Migratory flux	mol m^{-2} s^{-1}
k^0	Standard electrochemical rate constant	
k_B	Boltzmann constant (1.38×10^{-23})	J K^{-1}
k_{ox}	Rate constant for the oxidation reaction	cm s^{-1}
k_{red}	Rate constant for the reduction reaction	cm s^{-1}
M	Molar mass	kg mol^{-1}
$M_{surface}$	Amount of substance reacting on the surface of the electrode	mol
n	Number of particles	
Q	Charge	C
R	Gas constant (8.314)	J K^{-1} mol^{-1}
r_e	Radius of electrode	m
r_f	Average final particle radius	m
r_i	Average initial particle radius	m
r_{np}	Radius of nanoparticle	m
R_s	Electrical resistance of bulk solution	Ω
S	Surface coverage of the electrode	
T	Temperature	K
t	Time	s
t_k	Thickness of ion insertion	m
ν	Velocity	m s^{-1}

Greek Symbols

Symbol	Definition	Units
α	Transfer coefficient	
γ	Activity coefficient	
η	Viscosity	kg m^{-1} s^{-1}
λ	Wavelength	m
v	Scan rate	mV s^{-1}
ρ	Density	kg m^{-3}
ϕ	Electrostatic potential	V

Abbreviations

Abbreviation	Definition
APC	Anodic particle coulometry
CV	Cyclic voltammetry
DLS	Dynamic light scattering
DPPH	2-diphenyl-1-picrylhydrazyl
GC	Glassy carbon
IHP	Inner Helmholtz Plane
NMP	N-Methyl-2-pyrrolidone
NPs	Nanoparticles
NTA	Nanoparticles tracking analysis

NTP	1,4-nitrothiophenol
OBD	Oil Blue N Dye/Solvent Blue 14
OHP	Outer Helmholtz plane
PBS	Phosphate-buffered saline
PDDP	1-phenyl-3-((dimethylamino)styryl)-5-((dimethylamino)phenyl)-2-pyrazoline
PVK	Poly(N-vinylcarbazole)
SCE	Saturated calomel electrode
SEM	Scanning electron microscopy
TBAP	Tetra-n-butylammonium perchlorate
TCNQ	7,7,8,8-Tetracyanoquinodimethane
THF	Tetrahydrofuran
UV-Vis	Ultraviolet-visible

Chapter 1

Fundamentals of Electrochemistry

This thesis is concerned about using electrochemical methods to detect and characterize organic nanoparticles. This chapter provides an introduction to the fundamental understanding of electrochemical behaviour and the theories which are used in the study of electrochemical reactions. In order to develop the following electrochemical discussion, it is essential to first introduce the concept of equilibrium electrochemistry. This will be followed by electrochemical kinetics and mass transport. An overall of electrochemical cell and electrochemical techniques will also be established. More detailed information of the fundamental of electrochemistry may be found in the books of Compton[1], Bard and Faulkner[2] , Brett and Brett[3], Fisher[4], Scholz[5] and Rieger[6].

1.1 Equilibrium Electrochemistry

Electrochemical equilibrium reflects a balance between chemical energies and electrical energies in electrochemical reactions. A simple reaction involving the transfer of charge across the interface between an electrode (m) and an electrolyte (aq) can be given as:

$$O_{(aq)} + e^-_{(m)} \rightleftharpoons R_{(aq)} \qquad \text{(Eqn.1.1)}$$

in which O and R are the species in solution phase and one electron is assumed to be transferred. When the oxidized and reduced species in an electrode reaction are at

equilibrium at the electrode surface, the Nernst equation can be applied with the potentials as established by

$$E = E^0 + \frac{RT}{F}\ln\left(\frac{a_o}{a_R}\right) \quad \text{(Eqn.1.2)}$$

where E is the equilibrium potential (V), E^0 is the standard electrode potential, R is the gas constant, T is the absolute temperature, F is the Faraday constant (96485 C mol^{-1}) and a_o and a_R are the activities of species involved in the charge transfer reaction.

Under practical circumstances, however, it is more convenient to express the Nernst equation by using surface concentration of O and R rather than activities. The Nernst equation then is given by

$$E = E_f^0 + \frac{RT}{F}\ln\left(\frac{[O]}{[R]}\right) \quad \text{(Eqn.1.3)}$$

where the E_f^0 is the formal potential, $[O]$ and $[R]$ are the surface concentration of O and R and there exists:

$$E_f^0 = E^0 + \frac{RT}{F}\ln\left(\frac{\gamma_O}{\gamma_R}\right) \quad \text{(Eqn.1.4)}$$

where γ_O and γ_R are the activity coefficients of O and R such that $a_o = \gamma_O[O]$ and $a_R = \gamma_R[R]$. Note that E must be measured relative to a reference electrode and that the standard

hydrogen electrode is assigned, by definition, a standard potential at 0V. (See also section 1.4)

1.2 Dynamic Electrochemistry

For a general one-electron redox electrochemical reaction as shown in Eqn. 1.5,

$$O_{(aq)} + e^-_{(m)} \underset{k_{ox}}{\overset{k_{red}}{\rightleftharpoons}} R_{(aq)} \qquad \text{(Eqn.1.5)}$$

the current (I) can be quantified by Faraday's Law by

$$I = FAj \qquad \text{(Eqn.1.6)}$$

where A is the area of the electrode and j is the Faradaic flux at the electrode surface. The currents for the oxidative and reductive components may be described by

$$I_c = FAk_{red}[O]_0 \qquad \text{(Eqn.1.7)}$$

$$I_a = FAk_{ox}[R]_0 \qquad \text{(Eqn.1.8)}$$

where k_{red} and k_{ox} are the heterogeneous rate constants for reduction and oxidation respectively and $[O]_0$ and $[R]_0$ denote the concentrations at the electrode surface. Then the Eqn. 1.6 can be written as

$$I = I_c - I_a \qquad \text{(Eqn.1.9)}$$

Therefore

$$I = FA(k_{red}[O] - k_{ox}[R]) \quad \text{(Eqn.1.10)}$$

1.2.1 Electrode Kinetics

This section introduces theory to understand the rate of electron transfer between the electrode surface and species in solution. It is generally considered that the electron transfer kinetics can be parameterised via the Butler-Volmer model. For a one-electron transfer reaction, the rate constants for the oxidation and reduction can be expressed as:

$$k_{red} = k^0 \exp\left[\frac{-\alpha F}{RT}\left(E - E_f^0\right)\right] \quad \text{(Eqn.1.11)}$$

$$k_{ox} = k^0 \exp\left[\frac{(1-\alpha)F}{RT}\left(E - E_f^0\right)\right] \quad \text{(Eqn.1.12)}$$

where k^0 is the standard electrochemical rate constant (cm s^{-1}), α is the transfer coefficient and $(E - E_f^0)$ is the overpotential. Then the relationship between the current response and potential difference can be described as:

$$I = FAk^0\left\{[\mathrm{O}]_0 \exp\left[\frac{-\alpha F}{RT}\left(E - E_f^0\right)\right] - [R]_0 \exp\left[\frac{(1-\alpha)F}{RT}\left(E - E_f^0\right)\right]\right\} \quad \text{(Eqn.1.13)}$$

The Butler-Volmer equation was developed by two electrochemists, Butler[7] (1924) and Volmer[8] (1930). They independently arrived at its formulation which was verified by experimental test independently. It is fundamental and vitally important to electrode

kinetics representing how the observed current is influenced by the overpotential and the transfer coefficient.

From Eqn.1.13, it can be seen that under extreme potentials, such as $E \gg E_f^0$ or $E \ll E_f^0$, the first or second term within the brackets can be neglected. For a case of reductive electrochemical process, the Butler-Volmer equation can be written as

$$I_{red} = I_0 \exp\left[\frac{-\alpha F}{RT}\left(E - E_f^0\right)\right] \quad \text{(Eqn.1.14)}$$

Then the equation simplifies to

$$\ln|I_{red}| = \frac{-\alpha FE}{RT} + constant \quad \text{(Eqn.1.15)}$$

assuming no concentration depletion effects at the electrode.

For an oxidation, similarly

$$I_{ox} = I_0 \exp\left[\frac{(1-\alpha)F}{RT}\left(E - E_f^0\right)\right] \quad \text{(Eqn.1.16)}$$

$$\ln|I_{ox}| = \frac{(1-\alpha)FE}{RT} + constant \quad \text{(Eqn.1.17)}$$

I_{red} and I_{ox} are the reduction and oxidation currents respectively and I_0 is the exchange current. The plots of $\ln|I_{red}|$ against E or $\ln|I_{ox}|$ against E are so called Tafel plots[1], which can used to calculate the transfer coefficient α.

1.2.2 Mass Transport

Section 1.2.1 discussed the rate of an electron transfer reaction at the interface between electrode and solution. However, under conditions of electrolysis, it is obvious that the composition of solution at the interface is different from that in bulk solution. The active species need to be transported from bulk solution to the electrode interface and then the products diffuse away after being formed as shown in Figure 1.1.

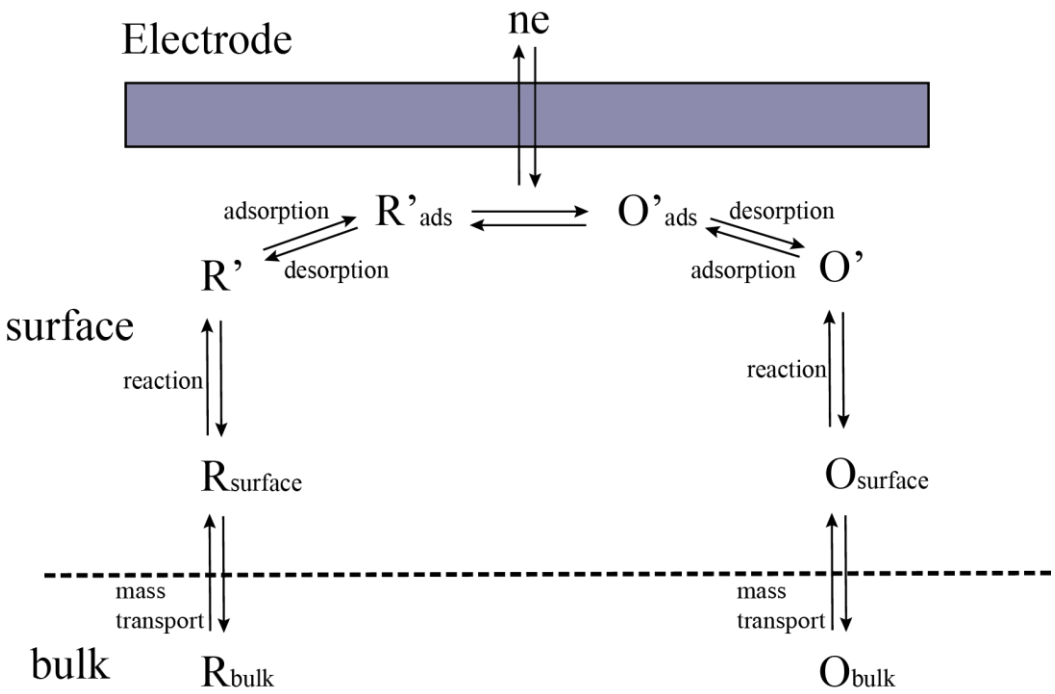


Figure 1.1 Schematic pathway of a general electrode reaction

Thus, the overall kinetics will not only depend on the rate of electron transfer, but will also be controlled by the rate of mass transport. There are three forms of mass transport, namely: diffusion, convection and migration, each of which will be discussed in more detail below.

1.2.2.1 Diffusion

Diffusion is the spontaneous movement of species driven by a concentration gradient of chemical potential, as a consequence of reactant consumption and product formation at the electrode surface[5]. The flux at a distance, x, from the electrode surface can be quantified by Fick's first law[9]

$$j_d = -D\frac{\partial c}{\partial x} \qquad \text{(Eqn.1.18)}$$

where j_d is the diffusional flux, $\frac{\partial c}{\partial x}$ is the concentration gradient in the x direction and D is the diffusion coefficient. D describes the ease with which a species can move from higher concentration to lower concentration through solution, which can be defined as:

$$D = \frac{(\delta x)^2}{2\delta t} \qquad \text{(Eqn.1.19)}$$

where δt is the time taken for the species to move a mean square distance $(\delta x)^2$. Eqn.1.19 was introduced by Einstein[10].

Fick's second law[9] gives the variation of concentration as a function of time, shown as

$$\frac{\partial c}{\partial t} = D\frac{\partial^2 c}{\partial x^2} \quad \text{(Eqn.1.20)}$$

If more than one direction needs to be considered, the equation must be extended to describe transport in each direction. Specifically in three directions:

$$\frac{\partial c}{\partial t} = D\frac{\partial^2 c}{\partial x^2} + D\frac{\partial^2 c}{\partial y^2} + D\frac{\partial^2 c}{\partial z^2} \quad \text{(Eqn.1.21)}$$

1.2.2.2 Convection

Convection is defined as a movement of a species with fluid flow when an external force acts on a solution. There are two types of convection[2]. Natural convection arising from thermal or density gradient within the solution exists in any circumstance. The effects of natural convection are generally undesirable due to the unpredictable and irreproducible results on the observed current, but it becomes significant only when the timescale of experiments is long. Consequently, all experiments at macroelectrodes are limited to a period of 10-20 seconds[1].

The second type is forced convection, which originates from mechanical forces such as bubbling, pumping or stirring. The flow of forced convection is generally of a magnitude much larger than natural convection. The flux j_c due to convection is given by

$$j_c = cv_x \quad \text{(Eqn.1.22)}$$

where c is the bulk concentration and v_x is the solution velocity in the x direction.

Forced convection can be deliberately introduced into experimental system to eliminate uncontrolled effects allowing better quantitative analysis. Such an approach is applied in rotating disc electrodes[11], flow cells[12] and in sonoelectrochemistry[13].

1.2.2.3 Migration

Migration is the movement of a charged species driven by a potential gradient. The external electric field at the electrode/solution interface results from drop in electrical potential between the two phases. It exerts a force on charged species thereby inducing movement of ions from or to the electrode. The migratory flux is defined as[4]

$$j_m = -\frac{zF}{RT} Dc \frac{\partial \phi}{\partial x} \qquad \text{(Eqn.1.23)}$$

where z is the charge on the electroactive species, c is the concentration and $\frac{\partial \phi}{\partial x}$ is the gradient of electric field in the x-dimension.

In order to minimise the effects of migration, a high concentration of supporting electrolyte (much larger than that of electroactive species) is typically added to the solution to act as an ionic charge carrier[4]. The current of electrons through the external circuit can be balanced by the passage of supporting electrolyte ions through the solution from or to the electrodes, and a minimal amount of the electroactive species will be transported by migration. Apart from this, the supporting electrolyte also compresses the

electrical double layer (will be discussed in Section 1.4) to 10-20Å[1], which is compatible with electron quantum mechanical tunnelling between the electrode and the species in the phase. However, there are also some drawbacks of adding supporting electrolyte such as increasing ion-pairing and causing adsorption on the surface of the electrode, which have the kinetic and thermodynamic implication[2].

In this thesis, migration and convection are minimised and it is assumed that in all experiments the mass transport is diffusion controlled.

1.3 The Electrical Double Layer

There are two types of processes of reactions: Faradaic process and non-Faradaic process. All the electrochemical reactions discussed in section 1.2 are Faradaic, while a non-Faradaic process is the one in which there is no charge transfer across an interface but is instead caused by interfacial capacitance[2]. This is relevant because the effect of capacitance can interfere with measurements of kinetic and transport properties. On the positive side, the study of non-Faradaic currents that comes from capacitative charging of electrical double layer is a promising area for applications in energy storage[14-16].

The electrical double layer is formed at the interface between an electrode and a solution. When an electrode was immersed into a solution, a potential difference can be built up at the interface as a result of different energy levels in the electrode and in solution. Ions with same charge are repelled by the electrode and ions with opposite charge are attracted to the surface, thereby an electric field gradient is formed between the electrode and the bulk solution.

There have been several models and improvement proposed to describe the electrical double layer. In 1853, Helmholtz[17] first proposed that the double layer is formed as two layers of opposite charges on each side of the interface. The plane of the region was defined as the outer Helmholtz plane (OHP), which passed through the centre of the absorbed ions located at a minimum distance from the electrode surface. The potential followed a linear sharp drop between the surface and OHP. Then a model was developed by Gouy[18] and Chapman[19] independently, indicating that the capacitance is not a constant but is determined by the applied potential and ion concentration in solution. Their model concluded the existence of a 'diffuse layer' of charge distribution of ions and the potential decreased approximately exponentially from the surface to the bulk solution. Stern[20] improved his approach later by considering the ions to have a minimum distance of approach (OHP) and combined this with the accepted idea of the diffuse layer. He proposed that a sharp drop of potential exists between the electrode and the OHP and then the potential gradually decreases to the bulk solution.

In 1947 Grahame[21, 22] reported that it may be possible for some ionic or uncharged species to be absorbed on the surface of the electrode. This could occur if ions lose their solvation shell as they approach the electrode. The model thus predicts the existence of three regions with a new closer plane named the Inner Helmholtz Plane (IHP) which passes though the centre of the 'specifically adsorbed' ions. Figure 1.2 shows a schematic diagram of the double layer region and the decay of the electrostatic potential predicted by this model.

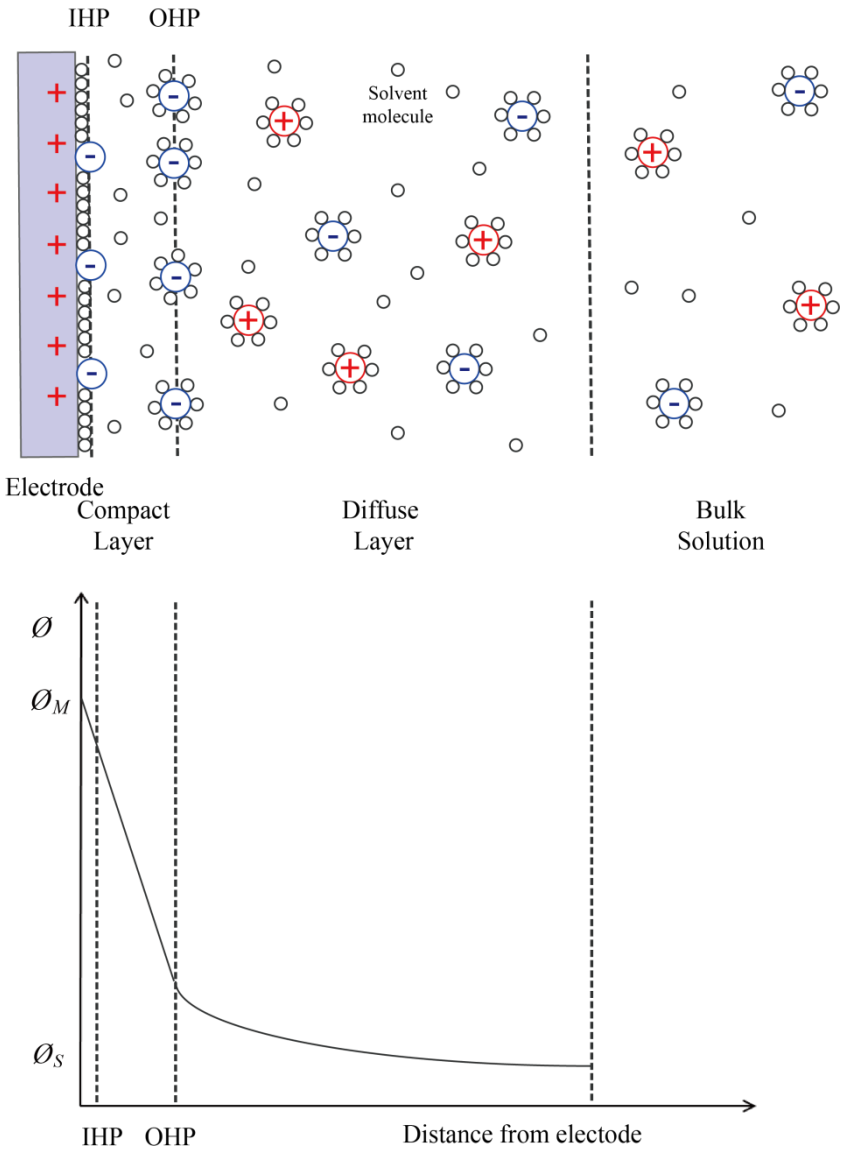


Figure 1.2 Schematic diagrams showing the Grahame model of the electrical double layer

1.4 The Electrochemical Cell

It is impossible to measure or control the difference of potential between a single electrode and a solution. We can, however, detect the potential difference between two electrodes immersed in a same solution. In order to apply a controlled potential drop at a single

interface, a power supply can be used between the two electrodes and a solution is used to form a closed circuit. The electrode with the interface of interest is termed the 'working electrode' (WE), while the second electrode, termed the 'reference electrode', acts as the other half of the cell which must maintain a fixed potential to gauge the potential of working electrode. The potential difference E_{diff} then can be described as:

$$E_{diff} = (\phi_M - \phi_S)_{working} - (\phi_M - \phi_S)_{reference} - IR_S \qquad \text{(Eqn.1.24)}$$

where ϕ_M and ϕ_S are the electrical potentials of the electrode and solution phases respectively. I is the current passed and R_S is the electrical resistance of the bulk solution which is defined by Ohm's Law. It can be reduced by locating the electrodes close to each other. However, if a significant current is passed, electrolysis occurs and the potential of reference electrode is no longer a constant, moreover, the IR_S term contributes in an essentially unknown manner to Eqn.1.24.

To solve this problem, a third electrode is employed as 'counter electrode'. Figure 1.3 gives an illustration of an experimental setup of a three electrode system. The electrodes are termed the working electrode, the reference electrode and the counter electrode from left to right. In the classical three electrode system, current is passed between the working electrode and the counter electrode but no current is passed through the reference electrode. In this way a stable constant reference potential can be maintained.

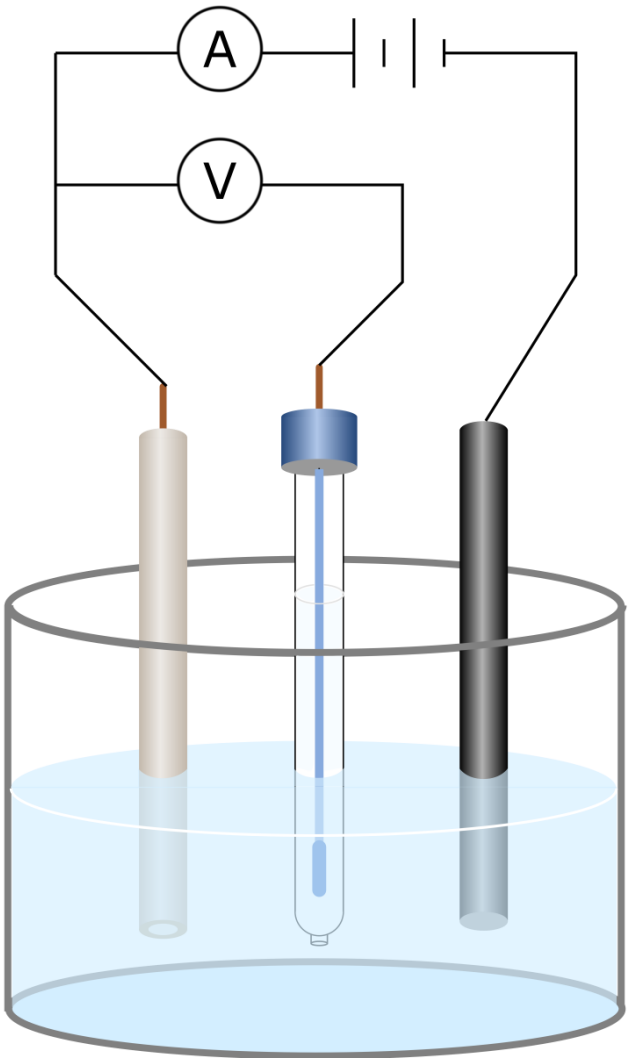


Figure 1.3 Schematic diagram of a three electrode setup. Electrodes from left to right: working electrode, reference electrode and counter electrode

In this thesis, all electrochemical experiments are using a three electrode system with a potentiostat applied to impose a potential difference between the working electrode and the reference electrode and which follows by recording the current signal as a function of the applied potential.

1.4.1 Working Electrodes

The working electrode plays the most important role in an electrochemical system. It is on the working electrode that electron transfer reactions of interest occur. The selection of a working electrode depends on two main factors. First of all, the material of the working electrode should have a performance with the analyte with favourable redox behaviour and which gives a reproducible result without any chemical reactions between the material and the solution phase. Secondly, the potential window of the intended analyte on the electrode in a given electrolyte needs to be appropriately wide. In electrochemical experiments, working electrodes such made of gold, silver, platinum, carbon and mercury are commonly used. The types of working electrode can be classified in terms of geometry such as disk electrode, rotating disk electrode[23, 24] etc.

The concentration difference between the vicinity of an electrode and the bulk solution results in diffusion and forms a diffusion layer around an electrode. Both macro- and micro-disc electrode are employed in electrochemical experiments in this thesis. The diffusion behaviour at macroelectrodes and microelectrodes are different leading to different electrochemical responses in voltammograms. The mass transport is mainly attributed to linear diffusion at a macroelectrode, while convergent diffusion dominates for a microelectrode as shown in Figure 1.4[1]. The convergent diffusion contributes more as the radius of the electrode decreases; as a result, a microelectrode has more sufficient diffusion transport than the macroelectrode. The difference in the electrochemical behaviour of macroelectrodes and microelectrodes will be introduced in more detail in Section 1.5.

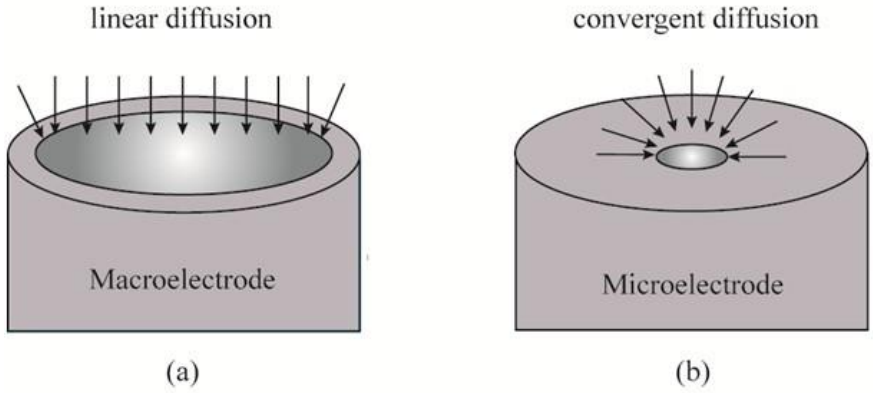


Figure 1.4 The difference of mass transport modes at a macroelectrode and a microelectrode

1.4.2 Reference Electrodes

As mentioned above, a reference electrode should provide a fixed potential so that it can be used to monitor the potential difference at the working electrode. It should have a relative stable and reproducible potential value over time and with temperature changing. Commonly used reference electrodes are the standard hydrogen electrode (SHE), the saturated calomel electrode (SCE) and the silver-silver chloride electrode (Ag/AgCl).

The SCE is employed for the electrochemical experiments in this thesis. A SCE is a half-cell which consists of a paste of mercurous chloride (Hg_2Cl_2, calomel) and a pool of mercury immersed into a saturated potassium chloride (KCl) solution. The saturated KCl solution contains solid KCl, which keeps the chloride ion concentration constant. A platinum wire is used to electrically contact the system to the external circuit. A schematic diagram of a SCE is shown in Figure 1.5 and the half-cell reaction is:

$$Hg_2Cl_2(s) + 2e^- \leftrightarrow 2Hg(l) + 2Cl^- \qquad \text{(Eqn.1.25)}$$

with an E^0value of +0.244 V at 298K.

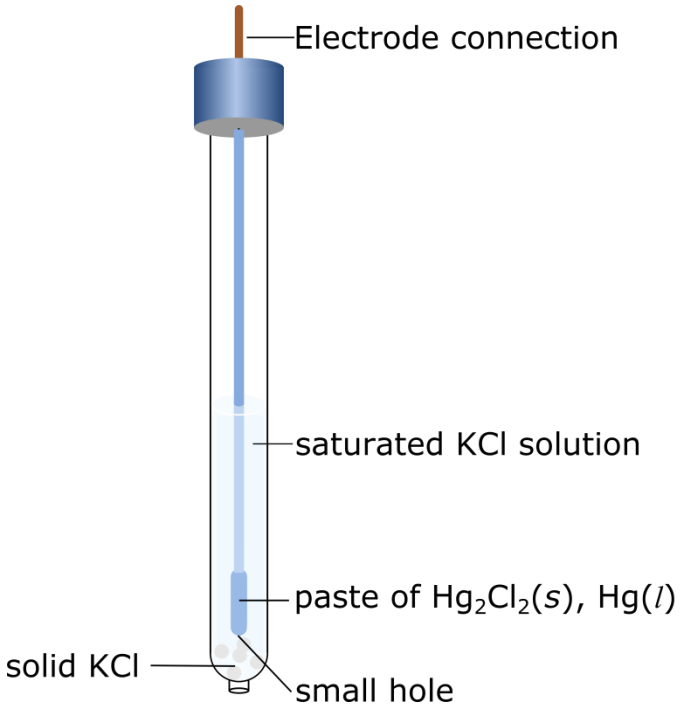


Figure 1.5 Schematic diagram of a saturated calomel electrode (SCE)

1.4.3 Counter Electrodes

The purpose of the counter electrode is to allow the current to flow as induced by the potential applied to the working electrode. It is common that the counter electrode is made of a relative inert material such as platinum, gold or carbon so as to minimise its chemical effects on the reaction at the working electrode. It is preferable that the surface area of the counter electrode is ca. ten times larger than that of the working electrode to avoid limitations of the applied potentials.

1.5 Electrochemical Techniques

In the previous section, the design of an electrochemical cell and the functions of the different electrodes were discussed that are necessary to control the applied potential and detect the current correctly. Once a suitable potential is applied, plots of currents against potential can give a response of a reductive or an oxidative reaction during using electrochemical techniques such as cyclic voltammetry and chronoamperometry. Both of these will be introduced below.

1.5.1 Cyclic Voltammetry

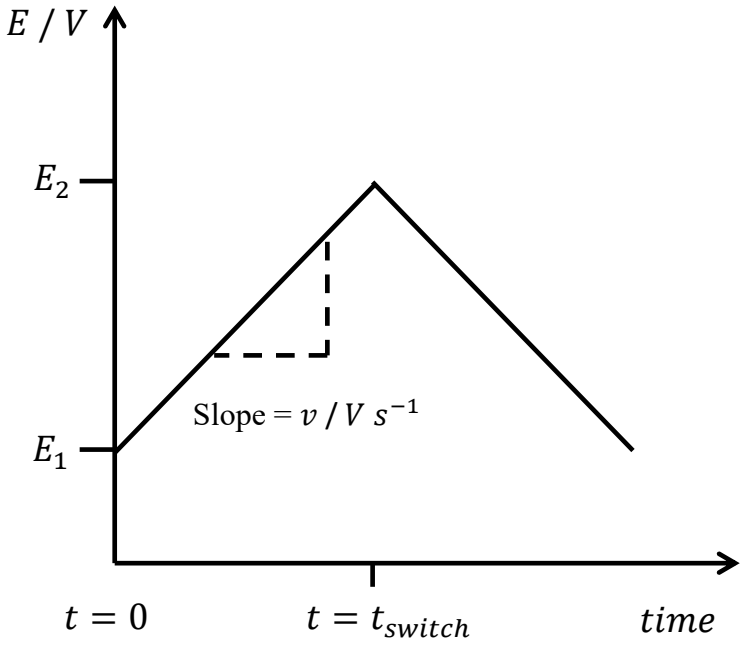


Figure 1.6 The potential waveform applied to the working electrode in the cyclic voltammetry experiment.

In cyclic voltammetry, the current is recorded as a function of potential. The potential is scanned linearly from a starting potential E_1 which usually corresponds to zero current flow to a second potential E_2 and is then reversed back to starting point E_1 at a fixed scan rate. The second potential E_2 is always sufficiently set so that the interval (E_2-E_1) contains the oxidation or reduction process of interest. The triangular waveform of cyclic voltammetry is shown in Figure 1.6, where t_{switch} refers to the time at which the potential applied is reversed.

Cyclic voltammetry is the most important and widely used method of voltammetry[3, 25], and can provide electrochemical kinetics and diffusion parameters. It is often employed first in electrochemical experiments and gives direct information such as the formal potentials of species in redox electrochemical reactions. However, the electroactive species exhibits a different diffusional behaviour depending on the size of the working electrode, resulting in different shapes of the voltammograms. The cyclic voltammetry at both macroelectrodes and microelectrodes is discussed in the next sections.

1.5.1.1 Cyclic voltammetry at macroelectrodes

For a macro disc electrode, the cyclic voltammograms are given in Figure 1.7, in which curves 1, 2 and 3 corresponds to a reversible, a quasi-reversible and an irreversible oxidation electron transfer process respectively. As can be seen from the graph, no faradaic current is passed at low overpotentials ($E << E_f^0$) as the electrode potential is insufficient to convert the reactants: $\mathrm{Red} - e \rightarrow \mathrm{Ox}$. As E increases positively, a near exponential increase in the current is observed, corresponding to the electroactive species

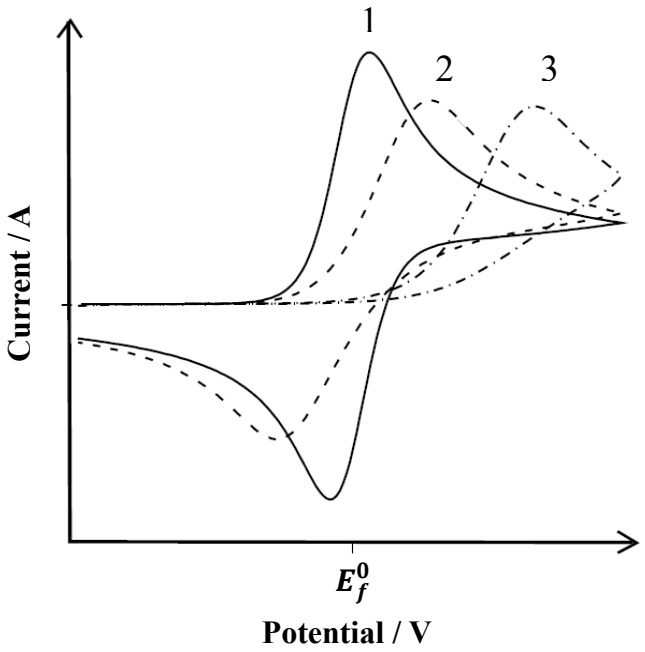


Figure 1.7 Cyclic voltammograms of (1) a reversible, (2) a quasi-reversible and (3) an irreversible system at a macroelectrode

starting to undergo an electrochemical oxidation. In the reversible case, the Nernst equation is employed to describe the electron transfer process[2] and the surface concentrations of Ox/Red are denoted by Eqn. 1.3, while the current increase follows the Butler-Volmer equation in the irreversible case (Eqn.1.13). As the potential continues to grow, the concentration of the reactant become depleted and has to diffuse a larger distance from the bulk solution to the electrode leading to the diffusion layer becoming thicker. Under this circumstance, the current becomes mass transport limited and decreases with the concentration gradient, resulting a peak in the voltammogram. On the reverse scan, a back peak is observed, which is related to the reduction of the oxidized product.

At faster scan rates, the experimental time scale is decreased and the relative rate of mass transport increases, which results in the peak current increasing. Assuming a simple one-electron transfer process, the peak current for a diffusional species is predicted by Randles- Sevcik equation[26, 27] for the reversible limit at 298K:

$$I_P = 2.69 \times 10^5 A D^{\frac{1}{2}} c v^{\frac{1}{2}} \quad \text{(Eqn.1.26)}$$

and for the irreversible limit:

$$I_P = 2.99 \times 10^5 \sqrt{\alpha} A D^{\frac{1}{2}} c v^{\frac{1}{2}} \quad \text{(Eqn.1.27)}$$

where I_P is the peak current, A is the area of the working electrode, D is the diffusion coefficient, c is the concentration of the electroactive species in the bulk solution, v is the scan rate and α is the transfer coefficient. It is noted that the reversible process occurs when electrode transfer is much faster than the rate of mass transport, while in the irreversible process, the electrode kinetics is slower compared with the rate of transport and the electroactive species diffuse away from the interface before equilibrium can be established. As a result, a larger overpotential is required to "drive" the reaction.

The peak to peak separation, defined as the potential difference between the maximal values of the forward and backward peaks, is not zero but is about 59 mV for a reversible one electron process at 25℃. Conversely, for a quasi-reversible or irreversible electrode process, the peak to peak separation is much larger. Assuming the transfer coefficient is

around 0.5, Matsuda and Ayabe[28] interpreted a classification based on the standard electrochemical rate constant, giving a parameter, Λ:

$$\Lambda = \frac{k^0}{\left(\frac{FDv}{RT}\right)^{\frac{1}{2}}} \qquad \text{(Eqn.1.28)}$$

where k^0 is the standard electrochemical rate constant. Matsuda and Ayabe[28] suggested the following ranges for the three types of electrode process at macroelectrodes:

Reversible:

$$\Lambda \geq 15 \qquad k^0 \geq 0.3v^{\frac{1}{2}} \text{ cm s}^{-1}$$

Quasi-reversible:

$$15 > \Lambda > 10^{-3} \qquad 0.3v^{\frac{1}{2}} \text{ cm s}^{-1} > k^0 > 2\times10^{-5}\, v^{\frac{1}{2}} \text{ cm s}^{-1}$$

Irreversible:

$$\Lambda \leq 10^{-3} \qquad k^0 \leq 2\times10^{-5}\, v^{\frac{1}{2}} \text{ cm s}^{-1}$$

where the numbers relate to a temperature of 298K.

1.5.1.2 Cyclic voltammetry at microelectrodes

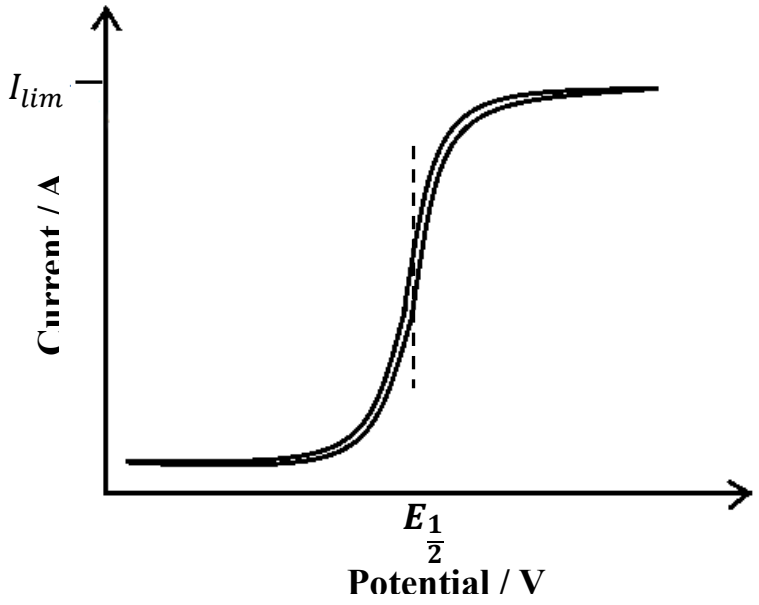


Figure 1.8 A cyclic voltammogram at a microelectrode

As discussed in section 1.4, when the size of the electrode decreases, the diffusional regime will change to convergent diffusion instead of linear diffusion. If a fast scan rate applied to a microelectrode, the shape of the voltammetry seen becomes more similar to that at macroelectrode because of the diffusion to the electrode surface is predominately linear and the diffusion layer is comparatively thin. However, if the time scale is sufficient large (low scan rates), the thickness of the diffusion layer is more significant leading to a convergent diffusion regime. The latter results in a more efficient mass transport since the electroactive species can be drawn not only from above the electrode but also from the side. Then a sigmoidal shaped steady-state voltammogram is established[29] (as shown in Figure 1.8) and the limiting current for a one electron process can be expressed as:

$$I_{lim} = 4FDCr_e \quad \text{(Eqn.1.29)}$$

where I_{lim} is the limiting current (see Figure 1.8), F is the Faraday constant, D is the diffusion coefficient, C is the bulk concentration of the reactant and r_e is the radius of the microelectrode. Another parameter which characterizes the steady-state voltammetry is the 'half-wave potential' $E_{\frac{1}{2}}$, which is the potential where the current is the half of I_{lim}. The half-wave potential is equal to the formal potential if the electron transfer is completely reversible and both the oxidized and reduced species have the same diffusion coefficient. Conversely, it will deviate dramatically for an irreversible redox reaction where the Red/Ox couple has slow electrode kinetics.

1.5.2 Chronoamperometry

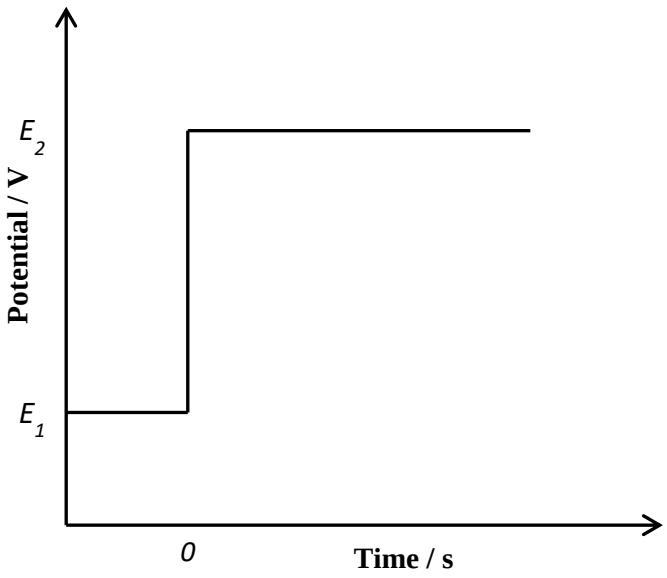


Figure 1.9 The potential-time waveform applied in a chronoamperometry

Chronoamperometric measurement is an electrochemical technique to study the current response when the potential applied to the working electrode is stepped at a certain time. The potential is first held at a known potential E_1 where no electrode reaction occurs and then is stepped to a potential E_2 where the electroactive species can undergo a faradaic process as shown in Figure 1.9. Generally, both of the potentials are chosen in the light of the associated cyclic voltammetry. The current is measured as a function of time. With increased time as electroactive material is depleted the diffusion layer becomes thicker. As a result, the recorded current is larger at the beginning of the experiments, and then decreases significantly due to the change of the concentration gradients of the reactant which is consumed rapidly at the interface. Figure 1.10 describes the current response in the step potential experiment.

The observed current not only depends on the potential applied and the experimental time, but also relies on the shape and size of the working electrode. At a macroelectrode where linear diffusion dominates, the current-time dependence can be described by Cottrell equation[30]:

$$I = \frac{nFAD^{\frac{1}{2}}c}{\pi^{\frac{1}{2}}t^{\frac{1}{2}}} \qquad \text{(Eqn.1.30)}$$

where n is the number of electrons transferred, F is the Faraday constant, A is the area of the electrode, D is the diffusion coefficient of the species and t is the time.

It is noted that in this expression the decay of current is inversely proportional to the square root of time and it will tend to zero as the time becomes infinite.

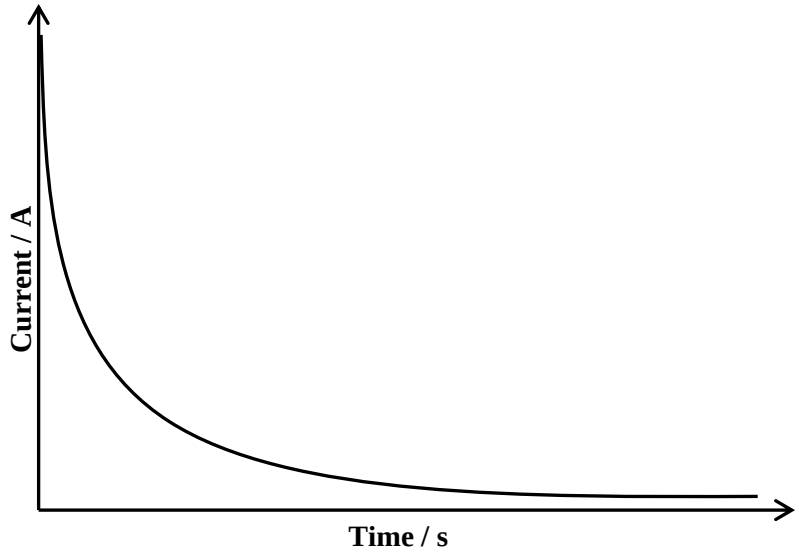


Figure 1.10 The current response against time during a chronoamperometry experiment

When a potential step is applied to a microelectrode, the current response reflects the experimental time scale. In the short-time limit, the thickness of the diffusion layer is smaller than the radius of the electrode, thus the diffusion regime is that of linear diffusion and the current is simply predicted by the Cottrell equation. However, when the time is longer, a convergent diffusion is established and a steady-state current results. The Shoup and Szabo equation[31] is employed to describe the current response over all times with a maximum error of 0.6%:

$$I = 4nFDcr_e f(\tau) \quad \text{(Eqn.1.31)}$$

where

$$f(\tau) = 0.7854 + 0.8863\tau^{-\frac{1}{2}} + 0.2146\exp\left(-0.7823\tau^{-\frac{1}{2}}\right) \quad \text{(Eqn.1.32)}$$

and where the time parameter τ is given by[32]

$$\tau = \frac{4Dt}{{r_e}^2} \qquad \text{(Eqn.1.33)}$$

Thus, potential step chronoamperometry can be used to obtain information from electrochemical data to simulate the value of diffusion coefficients[1, 2, 33-35], numbers of electrons transferred[1, 2, 36, 37], concentrations of analytes[1, 2, 38-40] and surface area of the working electrodes. Another application of chronoamperometry is in so called "nano-impacts" which will be introduced in detail in the next chapter.

References

1. R. G. Compton and C. E. Banks, *Understanding Voltammetry, 2nd Edition*, 2011, 1-429.
2. A. J. Bard and L. R. Faulkner, *Electrochemical Methods : Fundamentals and Applications*, *2nd Edition*., Wiley, New York, 2001.
3. C. M. A. Brett and A. M. O. Brett, *Electrochemistry : Principles, Methods, and Applications*, Oxford University Press, Oxford ; New York, 1993.
4. A. C. Fisher, *Electrode Dynamics*, Oxford University Press, Oxford ; New York, 1996.
5. F. Scholz and A. M. Bond, *Electroanalytical Methods : Guide to Experiments and Applications*, *2nd Revised and Extended Edition*., Springer, Heidelberg ; New York, 2010.
6. P. H. Rieger, *Electrochemistry*, Prentice-Hall, Englewood Cliffs, N.J., 1987.
7. J. Butler, *Transactions of the Faraday Society*, 1924, **19**, 729-733.
8. T. Erdey-Gruz and M. Volmer, *Zeitschrift für Physikalische Chemie*, 1930, **150**, 203-213.
9. A. Fick, *Annalen der Physik*, 1855, **170**, 59-86.
10. A. Einstein, *Annalen der physik*, 1905, **322**, 891-921.
11. R. G. Compton and P. R. Unwin, *Journal of Electroanalytical Chemistry and Interfacial Electrochemistry*, 1986, **205**, 1-20.
12. F. Qiu, R. G. Compton, B. A. Coles and F. Marken, *Journal of Electroanalytical Chemistry*, 2000, **492**, 150-155.
13. R. G. Compton, J. C. Eklund and F. Marken, *Electroanalysis*, 1997, **9**, 509-522.
14. E. Frackowiak and F. Beguin, *Carbon*, 2001, **39**, 937-950.

15. J. Chmiola, G. Yushin, Y. Gogotsi, C. Portet, P. Simon and P.-L. Taberna, *Science*, 2006, **313**, 1760-1763.

16. B. E. Conway, *Electrochemical Supercapacitors: Scientific Fundamentals and Technological Applications*, Springer Science & Business Media, 2013.

17. H. von Helmholtz, *Annual Review of Physical Chemistry*, 1853, **89**, 211-233.

18. G. Gouy, *Journal of Theoretical and Applied Physics*, 1910, **9**, 457-467.

19. D. L. Chapman, *The London, Edinburgh, and Dublin Philosophical Magazine and Journal of Science*, 1913, **25**, 475-481.

20. O. Stern, *Z. Elektrochem*, 1924, **30**, 1014-1020.

21. D. C. Grahame, *Chemical Reviews*, 1947, **41**, 441-501.

22. D. C. Grahame, *Physics Reviews*, 1947, **72**, 522-522.

23. I. U. r. V. Pleskov and V. I. U. l. e. Filinovskiĭ, *The Rotating Disc Electrode*, Consultants Bureau, 1976.

24. D. Gabe and F. Walsh, *Journal of Applied Electrochemistry*, 1983, **13**, 3-21.

25. G. A. Mabbott, *Journal of Chemical Education*, 1983, **60**, 697.

26. J. E. B. Randles, *Transactions of the Faraday Society*, 1948, **44**, 327-338.

27. A. Ševčik, *Collection of Czechoslovak Chemical Communications*, 1948, **13**, 349-377.

28. H. Matsuda and Y. Ayabe, *Zeitschrift für Elektrochemie, Berichte der Bunsengesellschaft für Physikalische Chemie*, 1955, **59**, 494-503.

29. Y. Saito, *Review of Polarography*, 1968, **15**, 177-187.

30. F. Cottrell, *Zeitschrift für Physikalische Chemie*, 1903, **42**, 385-431.

31. D. Shoup and A. Szabo, *Journal of Electroanalytical Chemistry and Interfacial Electrochemistry*, 1982, **140**, 237-245.

32. K. Aoki and J. Osteryoung, *Journal of Electroanalytical Chemistry and Interfacial Electrochemistry*, 1981, **122**, 19-35.

33. G. Denuault, M. V. Mirkin and A. J. Bard, *Journal of Electroanalytical Chemistry and Interfacial Electrochemistry*, 1991, **308**, 27-38.

34. M. C. Buzzeo, O. V. Klymenko, J. D. Wadhawan, C. Hardacre, K. R. Seddon and R. G. Compton, *The Journal of Physical Chemistry A*, 2003, **107**, 8872-8878.

35. Y. Wang, J. G. Limon-Petersen and R. G. Compton, *Journal of Electroanalytical Chemistry*, 2011, **652**, 13-17.

36. C. A. Paddon, D. S. Silvester, F. L. Bhatti, T. J. Donohoe and R. G. Compton, *Electroanalysis*, 2007, **19**, 11-22.

37. D. S. Silvester, A. J. Wain, L. Aldous, C. Hardacre and R. G. Compton, *Journal of Electroanalytical Chemistry*, 2006, **596**, 131-140.

38. Y. Wang, E. Laborda, K. R. Ward, K. Tschulik and R. G. Compton, *Nanoscale*, 2013, **5**, 9699-9708.

39. L. Xiong, E. O. Barnes and R. G. Compton, *Sensors and Actuators B: Chemical*, 2014, **200**, 157-166.

40. L. Xiong, A. M. Fletcher, S. Ernst, S. G. Davies and R. G. Compton, *Analyst*, 2012, **137**, 2567-2573.

Chapter 2

Nanoparticles and Existing Technologies

In the last thirty years, nanoparticles have found an enormous diversity of applications in fundamental research and commercial manufacturing. There is an urgent demand to detect and study their physical properties and some uncertain effects on human health and natural environment[1]. For example, silver nanoparticles have been widely used as antibacterial products in medical instruments and toothpaste[2]. Gold nanoparticles supported on alumina have been used to remove inorganic mercury from drinking water[3]. Iron nanoparticles have been used to remove metals such as Co and Cr[4]. Organic nanoparticles, due to their large range of molecular structures[5] and their capability to tailor binding affinity toward various materials[6] have attracted significant attention recently. Examples of applications include acting as carriers for the controlled release of drugs under specific stimuli and delivering hydrophobic drugs to target cells[7]. It is important to study the physical properties of organic nanoparticles themselves, the mass transport to and from nanoparticle surfaces, chemical reactions and "size-effect" behaviors. Furthermore, it is also significant to understand the fundamental electrochemical reactions at the interface at the nanoscale and so develop applications arising from the associated kinetics and thermodynamics.

This chapter introduces the detection of nanoparticles by using electrochemical methods such as stripping voltammetry, "nano-impacts", nanoparticle measurements at "sticking surfaces" and existing characterizations of nanoparticles including nanoparticles tracking

analysis (NTA), dynamic light scattering (DLS) and scanning electron microscopy (SEM). Other techniques in terms of the synthesis of organic nanoparticles and modification electrode are also summarized.

2.1 Synthesis of Organic Nanoparticles

There are a large number of methods for the fabrication of metal nanoparticles reported and developed[8], however, only a few of these approaches can be used for synthesis of organic nanoparticles due to their poor mechanical properties, lower melting temperatures and thermal instability. The mechanical milling method[9] can only be used to prepare *micro*particles because of particles' aggregating during the long time process. The laser ablation method[10, 11] may cause photochemical damage of the organic nanoparticles and the solvent deposition method[12] has the drawback of generating large size distributions and may also result in nanocrystals being prepared[13, 14]. In this thesis, all organic nanoparticles are synthesized by the reprecipitation method which is a simple and environmental friendly approach with low cost and which can be readily realized in the laboratory.

The reprecipatation method was first proposed by Kasai et al. in 1992 demonstrating that nanoparticles smaller than 100nm dispersed in water could be prepared[15]. Specifically, this method involves two main steps[8]. First, a target compound is dissolved at a concentration of the order of millmolar in a "good solvent" such as tetrahydrofuran (THF), alcohol, acetone (in which the compound is highly soluble). Then, a few microlitres of this solution

is injected rapidly into a much larger volume of a vigorously stirred "poor solvent" such as water (in which the compound is insoluble or much less soluble) at constant temperature (and below the boiling point of the good solvent). After sonication treatment for several minutes small nanoparticles can be produced. The usual procedures of the reprecipitation

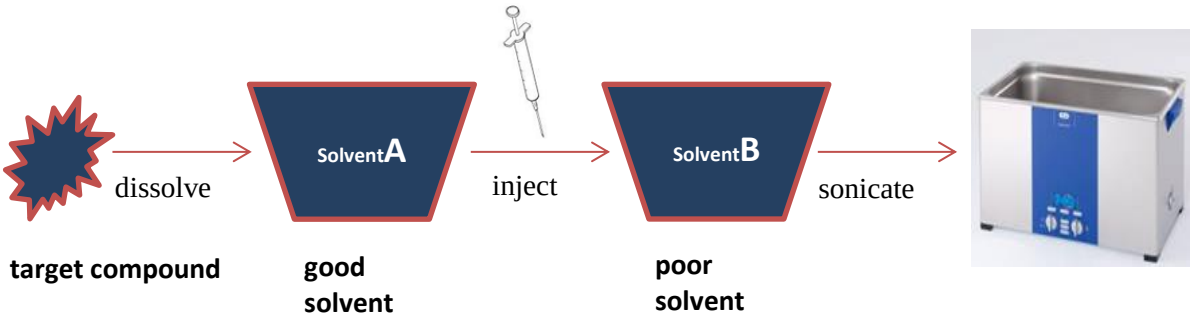


Figure 2.1 Schematic diagram demonstrating the processes of the reprecipitation method

method are shown schematically in figure 2.1. The key to this method is the different solubilities of the target species in the good solvent and the poor solvent and the miscibility between the two solvents. Recently, the reprecipitation method has been widely used to prepare various kinds of organic nanoparticles such as 1-phenyl-3-((dimethylamino)styryl)-5-((dimethylamino)phenyl)-2-pyrazoline (PDDP) nanoparticles[16] and poly(N-vinylcarbazole) (PVK) nanoparticles[17, 18] etc. The size of particles can be controlled by the use of different concentrations of the target in the good solvent and by varying the injecting speed. Alternatively, some organic nanoparticles can be prepared by the reprecipitation method in different solutions. For example nano-C_{60} can be synthesized by injecting C_{60} dissolved in N-Methyl-2-pyrrolidone (NMP) into vigorous stirred acetonitrile at room temperature[19]. The resulting particle size varied between 30-50nm.

2.2 The Modification of Electrodes

In order to achieve a quantifiable signal in electrochemical experiments, the concentration of nanoparticles is required to be calibrated at an appropriate level, which is normally low but much higher than is found naturally. A variety of methods for the modification of electrodes can be used to pre-concentrate nanoparticles before electrochemical experiments conducted such as drop casting[20, 21], spin coating[22, 23], spray coating[24, 25], dip coating[26, 27] and "sticky electrodes"[28]. Generally a thin film (between a sub-monolayer and a multilayer) of selected nanoparticles is bonded or coated on the surface of electrode. The films can be studied using stripping voltammetry to detect the electrochemical properties in terms of numbers of electrons transferred and redox potentials. In this project, drop casting techniques and "sticky electrodes" are used to modify electrodes.

2.2.1 Drop Casting Techniques

Drop casting is a simple modification method which involves the process of casting a drop of a solution or suspension on a normally macroelectrode surface with subsequent evaporation of the solvent to immobilize a species or nanoparticles of interest on a surface[29]. In nano-chemistry, it can be used to determine suitable potentials for the reductive and oxidative electron transfer to nanoparticles. Drop casting is a simple and easy way to modify a working electrode with almost no material waste. However, it has limitations in terms of leading to large area coverage and that the film thickness is hard to control. This method has been used in modification by silver[21, 30], nickel[31], nickel oxide[32],

copper[33] and copper oxide nanoparticles[34] of working electrodes. Figure 2.2 shows the process of drop casting on a glassy carbon working electrode.

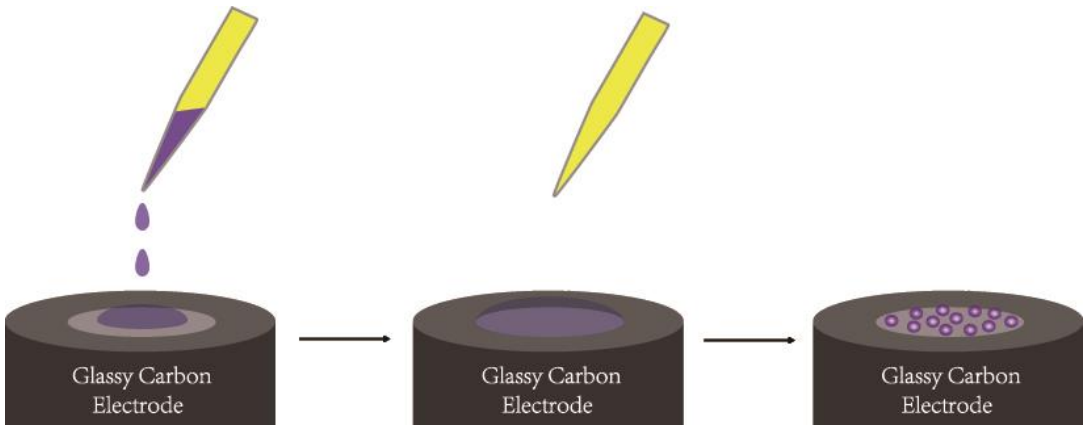


Figure 2.2 Schematic diagram showing drop casting processes of a nanoparticles suspension on a glassy carbon working electrode

2.2.2 "Sticky Electrodes"

The "sticky electrode" modification involves immersing an electrode in a nanoparticle suspension and waiting for a certain amount of time for nanoparticles to collide and adhere to the electrode surface[29]. This approach allows the immobilization to take place at open circuit potential with no potential applied during sticking time and can also be performed with a positive or negative potential applied to the electrode[29, 35]. It is possible to detect the nanoparticles in a very low concentration by using a long sticking duration. The subsequent stripping can either be performed in the field by a portable potentiostat or the modified electrodes can be effectively removed and analyzed in a laboratory later. The

study of the adsorption process in this method is utilized to minimize surface agglomeration of nanoparticles and allows the controlled modification of microelectrodes[36]. The electrode can itself be chemically pre-modified to enhance its "sticking" properties. Apart from this, 'sticky' electrodes have also been found to work effectively in natural seawater samples indicating that this simple technique offers low limits of detection for silver nanoparticles and is very promising for the in-field monitoring of nanoparticles in the environment[37]. Figure 2.3 shows a carbon electrode modified with a "sticky" surface to capture silver nanoparticles which are later stripped off using stripping voltammetry. The experiments with organic nanoparticles building upon the "stick and strip method" will be presented in detail in Chapter 4.

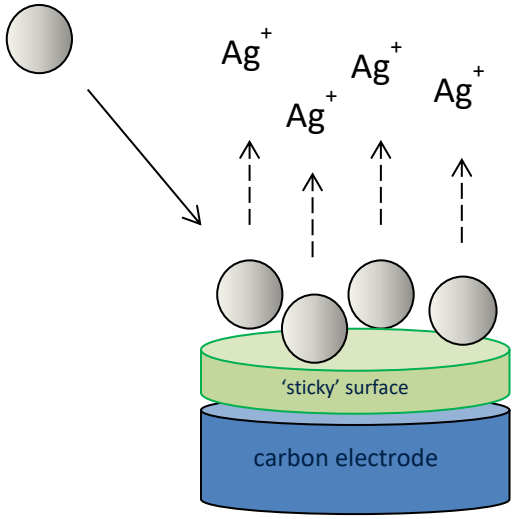
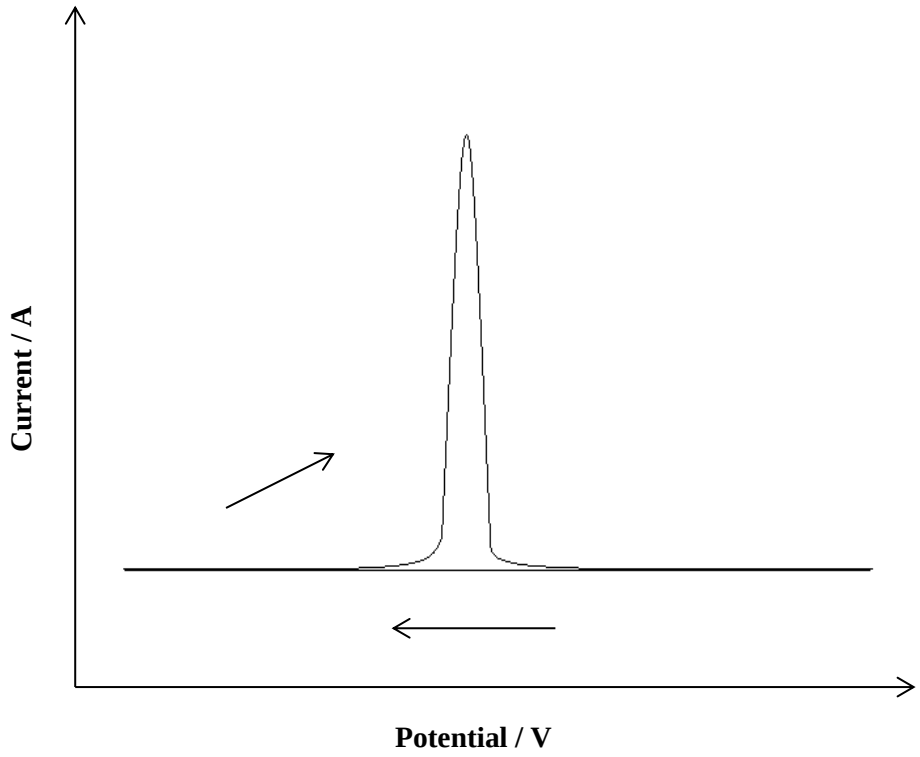


Figure 2.3 Schematic diagram showing silver nanoparticles immobilized on a "sticky" carbon electrode

2.3 Stripping Voltammetry

Stripping voltammetry is an electrochemical technique with the advantage of being simple and quick for the detection and quantitation of nanoparticles. The remarkable sensitivity of stripping voltammetry has been used in trace analysis with ease and success for a wide variety of analytical applications[38-42]. It involves a cathodic or an anodic process in which nanoparticles are immobilized on an electrode surface and then the application of a voltage scan to the electrode which causes an electrolytic dissolution or stripping of the nanoparticles into the solution at a characteristic potential. The specific potentials are chosen so as to remove ("strip") the species from the surface of the electrode.



Figrue 2.4 An ideal stripping voltammogram of an oxidation reaction

Figure 2.4 shows the ideal voltammetry of a chemically irreversible oxidative stripping. It can quantify the amount of the materials which react on the surface of the electrode by integration of the oxidative peak area and the use of by equation 2.1:

$$M_{surface} = \frac{Q}{nF} \qquad \text{(Eqn.2.1)}$$

where the number of moles of formed product or consumed reactant is given by $M_{surface}$, n is the number of electrons transferred per reactant , Q is the charge passed under the voltammetric signal and F is the Faraday constant.

Stripping voltammetry has usefully detected numerous nanoparticles. A general theory for the stripping voltammetry of silver nanoparticles modified by using drop casting on the glassy carbon electrode was presented recently by Toh *et al* [43]. It is found that the oxidative peak potential for silver nanoparticles is expected to be below the formal potential for the oxidation and that the size effect upon the measured voltammetry is related to the change of the surface coverage of the silver nanoparticles. For high surface coverage, a linear diffusion regime to the electrode surface is formed due to the diffusion layers of individual nanoparticles strongly overlapping. In contrast, for a low nanoparticle surface coverage, the diffusion layers of the nanoparticles do not overlap and radial diffusion dominates the mass transport to each of the nanoparticles, which depends on the size of the silver nanoparticles but not the surface coverage. Another basic work demonstrating stripping voltammetry on a microelectrode was reported by Neumann *et al*[36]. In this work, a carbon fiber microelectrode was pre-concentrated with two different

sizes of silver nanoparticles at a potential of -0.250 V vs SCE as a function of time. The stripping voltammetry signal became larger as the adsorption duration increased. The oxidative peak was found to be +0.2-0.35 V vs SCE which was significantly below the formal potential +0.555 V.

Most of the electrochemical studies for the detection and characterization of nanoparticles are at the fundamental level and carried out in laboratory settings. Additional applications of stripping voltammetry are introduced in detail in Chapter 4-9. A novel electrochemical technique for detection and analysis of *individual* nanoparticles through impacts on the working electrode is introduced in the next section.

2.4 Nano-impacts

"Nano-impacts" is an electrochemical method to detect a small quantity of nanoparticles suspended in solution[44]. In this approach, nanoparticles move to the electrode surface by random motion ("Brownian motion" observed by Robert Brown for large pollen grains in the 18th century). Electrochemical monitoring is performed at a suitable potential with a short burst of current observed during the random collision between the nanoparticles and electrode of the particles are oxidized or reduced. The results can not only be used to determine the size[44, 45] and concentration[31] of the nanoparticles, but also to identify the nature of the nanoparticles and to infer if they aggregate or agglomerate[46] or not. Such electrochemical data is difficult and often impossible to obtain from previous existing techniques.

The first electrochemical signatures of impacts between particles and electrode surfaces were reported by Heyrovsky et al. in 1995[47-50]. They studied the voltammetry of polydisperse colloidal solutions of SnO_2, TiO_2 and Fe_2O_3 in aqueous solution by using mercury electrodes. Then this principle was developed by Scholz *et al*[51, 52] in the early 2000s with experiments using micron size single montmorillonite particles contacting a mercury drop electrode. Non-Faradaic spikes were investigated during the collision which disturbed the double layer around the electrode. Further observations by Bard et al[53-55] identified electrocatalytic processes occurring on the surface of nanoparticles during collisions. Meanwhile, the Compton group showed that Faradaic charge transfer transients can arise during such impacts from oxidation or reduction of nanoparticles. The method allows the Faradaic charges resulting from the impacts of nanoparticles be measured and analyzed[31, 44, 56]. Specifically, the instantaneous change of current is detected as a "spike" or a "blip" when a nanoparticle impacts the electrode. This process involves a suitable potential to be applied to a micro working electrode which can cause electro-oxidation or -reduction of the nanoparticles during a current-time transient.

Direct oxidation and reduction of individual nanoparticles impacting at a solid ultramicroelectrode electrode can provide a variety of physical and chemical information about the nanoparticles. Specifically, nanoparticle "coulometry" can be used to measure the size of individual metal nanoparticles such as nickel, silver and gold nanoparticles[21, 44, 45]. In a typical experiment, for example, sizing Ni nanoparticles[31], a known concentration of pre-dispersed Ni nanoparticles was added into degassed $HClO_4$ and $NaClO_4$ solution and a carbon fiber electrode immersed. Typical oxidative spikes were observed when the electrode potential was held at +1.7 V vs. Ag/AgCl but no oxidative spikes were observed at +1.0 V, confirming that the current spikes corresponded to Faradaic oxidation of Ni

nanoparticles. The resulting data were used to establish a relationship between the diameter and charge of the single Ni nanoparticles with the shape of the nanoparticles assumed to be spherical:

$$D_{np} = 2 \times \sqrt[3]{\frac{3A_r Q}{4nF\pi\rho}} \qquad \text{(Eqn.2.2)}$$

where D_{np} is the diameter of the Ni nanoparticles, A_r is the relative atomic mass of Ni, Q is the charge (coulombs) passed by the individual Ni nanoparticles by integrating the area of each spike, n is the number of electrons transferred and ρ is the density of the Ni nanoparticles.

Another application of the direct electrochemistry of nanoparticles via the nano-impacts method is to determine the concentration of nanoparticles in solution. Again using Ni nanoparticles as an example, Stuart et al[31] measured the number of impacts as a function of time and fitted the data to the Shoup-Szabo equation[57] (Eqn.1.31), showing that the concentration of the Ni nanoparticles solution can be determined from the frequency of the impacts and that the latter is diffusion controlled.

Apart from this, nano-impacts methodology is also beneficial in understanding the sensitivity of nanoparticles to their environment. The aggregation kinetics of silver nanoparticles was found to depend on not only the electrolytes in which the nanoparticles were dispersed, but also the size and capping agents of the nanoparticles[58]. For instance, in the work of Ellison *et al*[46], the agglomeration of Ag nanoparticles in a solution containing

90 mM Potassium chloride and 10m M mono-sodium citrate has been studied via impact-based anodic particle coulometry (APC). The proportion of monomers, dimers, trimers, tetramers, pentamers and hexamers of silver nanoparticles was analyzed by recording size of each impact. In another study by Lee *et al*[59] on the effect of electrolyte on nanoparticle aggregation, four different samples of Ag nanoparticles with different size distributions were analyzed by anodic particle coulometry with nano-impact experiments in the 0.1 M citrate solution. The size of the various batches of Ag nanoparticles was also characterized by SEM and showed excellent agreement with the impact data. The result indicated that aggregation of silver nanoparticles is minimized in the presence of such electrolyte. Recently, Stuart *et al*[60] demonstrated that impact experiments can be used to identify and characterize Ag nanoparticles in natural aquatic systems. The experiments found that the Ag nanoparticles form aggregates of 2, 3, 4, and 5 monomers over a timescale of 42 min. This study allows laboratory synthesized Ag nanoparticles to be detected in environmental media. Their further research found that Ag nanoparticles can be characterized from a commercial product, a colloidal silver disinfectant spray, and in seawater. This technique thus shows a great promise for the applications of nano-impacts methodology[61].

Metal oxides, such as Fe_3O_4 nanoparticles, have also been studied by this electrochemical method with SEM employed to confirm the accuracy of the sizing[62]. The charges passed from both oxidation and reduction of individual Fe_3O_4 nanoparticles show a ratio of 1:2, which indicates that both anodic and cathodic particle coulometry can provide quantitative information on the electroanalysis of the nanoparticles. In addition, the direct nano-impacts method has also been shown to be effective for the characterization of other types of nanoparticles including copper nanoparticles[33], fullerenes[19] and liposomes containing

vitamin C[63] etc. Figure 2.5 (1) and (3) shows the typical spikes seen from different types of "direct" and "indirect" nano-impact experiments.

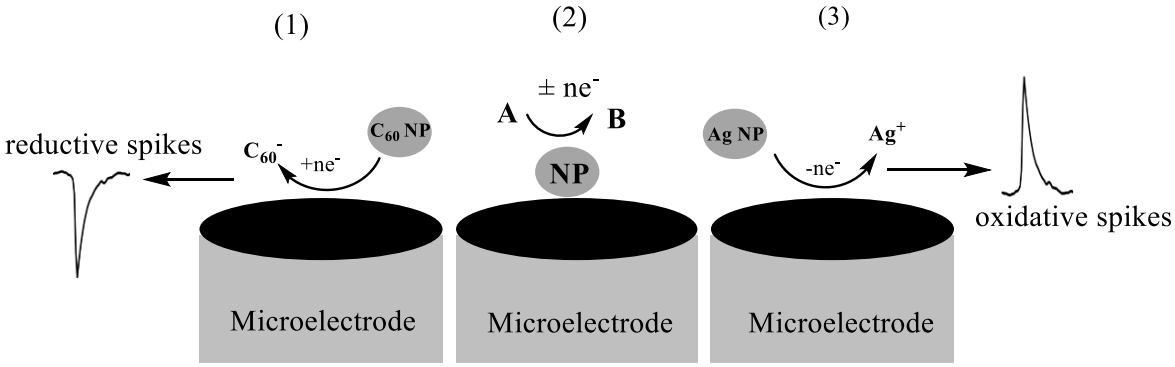


Figure 2.5 Schematic diagrams illustrating the "nano-impact" method: (1) the direct reduction of a fullerene nanoparticle (2) the indirect nanoparticle mediated electron-transfer turning A to B and (3) the direct oxidation of silver nanoparticles

Further, another type of nanoparticles, so called "tagged nanoparticles", has found increasing use analytically and have been investigated by anodic particle coulometry recently[64]. Here, the nanoparticles themselves are not oxidized or reduced. Instead molecules which are tagged on the nanoparticle surface undergo the electrochemical reaction during the measurements. In one study 1,4-nitrothiophenol (NTP)[21] was pre-absorbed onto the silver nanoparticles. When the nanoparticles hit the electrode surface, sharp reductive current transients were seen corresponding the 4 electron reduction of the attached NTP molecules. The tag-redox coulometry provides a non-destructive strategy[65] to the characterization of the nanoparticles and achieves the sizing of nanoparticles.

The electron transferred from or to nanoparticles by nano-impacts experiments is referred to as a "direct" process (as above). Based on the early work by Heyrovsky and further work by Bard's group, another type of impact experiment involves "indirect" electron transfer and relates to electrocatalytic processes as shown in Figure 2.5(2), such as the proton reduction at the surface of Pt nanoparticles[66], the oxidation of hydrazine at Au nanoparticles[54] and Pt nanoparticles[67] and the oxidation of water at IrO_x nanoparticles[55]. In these experiments, the nanoparticles mediate the electrocatalysis only when they are in contact with the electrode. Two different transients shapes observed for the electrocatalytic amplification[68]; "spike" responses appear when the impact time is short but "staircase" responses (as shown in Figure 2.6) when the nanoparticles adsorb at the electrode surface. One good example of a "staircase" response is in the work on proton reduction[66] which is catalyzed on Pt nanoparticles on a micro carbon electrode. Pt nanoparticles reside on the surface of the micro carbon electrode after impacting. It is found that before injection of the particle solution, the current transient was a smooth curve with a small constant noise level, while after injection, peaked current transients appeared. Moreover, the potential of proton reduction on the Pt nanoparticles is lower than that appears on naked carbon electrode. As the number of Pt nanoparticles stick on the surface of the electrode increases, a staircase voltammogram was obtained. It was found that the characteristics of an individual current time profile are determined by many factors. If the nanoparticles stick to the electrode surface, the steady state diffusion controlled current at a nanoparticle is (assuming the shape of the nanoparticle is spherical):

$$I_{ss} = 4\pi(ln2)nFDCr_{np} \qquad \text{(Eqn.2.3)}$$

where n is the number of electrons transferred, F is the Faraday constant, D is diffusion coefficient, C is the concentration, and r_{np} is the radius of the nanoparticle. In this situation, the step current is formed by adding the new nanoparticles to the previous current and a "staircase" is observed. Both the impact and adsorption of nanoparticles have been studied theoretically by Barnes et al[69, 70].

Even though the use of nano-impacts method including direct oxidation or reduction, tagged nanoparticles and indirect electrocatalysis has been developed for various types of nanoparticles, the work is still at a very early stage. In this thesis, for the first time we use this novel approach to detect the physical and chemical properties of single *organic* nanoparticles. The experimental details and results are presented in next chapters.

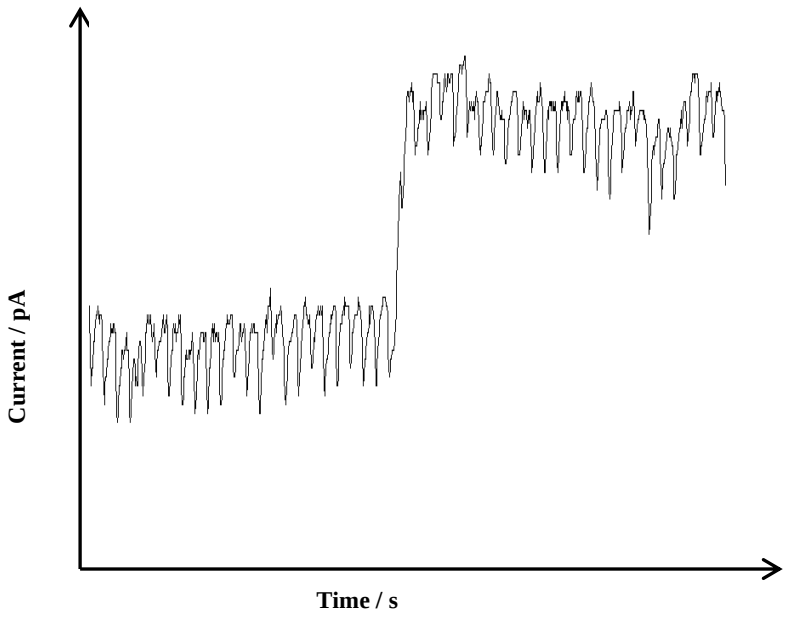


Figure 2.6 Schematic diagram showing a typical "staircase" signal obtained from a chronoamperogram for an indirect redox process mediated via adsorbed nanoparticles

2.5 Characterization of Nanoparticles

There are various existing advanced techniques for detecting, measuring and characterizing nanoparticles. However, there is no one that can be selected a “best” method due to the restriction of the types of sample, the information required and the cost of analysis. A straightforward technique may simply detect the presence of nanoparticles, and give the size distribution or shape and surface area of the nanoparticles. The approaches also differ in respect of information on the amount of nanoparticles present and whether they look at individual nanoparticles or not. In normal experiments, measurement techniques are combined to provide more information on a specific nanoparticles sample.

In this section, the principles of the following techniques, Scanning Electron Microscopy, Dynamic Light Scattering, Nanoparticle Tracking Analysis and Ultraviolet-visible spectroscopy are discussed with their advantages and limitations. These methods are used to detect and characterize the organic nanoparticles studied in this thesis.

2.5.1 Scanning Electron Microscopy

A scanning electron microscopy uses a focus of beam electrons to scan a sample producing a direct image of the latter. The principle of this technique is given in the schematic diagram in Figure 2.7. An electron gun is located at the top of a column where free electrons are generated by a thermionic emission filament. The electron beam is focused on the sample of interest passing the condenser and objective lenses. The

condenser lens is responsible for determining the intensity of the electron beam and objective lens is used to focus and determine the final diameter of the electron probe. Scanning coils between the two lenses control the magnification by means of a current supply. When the secondary electrons detected by the detector, an image displaying the pattern of the sample is created.

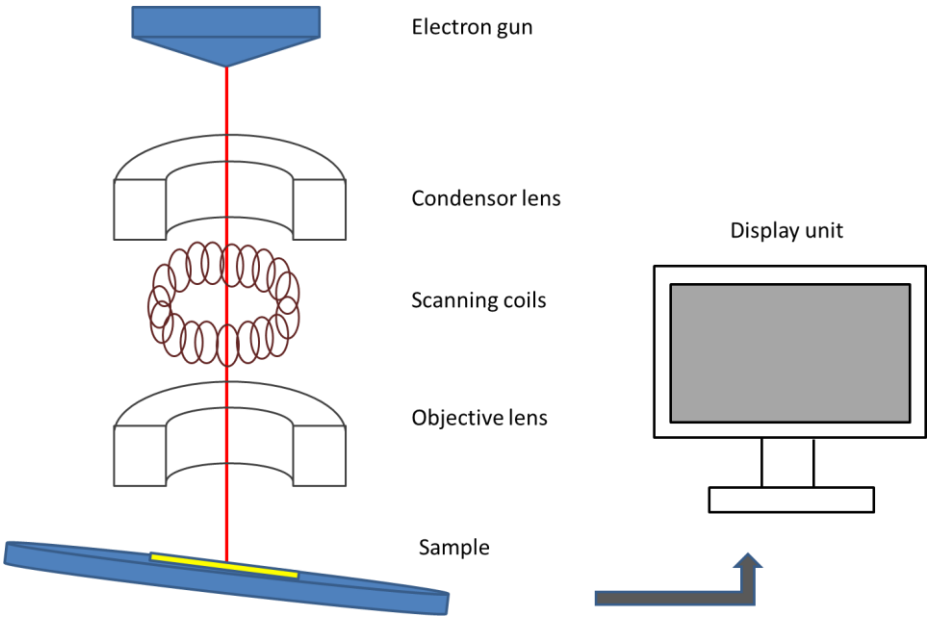


Figure 2.7 Schematic diagram showing the basic construction of a SEM

SEM is a very popular characterization method that allows the user to not only detect the size of nanoparticles, but also to characterize the real shape of the nanoparticles directly. In electrochemistry, it can also provide information about nanoparticle modified electrodes. However, the SEM technique needs the prepared nanoparticle sample to be dry which

means that the nanoparticles cannot be measured in solution. This may influence the accuracy of sizing for some of the nanoparticles which tend to aggregate or agglomerate during preparation on the holder. Another issue is that SEM sometimes can result in uncertainty about a whole nanoparticles population because the detecting and counting are manual processes subject to human error.

2.5.2 Dynamic Light Scattering

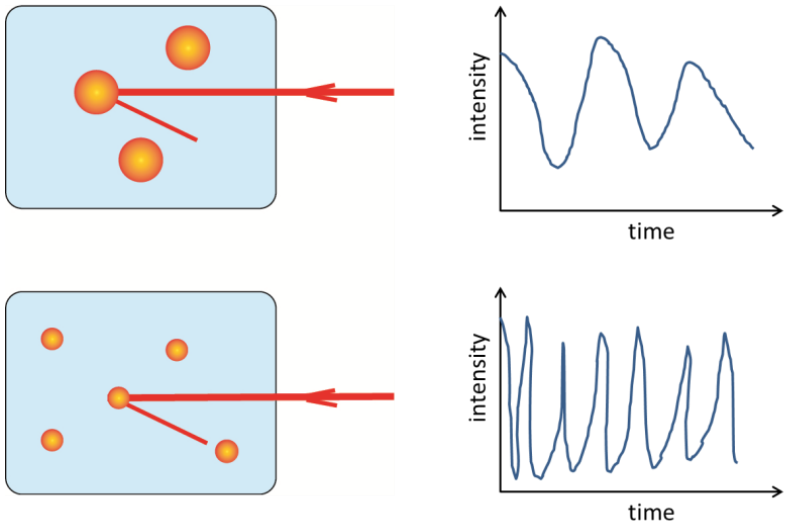


Figure 2.8 Schematic diagram of DLS used to measure big or small nanoparticles in solution

The Dynamic light scattering (DLS) technique is one of the most popular methods used to determine the size distribution of nanoparticles dispersed in liquid solution. A light beam, such as a laser, is used to irradiate the nanoparticles which are subject to Brownian motion.

When the light hits the moving nanoparticles, the wavelength of the incoming light changed in a way which is related to the size of the nanoparticles. It is possible to see that larger nanoparticles with a slower velocity results in a lower frequency of light intensity than that measured for smaller nanoparticles (as shown in Figure 2.8). The size distribution of the nanoparticles can be estimated via the Stoke-Einstein equation by measuring the diffusion coefficient (D) of the nanoparticles:

$$D = \frac{k_B T}{6\pi\eta r_{NP}} \qquad \text{(Eqn.2.4)}$$

where r_{NP} is the radius of the nanoparticles, k_B is the Boltzmann constant, T is the temperature and η is the viscosity of the solution.

DLS has several advantages: first of all the measurement is very quick and it is almost fully automatic and easy to carry out. Furthermore, the cost of DLS measurement is modest and the sample is measured as a whole. It can also detect the real size of nanoparticles in solution avoiding nanoparticles aggregating as in SEM measurements. This method is powerful to characterize nanoparticles which are prepared in solution. However, there are also some limitations of DLS. For instance, DLS measures the overall signal from the nanoparticles solution which is very sensitive to the presence of large nanoparticles. This can be compromising when monitoring the nanoparticles with high aggregation and agglomeration states or highly polydispersed nanoparticles. The presence of possible dust particles can also influence the accuracy of the measurements.

2.5.3 Nanoparticle Tracking Analysis

Nanoparticle tracking analysis (NTA) is a relatively newly developed method for the direct and real-time visualization and analysis of nanoparticles in liquid solution[71]. Based on a laser illuminating the sample, the Brownian motion of nanoparticles is analyzed in real-time while single particles are tracked by a microscope with an incorporated digital video recorder. As the average distance each nanoparticle moves in a 2D plane in an image is automatically calculated, the diffusion coefficient of the particle can be obtained from this value:

$$D = \frac{\overline{(x,y)^2}}{4} \qquad \text{(Eqn.2.5)}$$

where $\overline{(x,y)^2}$ is the mean square distance diffused.

Then the range of particle sizes can be analyzed knowing the sample temperature and the solution viscosity using Eqn.2.4. NTA can measure the nanoparticle size straightforwardly and the particle scattering intensity allows heterogeneous particle mixtures to be resolved. Moreover, the concentration of the nanoparticle solution can also be estimated directly according to the number of nanoparticles in an image. Nevertheless, it has fundamental limitations on the minimum particle size that can be detected due to the scattering from small particles and image analysis requires a significant input from the operator, which may cause bias.

2.5.4 Ultraviolet-visible Spectroscopy

Ultraviolet-visible spectroscopy (UV-Vis) technique is based on the electrons in a molecule being excited by absorption of ultraviolet or visible light. Molecules undergo electronic transitions in this region of the electromagnetic spectrum which affects the visible perceived color of chemicals.

UV-Vis can be employed to determine the size of gold nanoparticle[72] and it also can be used to analyze the composition and structure in organic detection. In this thesis, UV-Vis is performed to infer the composition and stability of organic nanoparticles after synthesis.

Chapter 1 and Chapter 2 give the introduction to the fundamentals of electrochemistry, nanoparticles and existing techniques to detect nanoparticles. It is relevant for the investigation of many fundamental issues in nanochemistry along with concomitant revolutionary change in analytical science and its applications from the program of work exploits the electrochemistry of *single* nanoparticles in solution.

In the next chapters, we focus on the study and characterisation of organic nanoparticle samples by using both electrochemical methods and existing techniques, providing information such as electrochemical sizing and electron transfer kinetics of organic nanoparticles during their oxidation or/and reduction.

References

1. W. Cheng and R. G. Compton, *Trends in Analytical Chemistry*, 2014, **58**, 79-89.
2. M. Ahamed, M. S. AlSalhi and M. K. J. Siddiqui, *Clinica Chimica Acta*, 2010, **411**, 1841-1848.
3. K. Lisha and T. Pradeep, *Gold Bulletin*, 2009, **42**, 144-152.
4. D. Zhang, S. Wei, C. Kaila, X. Su, J. Wu, A. B. Karki, D. P. Young and Z. Guo, *Nanoscale*, 2010, **2**, 917-919.
5. H. Kasai, T. Murakami, Y. Ikuta, Y. Koseki, K. Baba, H. Oikawa, H. Nakanishi, M. Okada, M. Shoji and M. Ueda, *Angewandte Chemie*, 2012, **124**, 10461-10464.
6. M. Oh and C. A. Mirkin, *Nature*, 2005, **438**, 651-654.
7. Y. Namiki, T. Namiki, H. Yoshida, Y. Ishii, A. Tsubota, S. Koido, K. Nariai, M. Mitsunaga, S. Yanagisawa and H. Kashiwagi, *Nature Nanotechnology*, 2009, **4**, 598-606.
8. J. Suk and A. J. Bard, *Journal of Solid State Electrochemistry*, 2011, **15**, 2279-2291.
9. J. Texter, *Journal of Dispersion Science and Technology*, 2001, **22**, 499-527.
10. Y. Tamaki, T. Asahi and H. Masuhara, *The Journal of Physical Chemistry A*, 2002, **106**, 2135-2139.
11. Y. Tamaki, T. Asahi and H. Masuhara, *Japanese Journal of Applied Physics*, 2003, **42**, 2725-2729.
12. T. Seko, K. Ogura, Y. Kawakami, H. Sugino, H. Toyotama and J. Tanaka, *Chemical Physics Letters*, 1998, **291**, 438-444.
13. F. Balzer, V. Bordo, A. C. Simonsen and H. G. Rubahn, *Applied Physics Letters*, 2003, **82**, 10-12.

14. H. Liu, Y. Li, S. Xiao, H. Gan, T. Jiu, H. Li, L. Jiang, D. Zhu, D. Yu, B. Xiang and Y. Chen, *Journal of the American Chemical Society*, 2003, **125**, 10794-10795.

15. H. Kasai, H. Oikawa, S. Okada and H. Nakanishi, *Bulletin of the Chemical Society of Japan*, 1998, **71**, 2597-2601.

16. H. B. Fu and J. N. Yao, *Journal of the American Chemical Society*, 2001, **123**, 1434-1439.

17. F. Kong, Y. Sun and R. Yuan, *Nanotechnology*, 2007, **18**, 265707-265712.

18. F. Kong, X. Wu, G. Huang, R. Yuan and P. K. Chu, *Thin Solid Films*, 2008, **516**, 6287-6292.

19. E. J. Stuart, K. Tschulik, C. Batchelor-McAuley and R. G. Compton, *ACS Nano*, 2014, **8**, 7648-7654.

20. Y. R. Kim, S. Bong, Y. J. Kang, Y. Yang, R. K. Mahajan, J. S. Kim and H. Kim, *Biosensors and Bioelectronics*, 2010, **25**, 2366-2369.

21. Y. G. Zhou, N. V. Rees and R. G. Compton, *Chemical Communications*, 2012, **48**, 2510-2512.

22. H. Akahoshi, S. Toshima and K. Itaya, *The Journal of Physical Chemistry*, 1981, **85**, 818-822.

23. F. Kaufman, A. Schroeder, E. Engler, S. Kramer and J. Chambers, *Journal of the American Chemical Society*, 1980, **102**, 483-488.

24. B. Hoyer, G. Sørensen, N. Jensen, D. B. Nielsen and B. Larsen, *Analytical Chemistry*, 1996, **68**, 3840-3844.

25. B. Hoyer, T. M. Florence and G. E. Batley, *Analytical Chemistry*, 1987, **59**, 1608-1614.

26. D. J. Harrison, R. F. B. Turner and H. P. Baltes, *Analytical Chemistry*, 1988, **60**, 2002-2007.

27. W. J. Albery, R. G. Compton and C. C. Jones, *Journal of the American Chemical Society*, 1984, **106**, 469-473.

28. Y. G. Zhou, E. J. Stuart, J. Pillay, S. Vilakazi, R. Tshikhudo, N. V. Rees and R. G. Compton, *Chemical Physics Letters*, 2012, **551**, 68-71.

29. K. Tschulik, C. Batchelor-McAuley, H.-S. Toh, E. J. Stuart and R. G. Compton, *Physical Chemistry Chemical Physics*, 2014, **16**, 616-623.

30. Y. G. Zhou, B. Haddou, N. V. Rees and R. G. Compton, *Physical Chemistry Chemical Physics*, 2012, **14**, 14354-14357.

31. E. J. Stuart, Y. G. Zhou, N. V. Rees and R. G. Compton, *RSC Advances*, 2012, **2**, 6879-6884.

32. K. Fominykh, J. M. Feckl, J. Sicklinger, M. Döblinger, S. Böcklein, J. Ziegler, L. Peter, J. Rathousky, E. W. Scheidt and T. Bein, *Advanced Functional Materials*, 2014, **24**, 3123-3129.

33. B. Haddou, N. V. Rees and R. G. Compton, *Physical Chemistry Chemical Physics*, 2012, **14**, 13612-13617.

34. W. Z. Teo, A. Ambrosi and M. Pumera, *Electrochemistry Communications*, 2013, **28**, 51-53.

35. M. Pumera, M. Aldavert, C. Mills, A. Merkoçi and S. Alegret, *Electrochimica Acta*, 2005, **50**, 3702-3707.

36. C. Neumann, C. Batchelor-McAuley, K. Tschulik, H. S. Toh, P. Shumbula, J. Pillay, R. Tshikhudo and R. G. Compton, *ChemElectroChem*, 2014, **1**, 87-89.

37. K. Tschulik, R. G. Palgrave, C. Batchelor-McAuley and R. G. Compton, *Nanotechnology*, 2013, **24**, 295502-295508.

38. R. T. Kachoosangi, G. G. Wildgoose and R. G. Compton, *Analyst*, 2008, **133**, 888-895.

39. K. E. Toghill and R. G. Compton, *International Journal of Electrochemical Science*, 2010, **5**, 1246-1301.

40. X. J. Huang, L. Aldous, A. M. O'Mahony, F. J. del Campo and R. G. Compton, *Analytical Chemistry*, 2010, **82**, 5238-5245.

41. M. C. Buzzeo, C. Hardacre and R. G. Compton, *Analytical Chemistry*, 2004, **76**, 4583-4588.

42. D. Q. Hung, O. Nekrassova and R. G. Compton, *Talanta*, 2004, **64**, 269-277.

43. H. S. Toh, C. Batchelor-McAuley, K. Tschulik, M. Uhlemann, A. Crossley and R. G. Compton, *Nanoscale*, 2013, **5**, 4884-4893.

44. Y. G. Zhou, N. V. Rees and R. G. Compton, *Angewandte Chemie International Edition*, 2011, **50**, 4219-4221.

45. Y. G. Zhou, N. V. Rees, J. Pillay, R. Tshikhudo, S. Vilakazi and R. G. Compton, *Chemical Communications*, 2011, **48**, 224-226.

46. J. Ellison, K. Tschulik, E. J. Stuart, K. Jurkschat, D. Omanović, M. Uhlemann, A. Crossley and R. G. Compton, *ChemistryOpen*, 2013, **2**, 69-75.

47. M. Heyrovsky and J. Jirkovsky, *Langmuir*, 1995, **11**, 4288-4292.

48. M. Heyrovsky, J. Jirkovsky and B. R. Muller, *Langmuir*, 1995, **11**, 4293-4299.

49. M. Heyrovsky, J. Jirkovsky and M. Struplovabartackova, *Langmuir*, 1995, **11**, 4309-4312.

50. M. Heyrovsky, J. Jirkovsky and M. Struplovabartackova, *Langmuir*, 1995, **11**, 4300-4308.

51. F. Scholz, D. Hellberg, F. Harnisch, A. Hummel and U. Hasse, *Electrochemistry Communications*, 2004, **6**, 929-933.

52. D. Hellberg, F. Scholz, F. Schauer and W. Weitschies, *Electrochemistry Communications*, 2002, **4**, 305-309.

53. X. Xiao and A. J. Bard, *Journal of the American Chemical Society*, 2007, **129**, 9610-9612.

54. X. Xiao, F. R. F. Fan, J. Zhou and A. J. Bard, *Journal of the American Chemical Society*, 2008, **130**, 16669-16677.

55. S. J. Kwon, F. R. F. Fan and A. J. Bard, *Journal of the American Chemical Society*, 2010, **132**, 13165-13167.

56. N. V. Rees, Y. G. Zhou and R. G. Compton, *RSC Advances*, 2012, **2**, 379-384.

57. D. Shoup and A. Szabo, *Journal of Electroanalytical Chemistry and Interfacial Electrochemistry*, 1982, **140**, 237-245.

58. N. V. Rees, Y. G. Zhou and R. G. Compton, *ChemPhysChem*, 2011, **12**, 1645-1647.

59. J. C. Lees, J. Ellison, C. Batchelor-McAuley, K. Tschulik, C. Damm, D. Omanović and R. G. Compton, *ChemPhysChem*, 2013, **14**, 3895-3897.

60. E. Stuart, N. Rees, J. Cullen and R. Compton, *Nanoscale*, 2013, **5**, 174-177.

61. E. Stuart, K. Tschulik, D. Omanović, J. Cullen, K. Jurkschat, A. Crossley and R. Compton, *Nanotechnology*, 2013, **24**, 444002-444007.

62. K. Tschulik, B. Haddou, D. Omanović, N. V. Rees and R. G. Compton, *Nano Research*, 2013, **6**, 836-841.

63. W. Cheng and R. G. Compton, *Angewandte Chemie*, 2014, **126**, 14148-14150.

64. Z. Dai, A. N. Kawde, Y. Xiang, J. T. La Belle, J. Gerlach, V. P. Bhavanandan, L. Joshi and J. Wang, *Journal of the American Chemical Society*, 2006, **128**, 10018-10019.

65. N. V. Rees, Y. G. Zhou and R. G. Compton, *Chemical Physics Letters*, 2012, **525**, 69-71.

66. H. Zhou, F.-R. F. Fan and A. J. Bard, *The Journal of Physical Chemistry Letters*, 2010, **1**, 2671-2674.

67. X. Xiao, S. Pan, J. S. Jang, F.-R. F. Fan and A. J. Bard, *The Journal of Physical Chemistry C*, 2009, **113**, 14978-14982.

68. A. J. Bard, H. Zhou and S. J. Kwon, *Israel Journal of Chemistry*, 2010, **50**, 267-276.

69. E. O. Barnes and R. G. Compton, *Journal of Electroanalytical Chemistry*, 2013, **693**, 73-78.

70. E. O. Barnes, Y. G. Zhou, N. V. Rees and R. G. Compton, *Journal of Electroanalytical Chemistry*, 2013, **691**, 28-34.

71. B. Carr, A. Malloy and P. Hole, *EuroNanoForum 2007*, 2007, 70.

72. W. Haiss, N. T. Thanh, J. Aveyard and D. G. Fernig, *Analytical Chemistry*, 2007, **79**, 4215-4221.

Chapter 3

Electrochemical Sizing of Monomeric Organic Nanoparticles

The work in this thesis is aimed at developing our ability to control and manipulate nanoparticles using electrochemistry, exploring oxidation and reduction processes. In particular we report entirely novel investigations into organic nanoparticles and use nano-impacts (as discussed in Chapter 2) to study their physical and chemical properties. In this chapter, we study for the first time the direct electrochemical sizing of monomeric organic nanoparticles using indigo as a model system, via analysis of the charge transferred in the reduction of individual organic nanoparticles. The electrochemical sizing demonstrates an excellent agreement with characterization using dynamic light scattering (DLS) data showing that the direct electrochemical sizing of organic nanoparticles is feasible and quantitative. It may open a new strategy for characterizing organic nanoparticles in solution and have significance for the future research of organic nanomaterials in diverse applications. This work presented here was carried out in cooperation with Dr. Wei Cheng and published in *Angewandte Chemie International Edition*, 52, (2013), 12980-12982.

3.1 Introduction

Size plays a crucial role in the applications of organic nanoparticles across many fields such as biomedicine, optoelectronics, and environmental science[1-4]. So far, microscopy and spectroscopy techniques have played central roles in organic nanoparticle detection; however, unlike metal nanoparticles, the widespread use of microscopy such as TEM or SEM is limited as the organic particle size may be compromised after drying when imaging is conducted. In comparison to metal and inorganic nanoparticles, the real-time in situ sizing of organic nanoparticle challenges existing techniques because of their presence in complex aqueous media which may affect their aggregation/agglomeration state and stability over time[5]. Light-scattering techniques such as DLS provide a powerful sizing technique for organic nanoparticles in complex solution; however, they measure the overall signal from the whole bulk of nanoparticles which makes DLS in particular very sensitive to the presence of large particles. DLS can thus be influenced by the presence of possible dust particles or small amounts of large aggregates which will influence the size determination. More recently, alternative advanced optical[6, 7] and ultracentrifugation methods[8] have been developed for sizing of nanoparticles, but they generally require expensive instrumentation and long processing times.

Electrochemistry as an alternative method to optical methods provides a more efficient and cost-effective approach for characterization of nanoparticles (NPs)[9-16]. As introduced in Section 2.4, the Compton group has developed the nano-impacts method based on the detection of solution-phase NPs upon their random collision by virtue to their Brownian motion with the imposed electrode. This method has been successfully applied for determining the size[9], concentration[10], the presence of molecular tags[11], and aggregation[12]

of silver and other metal nanoparticles[13, 14]. However, no studies have reported the electrochemical characterization, sizing and detection of organic NPs, although Bard and co-workers have investigated luminescent organic nanoparticles[17-19]. Here, we demonstrate for the first time the direct electrochemical sizing of organic nanoparticles using indigo nanoparticles as a model (The structure of indigo is shown in Figure 3.1), based on Faradaic charge transfer when nanoparticles strike an electrode. This strategy is shown to be both feasible and quantitative, and could be used for size monitoring of a wide range of organic nanoparticles in real environments.

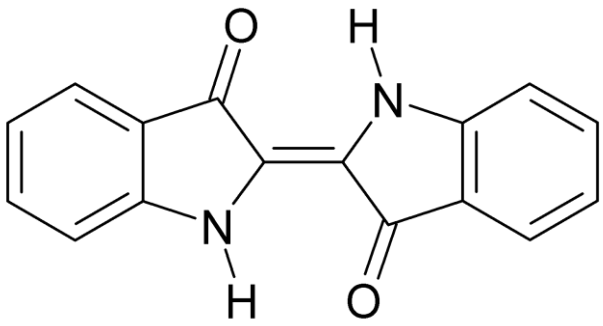


Figure 3.1 Structure of an indigo molecule

3.2 Experimental Section

3.2.1 Chemicals and Materials

Indigo (synthetic, 95%), dimethyl sulfoxide (DMSO, 99.9%, anhydrous) were purchased from Aldrich and used as received. The phosphate buffer solution (pH = 6.8) was composed of 50mM monobasic and dibasic potassium phosphates, 0.1 M KCl used as further supporting electrolyte. Unless stated otherwise, all chemicals in this work were

acquired from Sigma–Aldrich. All solutions were made up using ultrapure water of resistivity 18.2 MΩ cm (Millipore) at 25℃ and degassed thoroughly with N_2 (oxygen-free, BOC Gases plc) before use.

3.2.2 Synthesis of Indigo Nanoparticles

Indigo nanoparticles of various sizes were synthesized by the reprecipitation method[20] as described in Section 2.1. First, Indigo was dissolved in 25 mL DMSO, giving an indigo concentration of 0.5 mM. Then an indigo–DMSO solution (200 mL) was added to deionized water (20 mL) in a glass round-bottom flask and thoroughly mixed by magnetic vortexing stirring at 800 rpm for 5 minutes at a temperature of 25℃. The resulting mixture was a light blue, transparent dispersion with the appearance of a solution. To prepare indigo nanoparticles of larger size, the indigo–DMSO solution, the volumetric ratio of the organic solution to water was increased four times. The mixture again resulted in a blue transparent dispersion.

3.2.3 Characterisation of Indigo Nanoparticles

DLS measurements were performed using a Malvern Zetasizer Nano ZS (Malvern Instruments Ltd, Malvern, U.K.). Approximately 1mL of an indigo nanoparticle suspension that had been passed through a 0.2 μm filter (Whatman International Ltd., Kent, U.K.) was added to a glass cuvette before inserting the cuvette into the Zetasizer. The two different sized indigo nanoparticle suspensions were measured three times for each batch to ensure reproducibility.

3.2.4 Cyclic Voltammetry of Indigo Nanoparticles

The electrochemical experiments were performed at a temperature of 25℃ with a conventional three electrode setup using a μAutolab II potentiostat (Metrohm-Autolab BV, Netherlands) within a double Faraday cage for electrical noise reduction. Voltammetry data were collected by using GPES software. For drop-casting and voltammetric measurements experiment, a glassy carbon macroelectrode (3 mm diameter) was used as a working electrode, a saturated calomel electrode (SCE) as reference (Radiometer, Copenhagen), and a graphite rod as the counter electrode. The glassy carbon macroelectrode was modified by dropping a suspension of indigo nanoparticles onto the surface and letting the electrode dry under nitrogen. Cyclic voltammetry was conducted with the modified electrode in PBS buffer (PH = 6.8). All solutions were degassed thoroughly with nitrogen before scanning. The working electrode was polished between each experiment by using three grades of diamond spay (3, 1 and 0.1 microns) following by sonication in water and drying under nitrogen.

3.2.5 Electrochemical Sizing of Indigo Nanoparticles

Electrochemical sizing were performed as described in Section 2.4. The chronoamperometric recordings of indigo nanoparticles were performed with the same reference and counter electrodes used for the voltammetric measurements in Section 3.2.4, but the working electrode used was a carbon microelectrode (radius 5.5 mm). The carbon micro electrode diameter was calibrated electrochemically by analysing the steady state voltammetry of a 2.0 mM ferrocene in acetonitrile containing 0.1 M TBAP, using a diffusion coefficient for ferrocene of 2.30×10^{-9} m^2 s^{-1} at 298 K[21]. For the nano-impact

experiments, chronoamperometric scans of 5 s duration with a sampling time of 0.5 ms were recorded. “Signal Counter” developed by Dr. D Omanovic´ at Center for Marine and Environmental Research Zagreb, Croatia was used for detection and analysis of the impact spikes observed and OriginPro 8.5.1 for statistical analysis of the nanoparticle size.

3.3 Results and Discussion

In this section, cyclic voltammetry was applied to study the reduction of indigo nanoparticles drop cast on a glassy carbon electrode in in PBS buffer (pH = 6.8). Then the individual reduction of the indigo nanoparticles with two different sizes were characterised by using nano-impact experiments. Dynamic light scattering was also conducted to detect the size of the indigo nanoparticles in solution and compared with the data from electrochemical sizing.

3.3.1 DLS Characterization of Indigo Nanoparticles

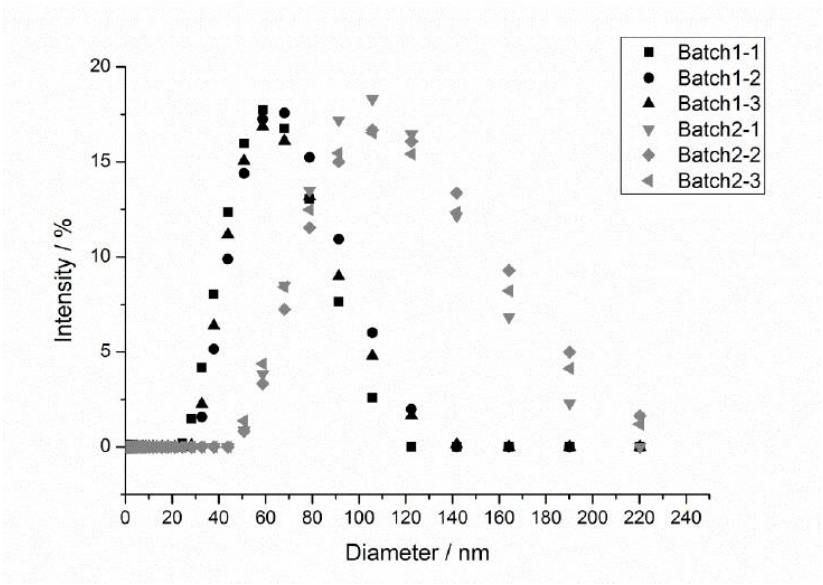


Figure 3.2 Size distributions of DLS measurements of indigo NPs of the two batches of different size (black: small indigo nanoparticles; grey: large indigo nanoparticles). Three measurements were made on each batch.

DLS measurements were performed to characterize the indigo nanoparticles suspensions with two different sizes and repeated three times for each batch. The size distributions of these synthesised indigo nanoparticles are shown in Figure 3.2 , giving an average size of 66 nm and 107 nm for the "small" and the "large" indigo nanoparticles respectively.

3.3.2 Cyclic Voltammetry of Indigo Nanoparticles

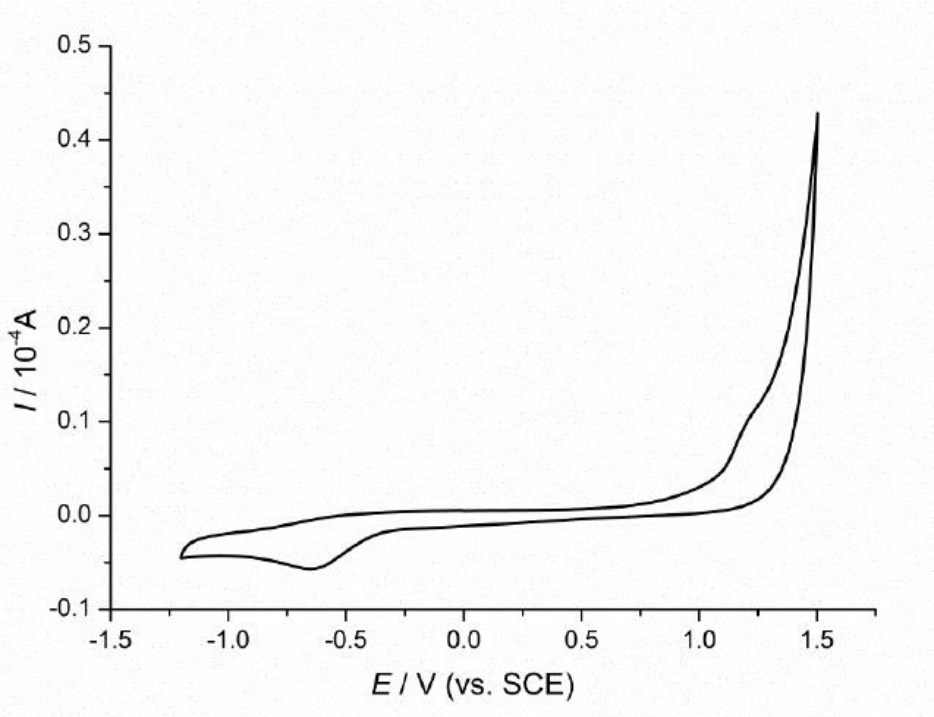
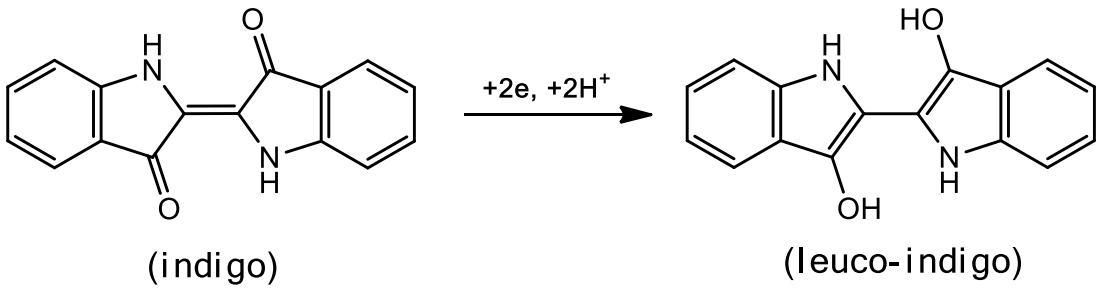


Figure 3.3 Cyclic voltammetry performed using an indigo NP-modified carbon macroelectrode in a solution of PBS buffer (pH = 7).

First, to determine the reduction potential of indigo NPs for impacting experiments, cyclic voltammetry (CV) was performed by using an indigo-modified carbon macroelectrode. A known amount of the suspension of indigo nanoparticles was dropcasted on the carbon macroelectrode to modify the electrode, and left to dry under a N_2 atmosphere. Cyclic

voltammograms were recorded with the modified carbon macroelectrode immersed in phosphate-buffered saline (PBS) buffer, yielding a reduction feature of indigo NPs associated with the known reaction shown in Scheme 3.1[22]. The cyclic voltammogram demonstrates a significant reduction peak of indigo NPs at -0.650 V as shown in Figure 3.3.



Scheme 3.1 Likely mechanism of indigo reduction

3.3.3 Electrochemical Sizing of Indigo Nanoparticles

Next, nano-impact experiments were attempted. To make sure the indigo nanoparticles undergo fully two electron transfer per monomer unit during their reduction, the potential used for reduction of indigo NPs for impact experiments was then selected as -0.70 V. A carbon microelectrode was placed in 0.1m PBS buffer solution (pH = 6.8) and a known concentration of predispersed indigo NPs added. The electrode potential was held at -0.7 V. Under potentiostatted conditions (between -0.7 V and -0.9 V), reductive (Faradaic) spikes from individual indigo NPs were observed (Figure 3.4(a)), showing for the first time that direct reduction of individual organic nanoparticles during random collision

events can be observed. As expected, the onset of these Faradaic spikes was found dependent on the reduction potential. By reducing the reduction potential (for example, to -0.3 V), no spikes were observed, showing those spikes result from the Faradaic reduction of indigo NPs. Increasing the amount of added indigo NPs increased the frequency of spikes (Figure 3.5). This further suggests that the spikes correspond to Faradaic reduction of indigo NPs. Further, to quantify the size of indigo NPs, an equation between the diameter and the charge associates with single indigo impacts can be established assuming that indigo NPs are spherical (diameter, D_{np}), and the charge Q passed as a result of complete reduction of single indigo NPs is:

$$D_{np} = 2 \times \sqrt[3]{\frac{3MQ}{4nF\pi\rho}} \qquad \text{(Eqn 3.1)}$$

where M is the molar mass of indigo, ρ is the density of indigo[23] and F is the Faraday constant. The parameter n is the number of electrons transferred of indigo NPs reduction (n = 2) as in Scheme 3.1.

Multiple repeats were performed such that total number of recorded impact events was greater than 300. By analyzing all these impact spikes, the size distribution of the indigo NPs was derived, as shown in Figure 3.4(b). The mean diameter and standard deviation of indigo NPs were determined to be 68 ± 23 nm. The results demonstrated for the first time the electrochemical sizing of organic nanoparticles can be quantified.

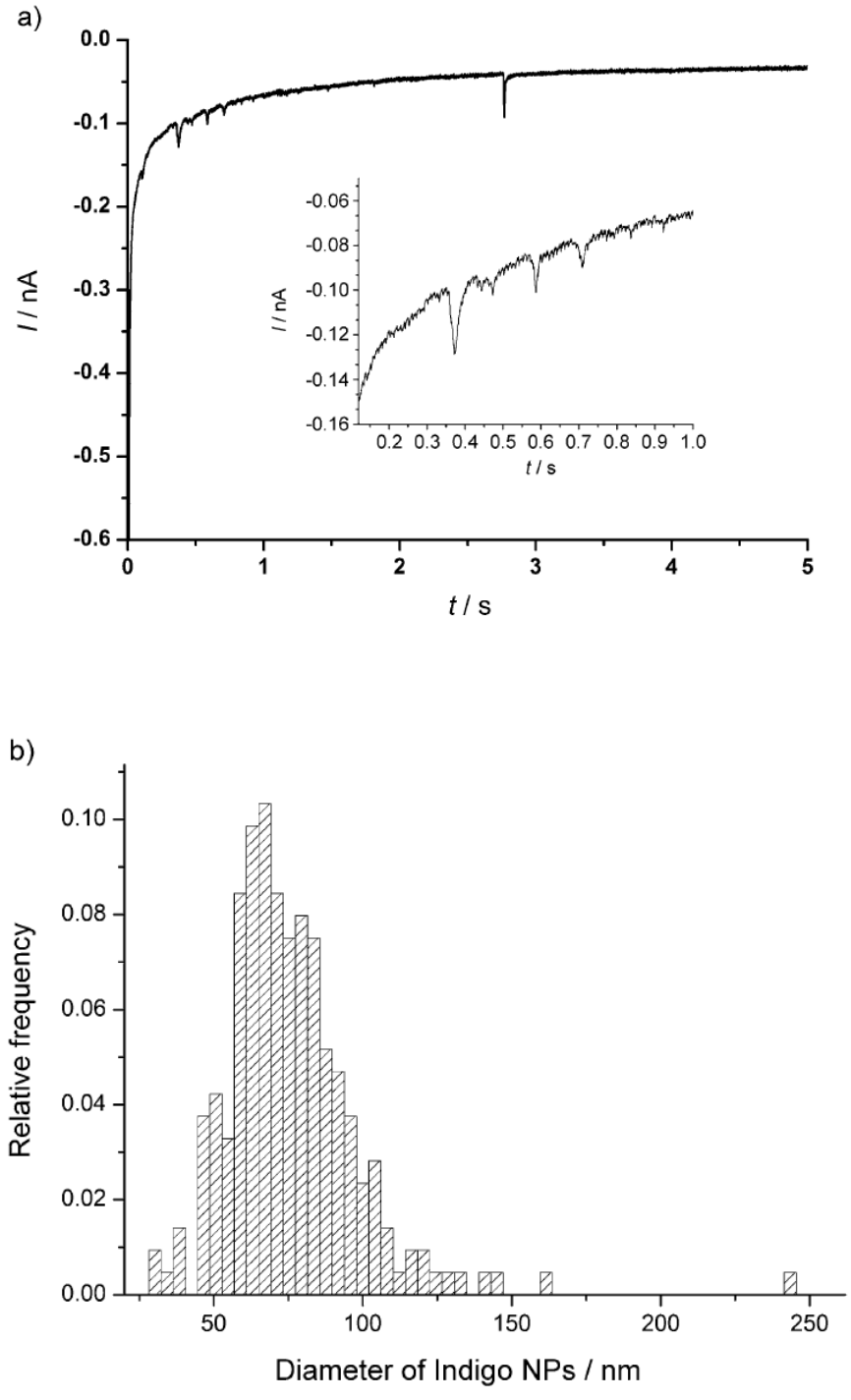


Figure 3.4 (a) Chronoamperometric profiles showing reductive Faradaic spikes of indigo NPs in PBS buffer (pH = 6.8) at -0.70 V versus saturated calomel electrode (SCE). The inset shows the detailed impact spikes. (b) Distribution of the NP diameter derived from a charge per current spike according to Equation 3.1.

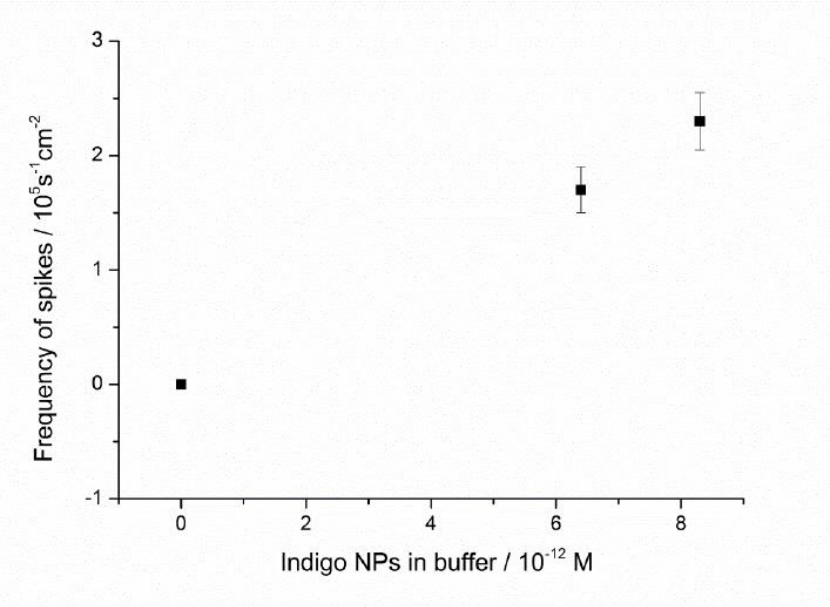


Figure 3.5 Frequency of spikes as a function of the number concentration of indigo NPs.

To verify our results from the electrochemical sizing, the size of indigo NPs from the same batch was compared with the dynamic light scattering (DLS) data. There was an excellent agreement of the resulting sizing distribution obtained from our electrochemical sizing and the DLS analysis, as shown in Figure 3.6.

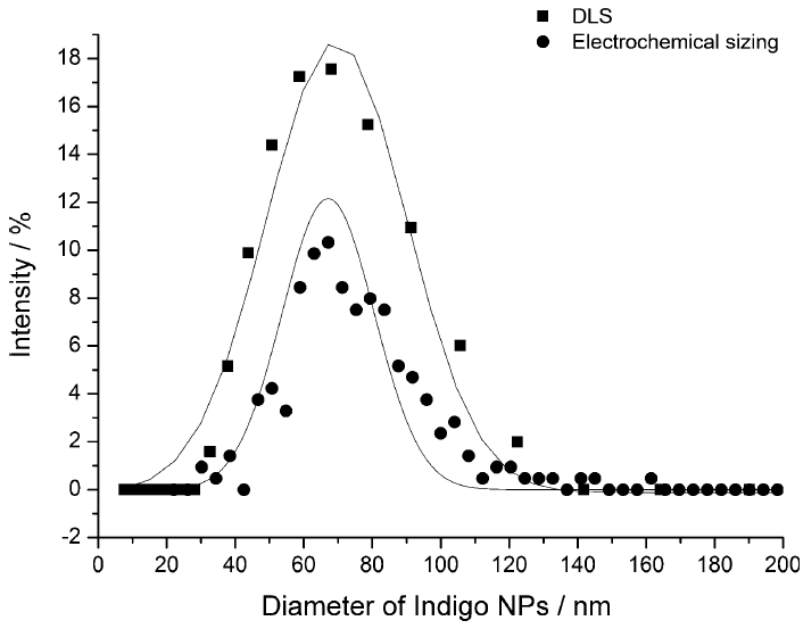


Figure 3.6 Indigo NPs size distribution obtained from electrochemical sizing experiment (dots) and DLS analysis (squares) with the same batch of "small" indigo nanoparticles.

To further confirm our electrochemical sizing results of indigo NPs, analogous experiments were carried out to size a different batch of indigo NPs, this time of larger size. These were synthesised by increasing the amount of indigo solution used in the reprecipitation, and as expected the size of indigo NPs was increased. The size of indigo NPs was then electrochemically characterized by adding the indigo NPs into a buffer solution and reductive spikes of the indigo NPs of the batch were again observed and subsequently analysed. Figure 3.7 shows reductive Faradaic spikes of the indigo NPs of larger size in PBS buffer (pH = 6.8) at -0.7 V vs. SCE. Again no reductive Faradaic spikes of indigo NPs were seen at -0.3 V vs. SCE. The size distribution from indigo NPs were analysed from the charges of those individual reductive spikes with a mean diameter and standard deviation determined to be 107 ± 35 nm (Figure 3.8), again showing an excellent agreement with pervious DLS sizing results of the large indigo nanoparticles (107 nm).

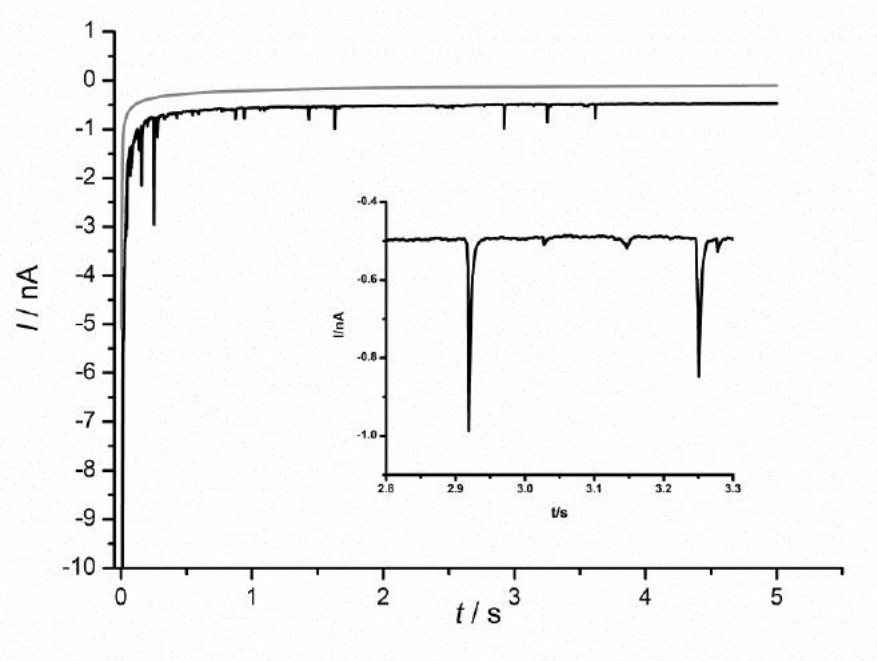


Figure 3.7 Chronoamperometric profiles showing reductive Faradaic spikes of indigo NPs of larger size (batch 2) in PBS buffer (pH = 6.8) at -0.7 V vs. SCE. The inset shows the detailed impact spikes; Chronoamperometric profiles at -0.3 V vs. SCE (top line; grey colour) showing no reductive Faradaic spikes of indigo NPs.

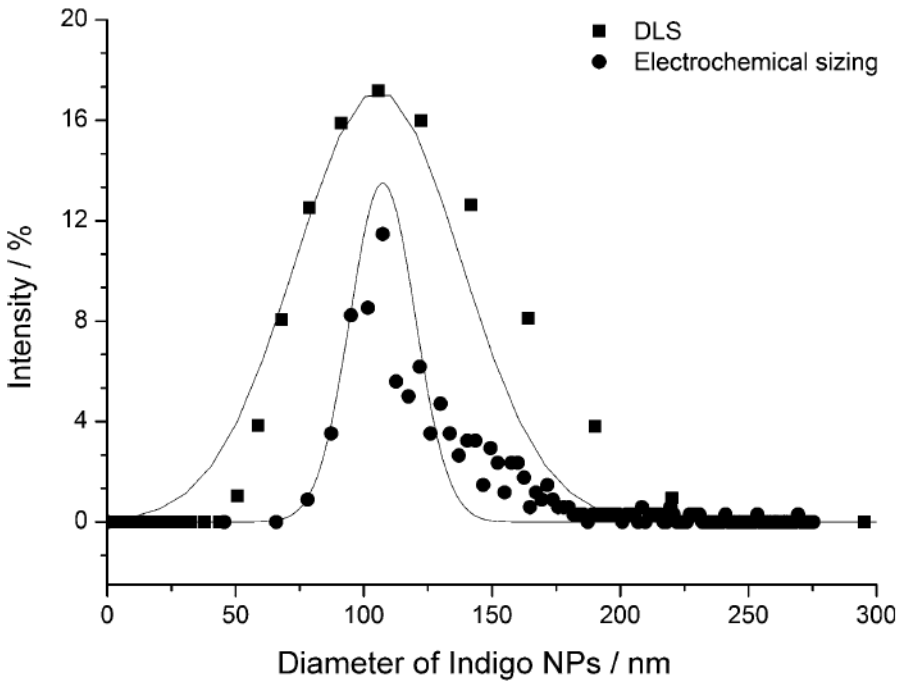


Figure 3.8 Indigo NPs size distribution obtained from electrochemical sizing experiment (dots) and DLS analysis (squares) of the batch of "large" indigo nanoparticles.

3.4 Conclusions

Herein we have shown for the first time, that direct electrochemical sizing of organic NPs is feasible and quantitative. As the electrochemical sizing enables the simultaneously sizing of individual organic NPs, we expect that this sizing strategy will be applied to determine the size range of organic NPs used in drug delivery and in biological environments, which are difficult to characterize in situ by other sizing methods currently available. This methodology is currently applied to characterize redox organic nanoparticles; however, this may further open a new strategy to electrochemically

characterize a wide range of organic nanoparticles including antibodies and proteins through surface modified redox active groups.

Indigo nanoparticles in the form of a monomeric organic solid were successfully sized and detected by the nano-impacts method. The next two chapters focus on the electrochemical detection and characterization of polymeric organic nanoparticles.

References

1. D. Horn and J. Rieger, *Angewandte Chemie International Edition*, 2001, **40**, 4330-4361.
2. K. R. Chu, E. Lee, S. H. Jeong and E.-S. Park, *Archives of Pharmacal Research*, 2012, **35**, 1187-1195.
3. V. P. Chauhan, T. Stylianopoulos, J. D. Martin, Z. Popović, O. Chen, W. S. Kamoun, M. G. Bawendi, D. Fukumura and R. K. Jain, *Nature Nanotechnology*, 2012, **7**, 383-388.
4. H.-B. Fu and J. N. Yao, *Journal of the American Chemical Society*, 2001, **123**, 1434-1439.
5. Z. Schnepp, *Angewandte Chemie International Edition*, 2013, **52**, 1096-1108.
6. J. Zhu, S. K. Ozdemir, Y. F. Xiao, L. Li, L. He, D.-R. Chen and L. Yang, *Nature Photonics*, 2010, **4**, 46-49.
7. Y. Hennequin, C. P. Allier, E. McLeod, O. Mudanyali, D. Migliozzi, A. Ozcan and J.-M. Dinten, *ACS Nano*, 2013, **7**, 7601-7609.
8. R. P. Carney, J. Y. Kim, H. Qian, R. Jin, H. Mehenni, F. Stellacci and O. M. Bakr, *Nature Communications*, 2011, **2**, 335.
9. Y. G. Zhou, N. V. Rees and R. G. Compton, *Angewandte Chemie International Edition*, 2011, **50**, 4219-4221.
10. E. J. Stuart, Y. G. Zhou, N. V. Rees and R. G. Compton, *RSC Advances*, 2012, **2**, 6879-6884.
11. Y. G. Zhou, N. V. Rees and R. G. Compton, *Chemical Communications*, 2012, **48**, 2510-2512.
12. E. Stuart, N. Rees, J. Cullen and R. Compton, *Nanoscale*, 2013, **5**, 174-177.

13. Y. G. Zhou, N. V. Rees and R. G. Compton, *Physical Chemistry Chemical Physics*, 2013, **15**, 761-763.

14. Y. G. Zhou, N. V. Rees, J. Pillay, R. Tshikhudo, S. Vilakazi and R. G. Compton, *Chemical Communications*, 2011, **48**, 224-226.

15. A. Boika, S. N. Thorgaard and A. J. Bard, *The Journal of Physical Chemistry B*, 2012, **117**, 4371-4380.

16. J. H. Park, S. N. Thorgaard, B. Zhang and A. J. Bard, *Journal of the American Chemical Society*, 2013, **135**, 5258-5261.

17. M. Shen, X. H. Zhu and A. J. Bard, *Journal of the American Chemical Society*, 2013, **135**, 8868-8873.

18. A. B. Nepomnyashchii, R. J. Ono, D. M. Lyons, J. L. Sessler, C. W. Bielawski and A. J. Bard, *The Journal of Physical Chemistry Letters*, 2012, **3**, 2035-2038.

19. Y. L. Chang, R. E. Palacios, F.-R. F. Fan, A. J. Bard and P. F. Barbara, *Journal of the American Chemical Society*, 2008, **130**, 8906-8907.

20. A. Johnson-Buck, G. Kim, S. Wang, H. J. Hah and R. Kopelman, *Molecular Crystals and Liquid Crystals*, 2009, **501**, 138-144.

21. E. I. Rogers, D. S. Silvester, D. L. Poole, L. Aldous, C. Hardacre and R. G. Compton, *The Journal of Physical Chemistry C*, 2008, **112**, 2729-2735.

22. A. M. Bond, F. Marken, E. Hill, R. G. Compton and H. Hügel, *Journal of the Chemical Society, Perkin Transactions 2*, 1997, 1735-1742.

23. P. Schaaf, B. Senger and H. Reiss, *The Journal of Physical Chemistry B*, 1997, **101**, 8740-8747.

Chapter 4

Electrochemical Detection and Characterization of Polymeric Nanoparticles

Individual organic nanoparticles were first studied using the electrochemical method as described in Chapter 3 so opening a new door to the quantitative analysis of nanoparticles. In this chapter, we investigate the detection and characterization of polymeric nanoparticles using electrochemistry. We study poly (N-vinylcarbazole) nanoparticles (PVK NPs) as a model system. This material was synthesized by the reprecipitation method. Cyclic voltammograms (CVs) were recorded using a PVK NPs modified glassy carbon electrode to quantify the amount of nanoparticles deposited on the electrode surface and the number of electrons transferred per PVK monomer was characterized by drop-casting different amounts of PVK NPs onto the surface of the working electrode. Stick and strip experiments were then conducted, which involved PVK nanoparticle immobilisation on the electrode surface and subsequent oxidation, yielding a quantitative determination of the amount of PVK nanoparticles adhering to the electrode surface, so enabling the rapid detection of polymeric nanoparticles in aqueous solution. A linear relationship of the stripping signal on sticking time was observed for PVK NPs of different sizes for different sticking times. It shown for the first time, that using this "stick and sense" method, polymeric nanoparticles in aqueous solution can be immobilised, pre-concentrated and quantified. This work presented here was published in article *Electroanalysis*, 26, (2014), 248-253.

4.1 Introduction

Organic nanoparticles have attracted significant attention in the past few years because of their large range of molecular structures[1], the capability of tailoring their binding affinity towards various materials[2] and their wide use in bio-imaging and biomedicine[3]. However, the research of organic nanoparticles, including polymeric nanoparticles, is still at a very early stage due to their complex physical and chemical properties[4]. More recently, organic nanoparticles have found high impact applications in nanomedicine to deliver hydrophobic drugs to target cells[5], and to act as carriers for the controlled release of drugs under specific stimuli[6]. Alongside their synthesis and wide-spread use, possible concerns have been raised regarding possible outcomes for both humans and environmental systems[7], particularly resulting from their inevitable release into the environment[8]. Therefore, there is an urgent demand to real-time detect and characterize the quantities of nanoparticles which requires an efficient technique for nanoparticle detection and quantification. Microscopic and spectroscopic techniques were widely used for nanoparticle characterization and detection[9, 10]. However, optical methods exhibit their own distinct disadvantages, such as high cost, time-consuming sample preparation and complex optics.

Electrochemistry as an alternative method to optical methods provides an efficient and cost-effective approach for characterization of nanoparticles (NPs)[11-19]. In this chapter, the electrochemical detection and characterization of polymeric nanoparticles is studied by using the polymer, poly (N-vinylcarbazole) (PVK) as a model system. Figure 4.1 shows the structure of a PVK molecule. The number of electrons transferred per PVK monomer on the electrode was characterized using a PVK nanoparticle modified glassy carbon electrode. Direct detection of polymeric nanoparticles in aqueous solution was realized by

locating an electrode in a nanoparticle containing aqueous solution and subsequent oxidative sensing, enabling quantitative determination of the amount of PVK nanoparticles adhering to the electrode surface. In this way, it has shown for the first time that polymeric nanoparticles in aqueous solution can be immobilised, pre-concentrated and quantified using electrochemistry based analysis. As the same time, we highlight the limitation of NTA (Nanoparticle Tracking Analysis) for characterization of organic nanoparticles for this task.

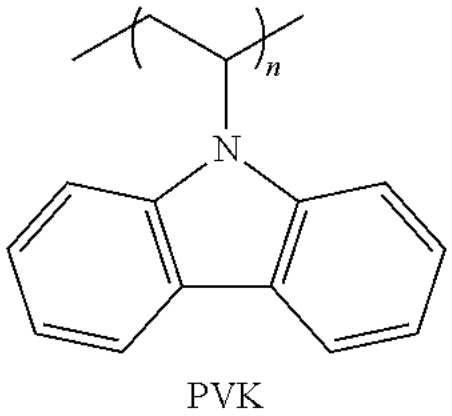


Figure 4.1 Structure of a PVK molecule

4.2 Experimental Section

4.2.1 Chemicals and Materials

Poly (N-vinylcarbazole) (PVK, molecular weight M = 40,000) were obtained from Polysciences (Warrington, PA, USA). Tetrahydrofuran (THF, 99.9%, anhydrous) were purchased from Aldrich and used as received. Unless stated otherwise, all chemicals in this work were acquired from Sigma-Aldrich. All solutions were made up using ultrapure

water of resistivity 18.2 MΩ cm (Millipore) at 25°C and degassed thoroughly with N_2 (oxygen-free, BOC Gases plc) before use.

4.2.2 Synthesis of PVK Nanoparticles

PVK nanoparticles of various sizes were synthesized by the reprecipitation method as described[20] in Section 2.1. A known amount of PVK powder was dissolved in 20 mL THF solution. Then 100 μL PVK/THF solution was injected into 25 mL de-ionized water under vigorously stirring by magnetic vortexing at 800 rpm for 5 minutes. The nanoparticles suspension was subjected to sonication for 30 minutes at room temperature. For synthesis of nanoparticles of different sizes, PVK nanoparticles were prepared by injecting PVK/THF solution of different concentrations (1.4 mM, 10 mM and 27 mM) as shown in Figure 4.2.

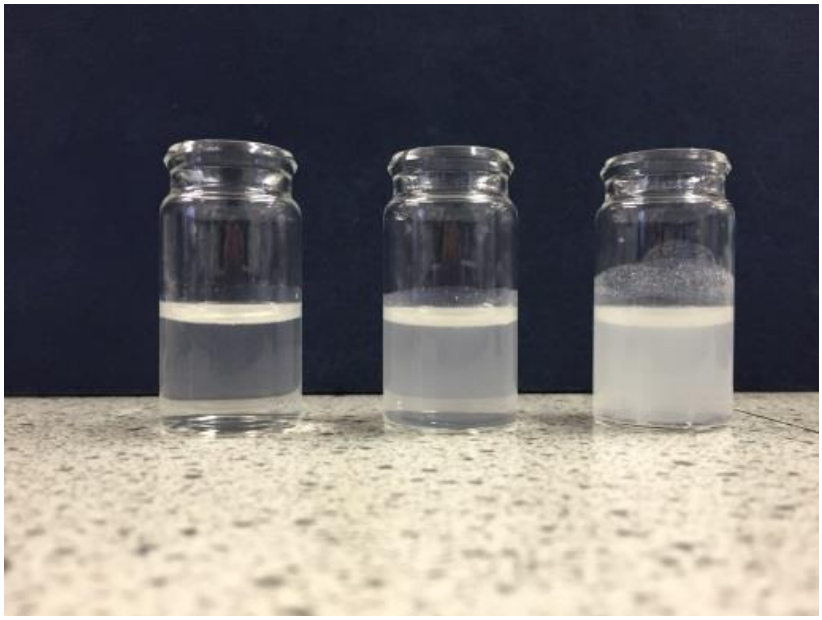


Figure 4.2 Three different concentrations of PVK nanoparticles in suspensions

4.2.3 Characterization of PVK Nanoparticles

A NanoSight LM10 (NanoSight Limited, Amesbury, UK) was used to carry out nanoparticle tracking analysis (NTA). A 300 µL sample of the PVK nanoparticle solution to be studied was syringed into the viewing unit of the NanoSight and a red (638 nm) laser was used to illuminate the particles so they could be tracked. Measurements were recorded at 25℃ and the nanoparticles were tracked for duration of 10 s, 30 s and 60 s. NanoSight NTA software was used to analyse the tracks of the nanoparticles in order to gain a particle size distribution.

4.2.4 Electrochemical Characterization of PVK Nanoparticles

The instrumentations for the electrochemical experiments used are same as those in Section 3.2.4. For cyclic voltammetry measurements a glassy carbon macroelectrode (GC, diameter 3.0 mm) was used as the working electrode, a saturated calomel electrode (SCE) as the reference electrode while a Pt mesh acted as a counter electrode. A glassy carbon macroelectrode was modified by dropping varying amounts of a PVK NPs suspension onto the surface and letting the electrode dry under nitrogen. Solutions were degassed thoroughly with nitrogen before scanning and a nitrogen blanket was maintained above the solution throughout the experiment. Cyclic voltammetry was conducted following drying process with scan rate from 20 mV/s up to 200 mV/s in 1.0 M $HClO_4$. Before each voltammetric scan the electrode was polished using three grades of diamond spray (3, 1 and 0.1 microns) before sonication in water and drying with nitrogen.

4.2.5 PVK Nanoparticle Sticking

Sticking and stripping measurements were performed with the same reference and counter electrode used for the drop-casting experiment above, but the working electrode utilized was a carbon microelectrode (radius 5 µm). *In situ* immobilisation and thus enrichment of PVK NPs on an electrode was achieved by nanoparticle sticking experiments. The carbon microelectrode was immersed in a suspension of PVK NPs (known monomer concentration) for a certain period of time (0-60 min) and the subsequent oxidative sensing (see "PVK nanoparticle sensing") was employed to quantify the amount of adherent PVK NPs. PVK NPs suspension with monomer concentrations of 1.1×10^{-4} mol/L, 4.2×10^{-5} mol/L and 5.8×10^{-6} mol/L, respectively were used for sticking experiments.

4.2.6 PVK Nanoparticle Sensing in Aqueous Solution

Following the sticking experiments, the electrode was transferred for stripping to a freshly prepared aqueous solution of 1 M $HClO_4$. Cyclic voltammetry was recorded between 0 and + 1.7 V *versus* SCE reference electrode at a scan rate of 100 mV/s. The potential region was chosen since this region was found to be suitable for quantitative oxidation of PVK NPs in 1 M $HClO_4$, as determined by drop-casting experiments.

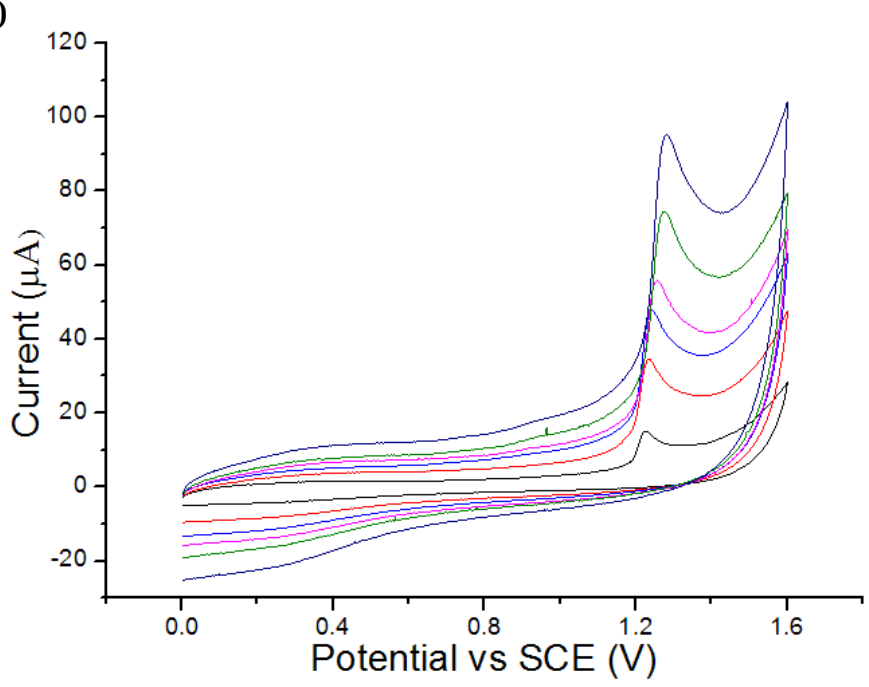
4.3 Results and Discussion

4.3.1 NTA Characterisation of PVK Nanoparticles

Characterization of the as-produced nanoparticles within solution was undertaken using nanoparticle tracking analysis (NTA, LM10, NanoSight Ltd.). It should be commented that regular characterization techniques such as electron microscopy are not applicable for use with organic polymeric nanoparticles due to requirement of them being studied ex-situ, hence, the size and morphology of the particles may be altered dramatically from that found in solution. From the NTA studies the mean particle diameter was found to be ~30 nm. It should be commented that the mean size determined by NTA is on the lower limit of detection for such particles, due to the relatively low light scattering, hence the values of 30 nm should be approached with caution[21]. Sizing of polymeric nanoparticles with the electrochemical method and with dynamic light scattering is illustrated in Chapter 5.

4.3.2 Determination of Electrons Transfer to Poly (N-vinylcarbazole) Nanoparticles

(a)



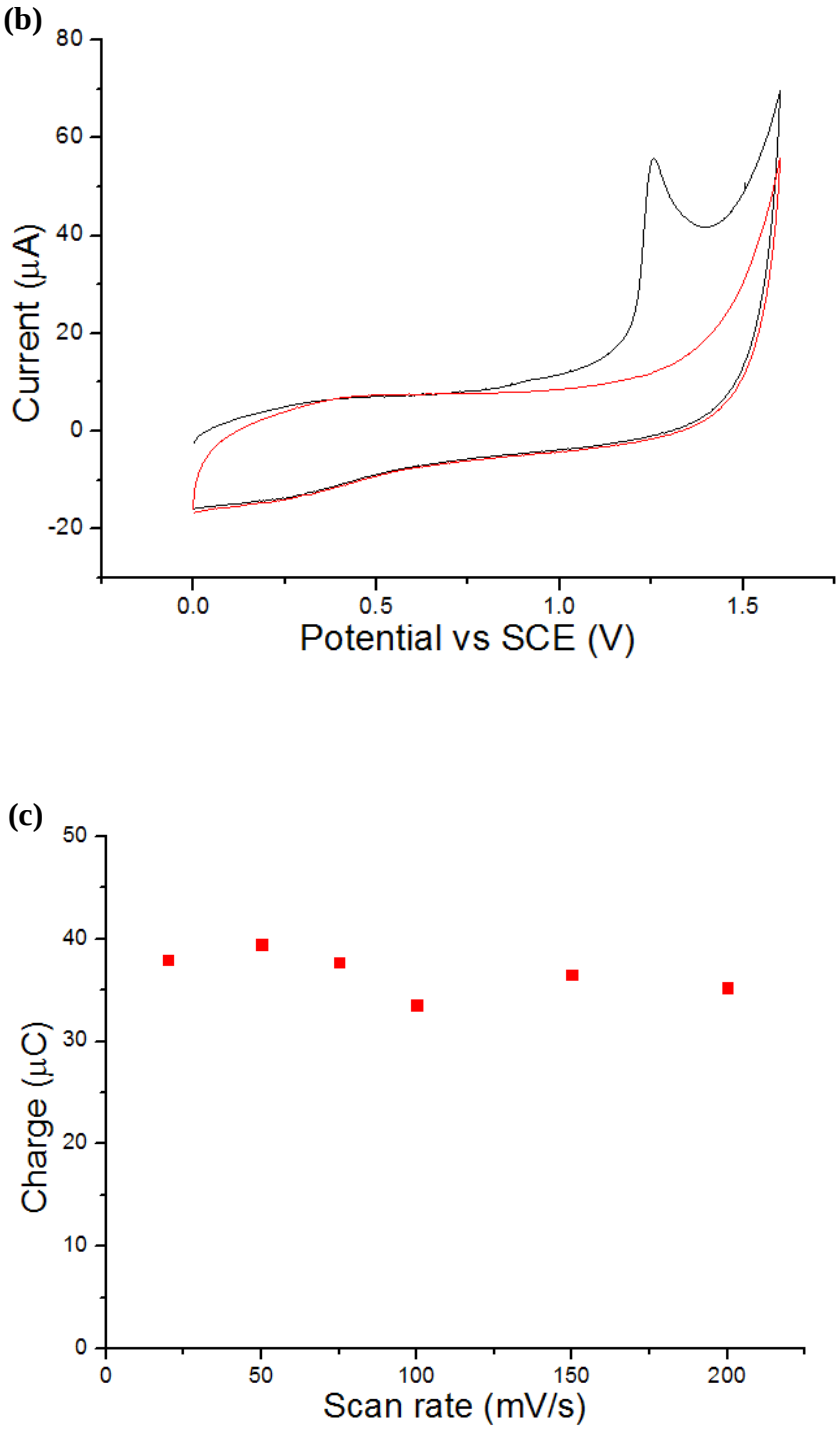


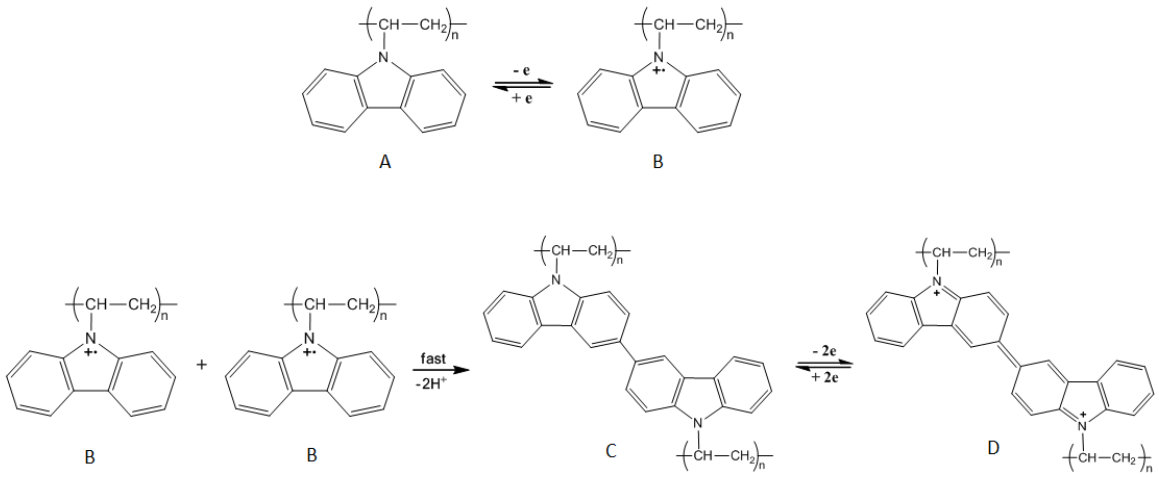
Figure 4.3 (a) Cyclic voltammograms recorded for a GC macroelectrode modified with PVK NPs in 1.0 M $HClO_4$ at different scan rate from 20 mV/s to 200 mV/s (from the top: 200 mV/s, 150 mV/s, 100 mV/s, 75 mV/s, 50 mV/s, 20 mV/s); (b) The first two scans (black: first scan; red: second scan) of cyclic voltammograms recorded for a GC macroelectrode modified with 2 μL of PVK NPs suspension (monomer concentration:1.1×10^{-4} mol/L) in 1.0 M $HClO_4$ at a scan rate of 100 mV/s; (c) Plots of charge (integrated from Figure 4.2 (a)) *versus* scan rates from 20 mV/s to 200 mV/s.

Cyclic voltammograms (CVs) were recorded for a GC macroelectrode modified with PVK NPs immersed in 1.0 M $HClO_4$ at different scan rates, yielding a well-defined sharp oxidation peak associated with PVK oxidation[22], as shown in Figure 4.3(a). No further peak was observed in the consecutive scan, indicating the complete oxidation of the PVK NPs in the first scan, as shown in Figure 4.3(b).

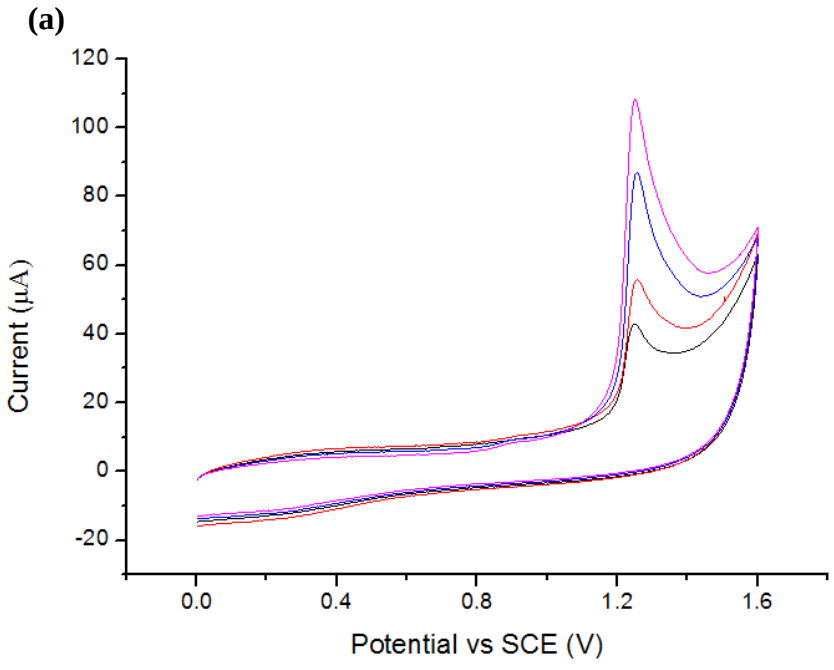
Also, no signal was recorded on a bare glassy carbon electrode which confirms that the stripping charge is due to the immobilised PVK nanoparticles. The charge associated with the oxidation was thus obtained by integrating the oxidation peak of the corresponding PVK oxide. The charge derived from cyclic voltammograms (CV) recorded by different scan rates 20 mV/s to 200 mV/s is plotted against scan rates in Figure 4.3(c). It confirms that the charge is independent of scan rate. Therefore, the quantification of the amount of PVK NPs immobilised upon drop-casting on the glassy carbon surface has been carried out using this anodic oxidation method.

The electron transfer of PVK NPs was studied by applying different loadings directly onto the surface of the working electrode multiple times. The modified GC electrode was then anodically scanned, revealing consistent oxidation peaks at around +1.25V, as shown in Figure 4.4(a). The anodic peak charge (obtained from the integration of the peak area) increases linearly by increasing the PVK NPs loadings on the electrode surface as plotted in Figure 4.4(b). The gradient of this plot can be calculated from this plot, indicating that ~1.75 electrons are transferred per monomer. The result is in agreement with the previous electrochemical studies of PVK[22], involving the equilibria for oxidation of PVK as shown in Scheme 4.1 and suggested that the electroanalysis of the majority of PVK NPs underwent a two electron transfer process (from A to D). The deviation from exactly 2

electron transfer may indicate that following a rapid one electron-transfer process by conversion of A into B, the conversion of B to C then D may happen on a longer time-scale so that the whole oxidisation process is partly governed by the rate of the PVK cross-linking process.



Scheme 4.1 Likely mechanism of PVK oxidation[22].



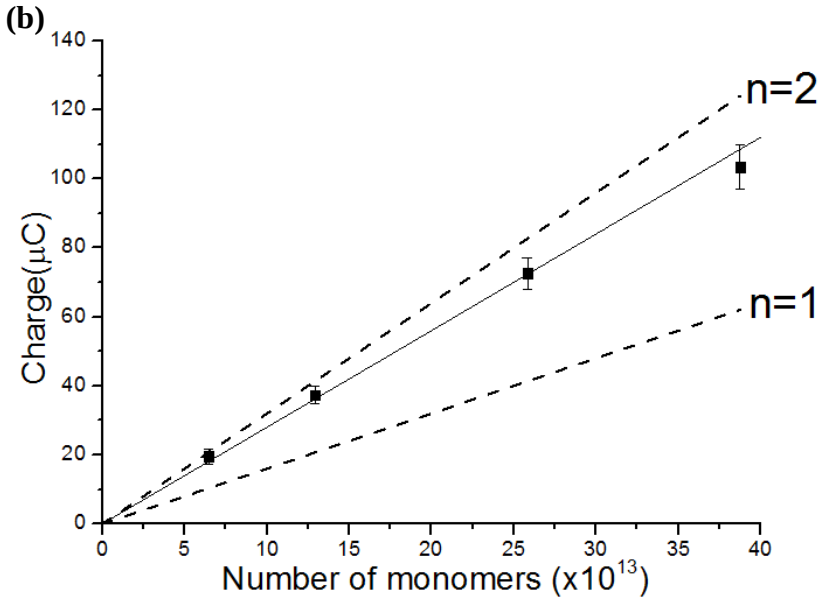
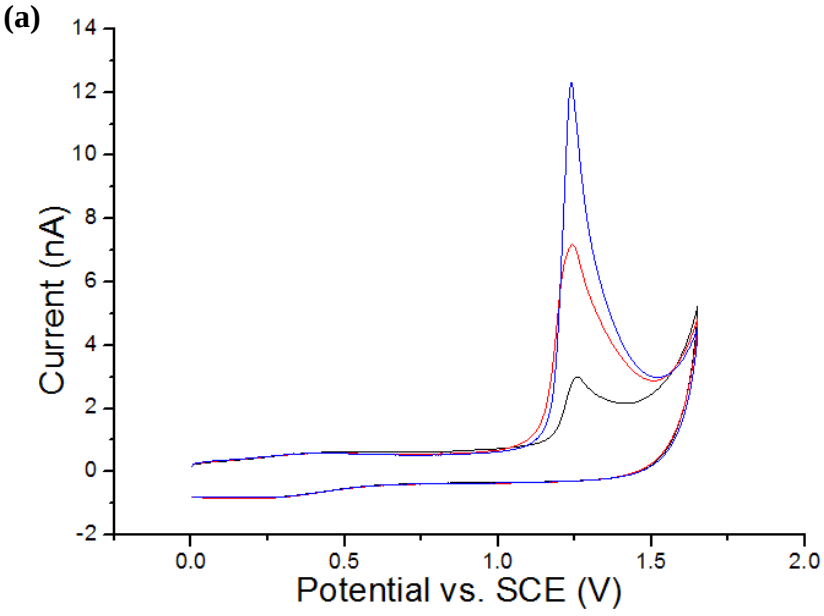


Figure 4.4(a) Cyclic voltammograms recorded for a GC macroelectrode modified with PVK NPs of various monomer moles: 1.1×10^{-10} mol (black line), 2.2×10^{-10} mol (red line), 4.4×10^{-10} mol (blue line) and 6.6×10^{-10} mol (magenta) in 1.0 M $HClO_4$ at a scan rate of 100 mV/s; (b) Linear relation between the anodic peak charge (obtained from the integration of the peak area from (a)) and the PVK NPs loadings on the electrode surface, and plotted lines of charge *versus* number of monomers for one or two electrons transferred (n = 1 and n = 2) per monomer of PVK NPs.

4.3.3 Detection of Organic Poly (N-vinylcarbazole) Nanoparticles Using the Sticking and Sensing Method



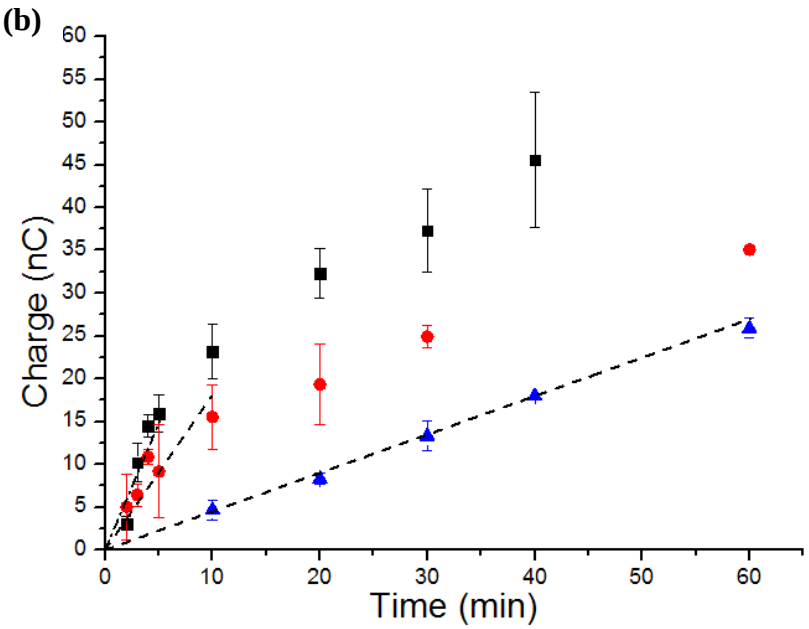


Figure 4.5(a) showing the oxidative stripping of PVK NPs at a scan rate of 100 mV/s from a carbon microelectrode immersing in a suspension containing PVK NPs of 1.1×10^{-4} mol/L monomer concentration for various sticking times (min): 2 (black), 3 (red), 4 (blue); (b) Plots of the stripping charge *versus* sticking time from 2min to 60 min for a carbon microelectrode in PVK NPs suspension of different monomer concentrations of 1.1×10^{-4} mol/L (black dots), 4.2×10^{-5} mol/L (red dots) and 5.8×10^{-6} mol/L (blue dots). Mean value and standard deviation of each data point were obtained from at least three experiments.

To detect the PVK NPs in aqueous solution, PVK NPs sticking experiments were performed by immersing the modified electrode in a suspension of synthesized PVK NPs for various sticking times. In this way, coverage of PVK NPs result from the irreversible adsorption of the NPs associated with collision of the NPs with the electrode by virtue of their Brownian motion. The resulting oxidation curves of stripping by CV are shown in Figure 4.5(a). Analogous experiments were also carried out for synthesized PVK NPs with different monomer concentrations. The fact that no anodic peak/charge was observed for the control exposure (0 min), while a quantifiable anodic peak/charge was found for sticking times of 2 min or longer, suggests that the observed peaks are due to the continuous adhering of PVK NPs to the electrode and subsequent oxidative stripping from the electrode. It showed for the first time, that using this sticking and sensing method,

organic nanoparticles in aqueous solution can be immobilised, pre-concentrated and quantified.

Increasing monomer concentration of PVK for re-precipitation increases the size of PVK NPs, according to the literature[20]. Figure 4.5(b) shows a relationship of the stripping charge *versus* sticking time up to 60 min for PVK NPs synthesized with different monomer concentrations. A linear relationship between sticking time and oxidative charge was observed up to 60 min for PVK NPs with low monomer concentration of 5.8×10^{-6} mol/L (small size). The corresponding linear fit suggests an increase of sticking charge of about 4.5×10^{-10} C per min of sticking time for PVK NPs. This may also indicate that the electrode may have a relatively large surface coverage for PVK NPs, where the affinity of the suspended nanoparticles on the electrode surface is not reduced over electrode exposure times.

It is interesting that a linear relationship was observed only up to 5 min, and 10 min for PVK NPs with high monomer concentration of 1.1×10^{-4} mol/L and 4.2×10^{-5} mol/L, respectively (large sizes) suggesting that in this case, a linear increase between the number of larger nanoparticles sticking to the surface within a limited period of time is observed when binding sites on the electrode surface are relatively unpopulated. As the binding sites approaches saturation over time, a Langmuir type adsorption, and thus a non-linear dependence, is expected.

4.4 Conclusions

In this chapter, the direct electrochemical detection and characterization of polymeric nanoparticles is studied. The number of electrons transferred per PVK monomer was characterized by drop-casting different amounts of PVK NPs onto the surface. Sticking and sensing experiments were conducted for subsequent detection and quantification of PVK nanoparticles, which involves PVK nanoparticles immobilisation on the electrode surface and subsequent oxidative stripping, yielding a quantitative determination of the amount of PVK nanoparticles adhering to the electrode surface, to enable quick detection of organic nanoparticles in aqueous solution. It demonstrated that using this sticking and sensing method, organic nanoparticles in aqueous solution can be immobilised, pre-concentrated and quantified. This shows promise for electrochemical methods to characterize and detect polymer and organic nanoparticles.

The following chapter describes the oxidative doping of single PVK nanoparticles by using nano-impacts technique which has potential to significantly characterize and size the doped organic nanoparticles and can offer information of individual polymeric nanoparticles.

References

1. H. Kasai, T. Murakami, Y. Ikuta, Y. Koseki, K. Baba, H. Oikawa, H. Nakanishi, M. Okada, M. Shoji and M. Ueda, *Angewandte Chemie*, 2012, **124**, 10461-10464.
2. M. Oh and C. A. Mirkin, *Nature*, 2005, **438**, 651-654.
3. R. N. Grass, E. K. Athanassiou and W. J. Stark, *Angewandte Chemie International Edition*, 2007, **46**, 4909-4912.
4. D. Horn and J. Rieger, *Angewandte Chemie International Edition*, 2001, **40**, 4330-4361.
5. Y. Namiki, T. Namiki, H. Yoshida, Y. Ishii, A. Tsubota, S. Koido, K. Nariai, M. Mitsunaga, S. Yanagisawa and H. Kashiwagi, *Nature Nanotechnology*, 2009, **4**, 598-606.
6. R. Tong, H. D. Hemmati, R. Langer and D. S. Kohane, *Journal of the American Chemical Society*, 2012, **134**, 8848-8855.
7. M. Ahamed, M. S. AlSalhi and M. Siddiqui, *Clinica Chimica Acta*, 2010, **411**, 1841-1848.
8. A. D. Maynard, R. J. Aitken, T. Butz, V. Colvin, K. Donaldson, G. Oberdörster, M. A. Philbert, J. Ryan, A. Seaton and V. Stone, *Nature*, 2006, **444**, 267-269.
9. B. Cho, S. G. Lee, H. G. Woo and H. Sohn, *Journal of Nanoscience and Nanotechnology*, 2013, **13**, 384-387.
10. J. Zhu, S. K. Ozdemir, Y. F. Xiao, L. Li, L. He, D.-R. Chen and L. Yang, *Nature Photonics*, 2010, **4**, 46-49.
11. Y. G. Zhou, N. V. Rees and R. G. Compton, *Angewandte Chemie International Edition*, 2011, **50**, 4219-4221.

12. E. J. Stuart, Y. G. Zhou, N. V. Rees and R. G. Compton, *RSC Advances*, 2012, **2**, 6879-6884.

13. Y. G. Zhou, N. V. Rees and R. G. Compton, *Chemical Communications*, 2012, **48**, 2510-2512.

14. E. Stuart, N. Rees, J. Cullen and R. Compton, *Nanoscale*, 2013, **5**, 174-177.

15. Y. G. Zhou, N. V. Rees and R. G. Compton, *Physical Chemistry Chemical Physics*, 2013, **15**, 761-763.

16. K. Tschulik, B. Haddou, D. Omanović, N. V. Rees and R. G. Compton, *Nano Research*, 2013, **6**, 836-841.

17. M. Shen, X. H. Zhu and A. J. Bard, *Journal of the American Chemical Society*, 2013, **135**, 8868-8873.

18. A. B. Nepomnyashchii, R. J. Ono, D. M. Lyons, J. L. Sessler, C. W. Bielawski and A. J. Bard, *The Journal of Physical Chemistry Letters*, 2012, **3**, 2035-2038.

19. Y. L. Chang, R. E. Palacios, F.-R. F. Fan, A. J. Bard and P. F. Barbara, *Journal of the American Chemical Society*, 2008, **130**, 8906-8907.

20. C. RemziáBecer, *Journal of Materials Chemistry*, 2009, **19**, 3838-3840.

21. V. Filipe, A. Hawe and W. Jiskoot, *Pharmaceutical Research*, 2010, **27**, 796-810.

22. R. Compton, F. Davis and S. Grant, *Journal of Applied Electrochemistry*, 1986, **16**, 239-249.

Chapter 5

Doping of Single Polymeric Nanoparticles

Building on the study of polymeric organic nanoparticles discussed in the previous chapter, it is clearly important to be able to characterize *single* polymeric organic nanoparticles using electrochemical methods. In this chapter, the oxidative doping of single poly (N-vinylcarbazole) (PVK) nanoparticles is studied in aqueous sodium perchlorate using the nano-impacts method. In these experiments using suspensions of PVK nanoparticles, the Brownian motion the nanoparticles brings them, from time to time, in contact with a microelectrode held under potentiostatic control. Complete oxidative doping of single PVK nanoparticles with a size of approximately 120 nm is demonstrated, showing for the first time a simple strategy to characterize the doping of polymeric nanoparticles at the single nanoparticle level. This work was published in *Angewandte Chemie, International Edition*, 53, (2014), 12587-12589.

5.1 Introduction

Polymeric nanoparticles (NPs) are widely used in energy storage and other applications[1-6]. Charge-transfer reactions using these materials involve the uptake or release of ions from the nanoparticulate polymer matrix and are generally studied by using an ensemble of nanoparticles in the form of a film or a composite which is usually supported on an electrode surface[7, 8]. For optimal performance, it is usually desirable that the nanoparticles can become fully charged or discharged. However, the unambiguous study of such processes is challenging when using an ensemble because the charge transfer is strongly coupled to mass transport processes which typically can only be approximately quantified.

Hitherto, the newly developed nano-impacts method has been mostly applied to determine the size of nanoparticles[9-11] as described in Chapter 2. In these experiments, charge transfer leads to dissolution of the nanoparticles. For example, silver nanoparticles are oxidized to Ag^+ ions, or indigo particles are reduced to form water soluble leuco-indigo (see Chapter 3). Alternatively, mediated electron transfer can take place on the surface of impacted nanoparticles[12-17]. Herein, we show how the charging and doping of single polymeric nanoparticles can be studied for the first time using the nano-impacts method. The oxidative doping of poly(N-vinylcarbazole) (PVK) nanoparticles is studied in aqueous sodium perchlorate solution. It is shown that the nanoparticles with a diameter of approximately 120 nm are oxidatively doped almost quantitatively with the uptake of one perchlorate ion per carbazole monomer unit. PVK nanoparticles are important for electroluminescent devices[18-20] whilst the doping of PVK films is important in battery technology[21, 22].

5.2 Experimental Section

5.2.1 Chemicals and Materials

The Chemicals used in this work are same as those in Section 4.2.1. Sodium perchlorate monohydrate (ACS reagent, >98%) was purchased from Sigma-Aldrich and used as received. All solutions were made up using ultrapure water of resistivity 18.2 MΩ cm (Millipore) at 25°C and degassed thoroughly with N_2 (oxygen-free, BOC Gases plc) before use.

5.2.2 Synthesis of PVK Nanoparticles

The experimental method used to synthesis PVK nanoparticles is described in Section 4.2.2. Specifically, 0.0380 g PVK powder was dissolved in 20 mL tetrahydrofuran (THF, 99.9%, anhydrous) solution. Then 100 μL PVK/THF solution was injected into 25 mL de-ionized water under vigorously stirring by magnetic vortexing at 800 rpm for 5 minutes. The nanoparticle suspension was subjected to sonication for 30 minutes at a temperature of 25℃.

5.2.3 Characterization of PVK Nanoparticles

The PVK nanoparticles were characterised by dynamic light scattering (DLS, Malvern Instruments Ltd, UK). DLS measurements were performed as detailed in Section 3.2.3.

5.2.4 Cyclic Voltammetry of PVK Nanoparticles

The experimental set-up was outlined in Section 3.2.4. For drop-casting and voltammetric measurements experiment, a glassy carbon macroelectrode (3 mm diameter) was used as the working electrode, a saturated calomel electrode (SCE) as the reference electrode (Radiometer, Copenhagen) and a large platinum mesh as the counter electrode. Varying amounts of the PVK NPs suspension were drop-cast on the glassy carbon macroelectrode to modify the electrode, and left to dry under a N_2 atmosphere. Cyclic voltammetry (CV) was conducted at scan rate of 50 mV/s in 1.0 M $NaClO_4$. Before each voltammetric scan the glassy carbon macroelectrode was polished using three grades of diamond spray (3, 1 and 0.1 microns) before sonication in water and drying with nitrogen.

5.2.5 Nano-impacts of PVK Nanoparticles

Nano-impacts were introduced and performed as detailed in Section 2.4. For electrochemical sizing and chronoamperometry of PVK nanoparticles, the electrodes used were same as in Section 5.2.4 however a micro-carbon electrode (diameter = 11 μm) was employed as the working electrode. The micro-carbon electrode was calibrated by using the same method as in Section 3.2.5. Signal Counter was used detect impact spikes identification and determine the individual spike area and OriginPro8.5.1 was applied for electrochemical data analysis and nanoparticle sizing.

5.3 Results and discussion

In this section, PVK nanoparticles are studied by using electrochemical methods. Cyclic voltammetry was conducted to detect the numbers of electrons transferred and oxidative potential during PVK nanoparticles oxidation. Doping of single PVK nanoparticles was characterized using the nano-impacts method. DLS measurements were conducted to characterise the average size of the PVK nanoparticles in solution and further compared the electrochemical results.

5.3.1 DLS Characterisation of PVK Nanoparticles

Dynamic light scatting (DLS, Malvern Instruments Ltd, UK) technique was conducted to characterize the PVK nanoparticles. The average size of the prepared PVK nanoparticles was measured to be approximately 121 nm and the size distribution is shown in Figure 5.1.

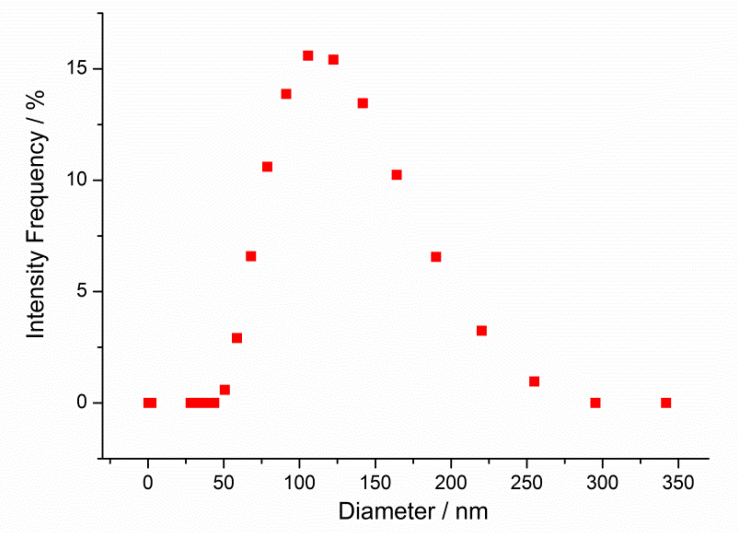


Figure 5.1 Size distribution of PVK nanoparticles by DLS measurement

5.3.2 Cyclic Voltammetry of PVK Nanoparticles

First, to find the approximate potentials required for nano-impacts experiments and the number of electrons transferred per PVK monomer in the oxidation of PVK NPs, cyclic voltammetry (CV) was used to study an ensemble of PVK nanoparticles by modifying a macro-sized glassy carbon (GC) electrode (diameter 3 mm) with different loadings of PVK nanoparticles.

Figure 5.2 shows the first and second scan of this PVK nanoparticles (10^{-10} mol carbazole moieties) modified electrode immersed in 1.0 M $NaClO_4$ solution at a scan rate of 50 mV/s. A single sharp oxidative was observed around +1.25 V. No peak was observed in backward scan or the second scan, indicating the oxidation of PVK nanoparticles is chemically irreversible and fully completed during the first scan in 1.0 M $NaClO_4$.

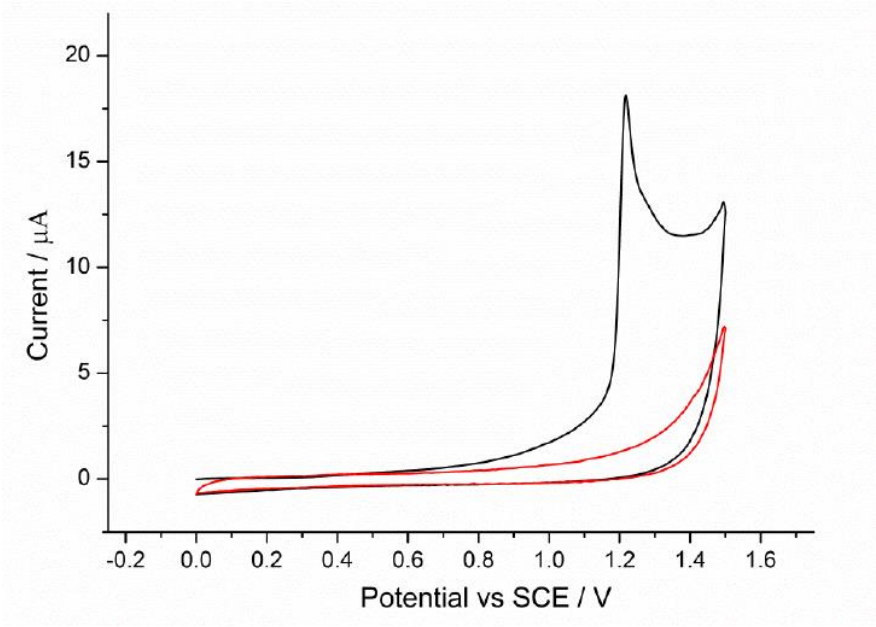


Figure 5.2 Cyclic voltammetric response of a glassy carbon macroelectrode modified with PVK nanoparticles (10^{-10} mol carbazole moieties) in 1.0 M $NaClO_4$ at a scan rate of 50 mV/s. (black: first scan; red: second scan).

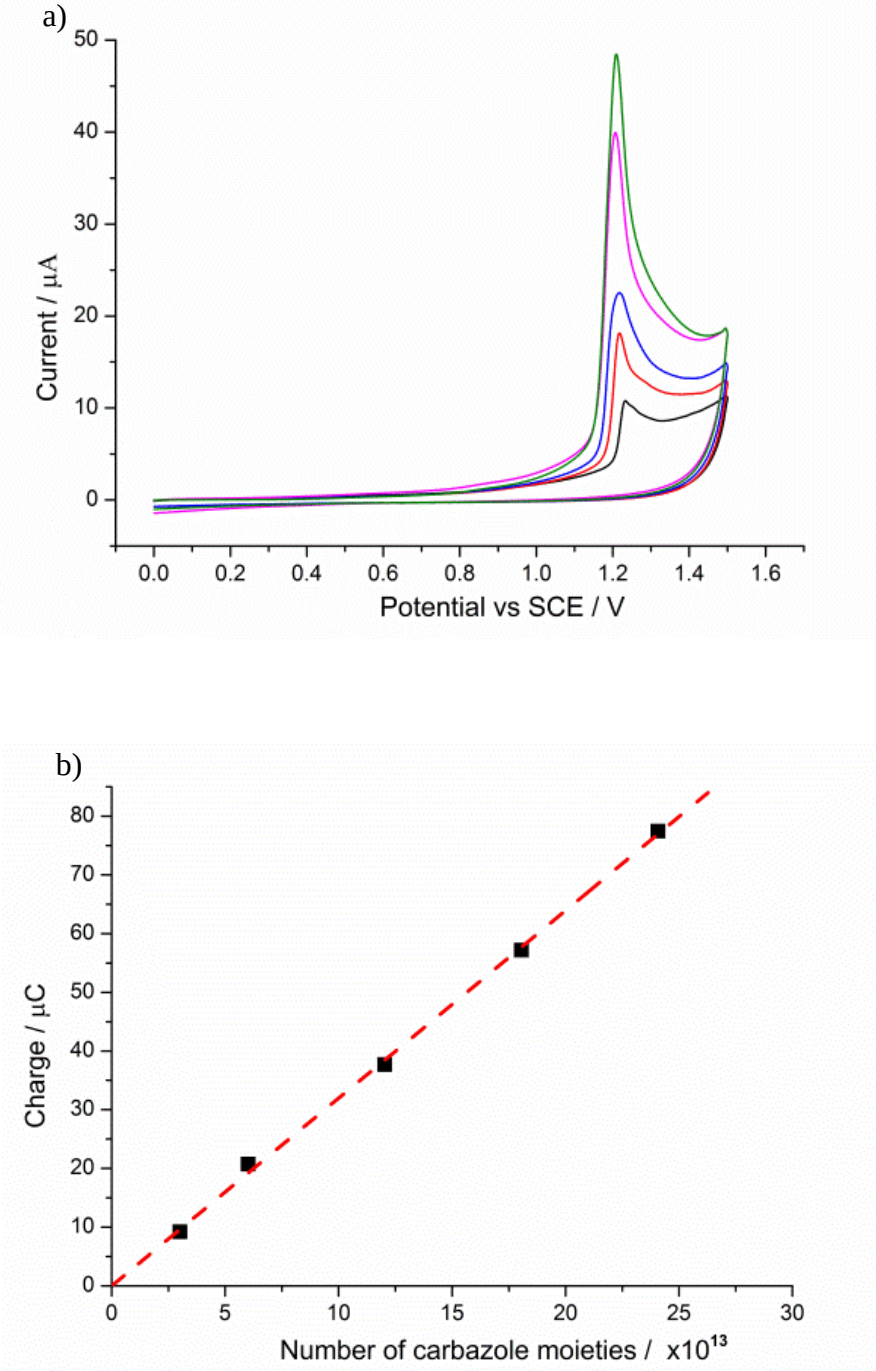


Figure 5.3 a) Cyclic voltammograms recorded for a glassy carbon macroelectrode modified with PVK nanoparticles of various amount (moles) of carbazole moieties: 5×10^{-11} mol (black), 1×10^{-10} mol (red), 2×10^{-10}mol (blue), 3×10^{-10} mol (magenta) and 4×10^{-10} mol (green) in 1.0 M $NaClO_4$ at a scan rate of 50 mV/s; b) Linear relation between the anodic peak charge (obtained from the integration of the peak area from Figure 5.3(a)) and the PVK nanoparticle loadings on the electrode surface.

Then, cyclic voltammetry was conducted for different loadings of PVK nanoparticles (from 5×10^{-11} mol up to 4×10^{-10} mol of carbazole moieties applied to the electrode) on the surface of the macro glassy carbon electrode, as shown in Figure 5.3(a). By integrating the area of each oxidative peak, the passed charge was plotted versus number of monomer carbazole units, giving an excellent linear relationship as shown in Figure 5.3(b). By calculating the gradient, it was confirmed that the number of electrons transferred per PVK monomer during the doping PVK nanoparticles was determined to be 2 ± 0.1 electrons. This suggests that the oxidative doping of PVK nanoparticles requires a two-electron-transfer process, which is consistent with the results shown in Chapter 4.

5.3.3 Doping of Single PVK Nanoparticles

Next, a clean, unmodified carbon microelectrode was placed in 1.0m $NaClO_4$ solution and a fixed concentration of dispersed PVK nanoparticles added. The oxidation potential used for subsequent impact experiments was +1.35 V versus SCE (saturated calomel electrode), a value chosen based on our initial results (see Chapter 4) to ensure that complete oxidation of PVK nanoparticles would occur. Under potentiostatted conditions, that is, at +1.35 V versus SCE, clear oxidative spikes from individual PVK nanoparticles were detected as shown in Figure 5.4. The onset of these Faradaic spikes was found to be dependent on potential and no spike was detected at lower oxidation potentials, such as +0.4 V and +0.6 V, showing that those spikes result from the oxidative doping of PVK nanoparticles. A control experiment was conducted at potential +1.35 V versus SCE with no PVK nanoparticles in the solution. No spikes were seen in this experiment, confirming that the individual spikes are a result of the random collisions of single PVK nanoparticles

with the surface of the electrode and subsequent oxidative doping and electron transfer from the electrode.

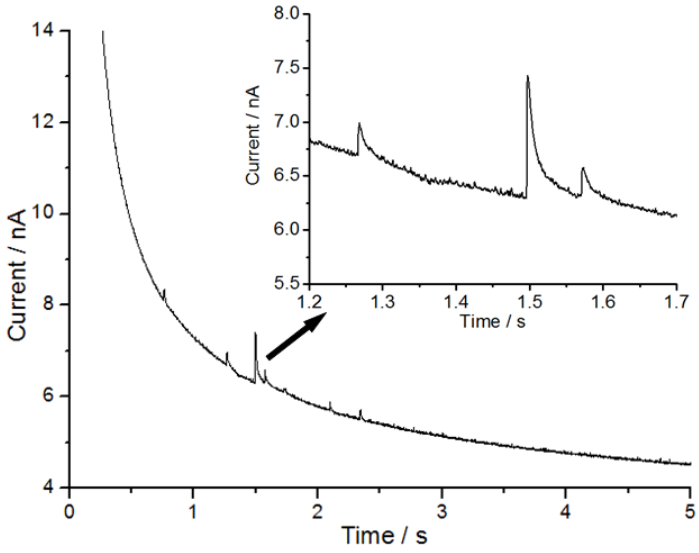


Figure 5.4 Typical chronoamperometric profiles showing oxidative Faradaic spikes of PVK NPs in 1.0m $NaClO_4$ at +1.35 V versus SCE. Inset: detailed impact spikes

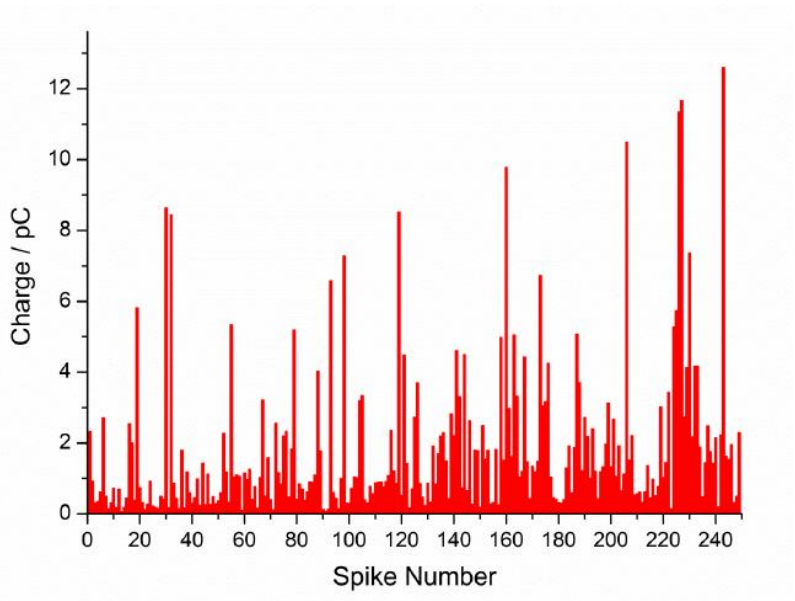


Figure 5.5 The charge resulting from the oxidative doping of single individual PVK nanoparticles of a total number of 249

A total of 249 spikes were detected from 131 chronoamperograms, each of 5 seconds duration, recorded at +1.35 V, corresponding to the oxidative doping of 249 individual PVK NPs. The charge of the electrons during doping of single nanoparticles was then calculated by integrating the area underneath the individual spikes (Figure 5.5). This is the first time oxidative doping of single polymeric nanoparticles has been detected or measured.

To characterize the yield of oxidative doping of single polymeric nanoparticles, the modal size D_{np} (size distribution) of the same batch of PVK NPs was estimated to be 121 nm through dynamic light scattering (DLS) experiments (Figure 5.1). If the charge is passed as a result of complete doping of single nanoparticles, then the theoretical charge (Q) of electron transfer from the complete doping of single polymeric nanoparticles, assuming that the PVK nanoparticles are spherical, can be determined by Equation 5.1:

$$Q = \frac{D_{np}^3 nF\pi\rho}{6M} \qquad \text{(Eqn 5.1)}$$

where D_{np} is the diameter of PVK nanoparticles, M is the molar mass of each PVK monomeric unit, ρ is the density of PVK, and F is the Faraday constant. The parameter n is the number of electrons transferred per PVK monomer during nanoparticle oxidation. The value of n (n=2) was obtained from Figure 5.3 (see above). Finally, comparing the modal charge Q_y (where Q_y =1.23×10^{-12} C) resulting from the oxidative doping of 249 single polymeric nanoparticles from the experimental nano-impacts method with the theoretical estimated maximum charge Q (Q =1.09×10^{-12} C) of single polymeric nanoparticles, indicates that there is effectively complete oxidative doping (110 ± 20%) of

single polymeric PVK NPs. The slightly larger estimated charge may be attributed to the aggregation/agglomeration of polymeric nanoparticles at a high concentration in sodium perchlorate solution during the course of the nano-impacts experiments.

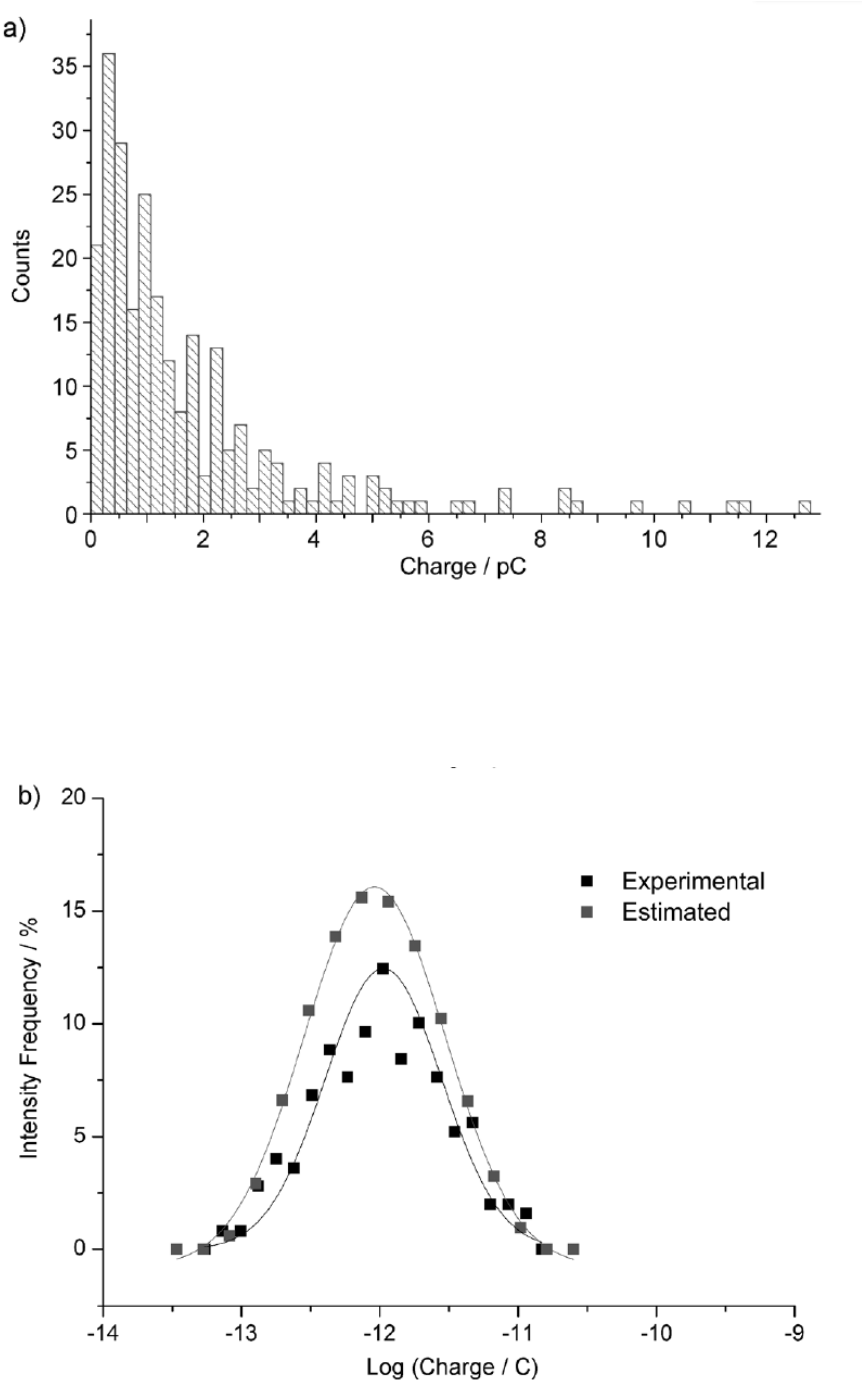


Figure 5.6 a) Distribution of charge from oxidative doping of single PVK NPs by analysis of the 249 oxidation spikes from nano-impacts experiments. b) Charge distribution of single PVK NPs derived from charge per spike from nano-impacts experiments (black) and the theoretical values (grey) estimated using Equation (1) from DLS data

In addition, there was good agreement between the distribution of charge from the oxidative doping by the nano-impacts method, as analysed from the above equation for all 249 single polymeric PVK nanoparticles, and the theoretical estimation (Figure 5.6). The similar normal distributions further indicate complete oxidative doping of individual polymeric PVK nanoparticles even if there is size distribution of the analysed individual nanoparticles. First, the results show the almost complete oxidative doping of single polymeric PVK nanoparticles and that a quantitative analysis of doping yield of single polymeric nanoparticles is viable using the nano-impacts method. Second, the results show that the PVK nanoparticles are quantitatively oxidized with the uptake of one perchlorate ion per carbazole monomer unit, as illustrated in Scheme 4.1 (chapter 4), based on the expected electro-oxidation of PVK[23-25].

5.4 Conclusions

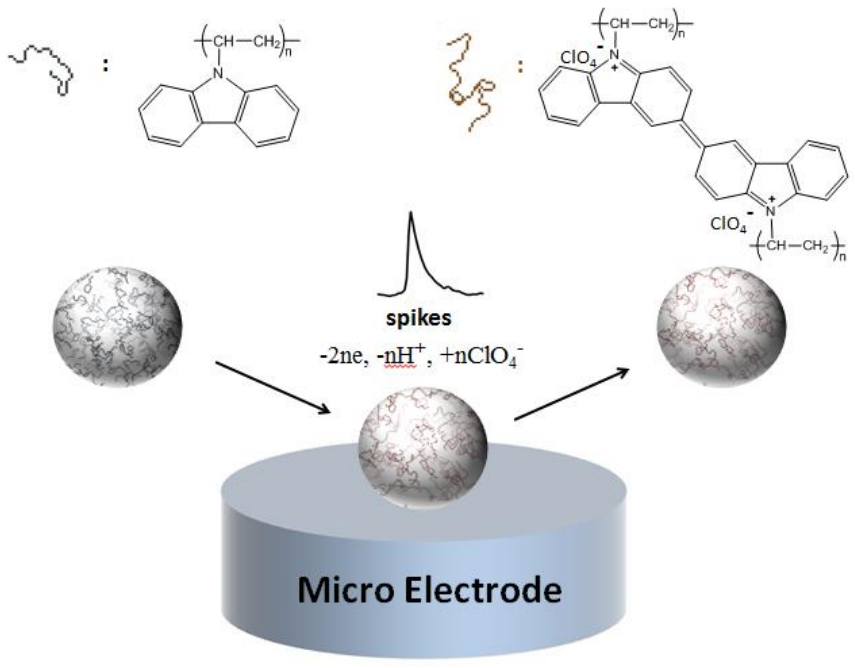


Figure 5.7 Schematic diagram showing the doping of single PVK nanoparticles

In this chapter, we have shown the real application of the nano-impacts method for doping single polymeric nanoparticles (Figure 5.7) and further demonstrated how to characterize the doping yield from doped single nanoparticles. We believe that this strategy will have major applications in the characterization of doped polymeric nanoparticles for new materials and energy applications. This method additionally provides unique characterization of polymeric single nanoparticles, such as dopant effect and doping yield, which are difficult to characterize by other spectroscopic or electron microscopy methods.

The electrochemistry of polymeric nanoparticles as a whole and of single polymeric nanoparticles was studied in Chapter 4 and Chapter 5. The next chapter introduces the detection and characterization of bifunctional organic nanoparticles which can be both electrochemically oxidized and reduced.

References

1. Q. Zhang, E. Uchaker, S. L. Candelaria and G. Cao, *Chemical Society Reviews*, 2013, **42**, 3127-3171.
2. A. R. Kirtane and J. Panyam, *Nature Nanotechnology*, 2013, **8**, 805-806.
3. K. Pu, A. J. Shuhendler, J. V. Jokerst, J. Mei, S. S. Gambhir, Z. Bao and J. Rao, *Nature Nanotechnology*, 2014, **9**, 233-239.
4. F. H. Schacher, P. A. Rupar and I. Manners, *Angewandte Chemie*, 2012, **124**, 8020-8044.
5. Y. L. Colson and M. W. Grinstaff, *Advanced Materials*, 2012, **24**, 3878-3886.
6. K. Jaskiewicz, A. Larsen, I. Lieberwirth, K. Koynov, W. Meier, G. Fytas, A. Kroeger and K. Landfester, *Angewandte Chemie International Edition*, 2012, **51**, 4613-4617.
7. A. G. MacDiarmid, *Angewandte Chemie International Edition*, 2001, **40**, 2581-2590.
8. C. Li, H. Bai and G. Shi, *Chemical Society Reviews*, 2009, **38**, 2397-2409.
9. Y. G. Zhou, N. V. Rees and R. G. Compton, *Angewandte Chemie International Edition*, 2011, **50**, 4219-4221.
10. Y. G. Zhou, N. V. Rees, J. Pillay, R. Tshikhudo, S. Vilakazi and R. G. Compton, *Chemical Communications*, 2011, **48**, 224-226.
11. K. Tschulik, B. Haddou, D. Omanović, N. V. Rees and R. G. Compton, *Nano Research*, 2013, **6**, 836-841.
12. S. E. F. Kleijn, S. C. S. Lai, T. S. Miller, A. I. Yanson, M. T. M. Koper and P. R. Unwin, *Journal of the American Chemical Society*, 2012, **134**, 18558-18561.
13. J. H. Park, S. N. Thorgaard, B. Zhang and A. J. Bard, *Journal of the American Chemical Society*, 2013, **135**, 5258-5261.

14. D. Wakerley, A. G. Guell, L. A. Hutton, T. S. Miller, A. J. Bard and J. V. Macpherson, *Chemical Communications*, 2013, **49**, 5657-5659.

15. R. Dasari, D. A. Robinson and K. J. Stevenson, *Journal of the American Chemical Society*, 2013, **135**, 570-573.

16. S. E. Fosdick, M. J. Anderson, E. G. Nettleton and R. M. Crooks, *Journal of the American Chemical Society*, 2013, **135**, 5994-5997.

17. J. M. Kahk, N. V. Rees, J. Pillay, R. Tshikhudo, S. Vilakazi and R. G. Compton, *Nano Today*, 2012, **7**, 174-179.

18. C. F. Huebner, J. B. Carroll, D. D. Evanoff, Y. Ying, B. J. Stevenson, J. R. Lawrence, J. M. Houchins, A. L. Foguth, J. Sperry and S. H. Foulger, *Journal of Materials Chemistry*, 2008, **18**, 4942-4948.

19. C. Martin, S. Bhattacharyya, A. Patra and A. Douhal, *Photochemical & Photobiological Sciences*, 2014, **13**, 1241-1252.

20. C. Jiang, W. Yang, J. Peng, S. Xiao and Y. Cao, *Advanced Materials*, 2004, **16**, 537-541.

21. F. C. Chen, Y. Yang, M. E. Thompson and J. Kido, *Applied Physics Letters*, 2002, **80**, 2308-2310.

22. J. Jang, Y. Nam and H. Yoon, *Advanced Materials*, 2005, **17**, 1382-1386.

23. R. G. Compton, F. J. Davis and S. C. Grant, *Journal of Applied Electrochemistry*, 1986, **16**, 239-249.

24. S. N. Bhadani, *Journal of Applied Polymer Science*, 1991, **42**, 1271-1273.

25. A. Desbene-Monvernay, J. E. Dubois and P. C. Lacaze, *Journal of Electroanalytical Chemistry and Interfacial Electrochemistry*, 1985, **189**, 51-63.

Chapter 6

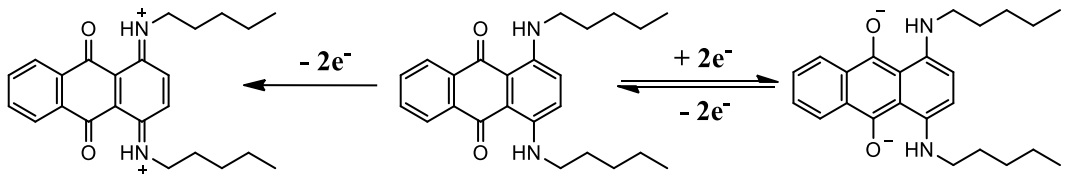
Electrochemistry and Nano-impacts of Bifunctional Organic Nanoparticles

This chapter investigates the electrochemical study of *bifunctional* organic nanoparticles by using Oil Blue Dye (OBD) as model nanoparticles which can be both electrochemically oxidized and reduced. The synthesis and characterization of OBD nanoparticles is studied along with their use for nano-impacts experiments in aqueous solution. The latter reveal current spikes corresponding to quantitative two electron reductions due to the reduction of the quinone groups and quantitative two electron oxidations from the 1, 4-phenylenediamine groups present in the OBD molecules within the nanoparticles. In both cases, the oxidation or reduction leads to size distributions in good agreement with independent measurements made using dynamic light scattering (DLS) showing that the redox events accompanying the nano-impacts lead to the full oxidation/reduction of the nanoparticles. This work presented herein was published in *Nanoscale*, 6, (2014), 6873-6878.

6.1 Introduction

So far, it has been shown that so-called 'nano-impacts' can be used for the identification and sizing of nanoparticles suspended in aqueous solution[1-7] and to study the doping of polymeric nanoparticles (see Chapter 5). These sizing works have previously focused to date on metallic nanoparticles[1-7] and organic samples in Chapter 3-5, where it has been shown that in addition to size distributions[1], concentrations[2] and information about the state of agglomeration[4] or aggregation[6] of the nanoparticles can be quantitatively measured. Experiments have also been done on the metal oxide Fe_3O_4 ($Fe(II)_2Fe(III)O_4$)[9] where both reductive and oxidative transients are seen. The former correspond to the reduction of Fe(III) to Fe(II) and the latter to the oxidation of Fe(II) to Fe(III). For both types of transient the quantitative dissolution of the Fe_3O_4 nanoparticles was inferred.

Hitherto study of nano-impacts experiments using monomeric organic nanoparticles are restricted to just one example, that of the reduction of indigo nanoparticles as described in Chapter 3[10]. In this chapter we present a second example namely that of organic monomeric nanoparticles of Oil Blue Dye (OBD). In addition to sizing these nanoparticles electrochemically using nano-impacts, we take advantage of their bifunctional character. In particular they have both quinone and phenylenediamine groups, such that the nanoparticles can undergo both oxidation and reduction in nano-impacts experiments as shown in Scheme 6.1.



Scheme 6.1 Likely mechanism of Oil Blue Dye reduction and oxidation

By comparison of the charge passed together with DLS analysis in both oxidation and reduction further strong evidence is deduced for the quantitative electroanalysis of organic nanoparticles during nano-impacts.

6.2 Experimental Section

6.2.1 Chemicals and Materials

Oil Blue N (dye content 96%), acetone (ACS reagent, ≥99.5%), acetonitrile (anhydrous, 99.8%), tetra-n-butylammoniumperchlorate (TBAP, electrochemical grade, 99%) were purchased from Aldrich and used as received. The phosphate buffer solution (pH = 6.8) was composed of 50 mM monobasic and dibasic potassium phosphates, 0.1 M KCl used as further supporting electrolyte. Unless stated otherwise, all chemicals in this work were acquired from Sigma–Aldrich. All solutions were made up using ultrapure water of resistivity 18.2 MΩ cm (Millipore) at 25℃ and degassed thoroughly with N_2 (oxygen-free, BOC Gases plc) before use.

6.2.2 Synthesis of OBD Nanoparticles

OBD (Oil Blue Dye) nanoparticles were synthesised by the reprecipitation method as performed in Chapter 2. OBD was dissolved in 20 mL acetone, giving an OBD concentration of 2.5 mM. Then 1 mL OBD/acetone solution was injected into deionized water and thoroughly mixed by magnetic vortexing stirring at 800 rpm. The resulting mixture was a dark blue, transparent dispersion. Then, it was subject to sonication for 20 minutes at a temperature of 25℃. The OBD nanoparticles suspension then resulted in a blue transparent solution.

6.2.3 Characterization of OBD Nanoparticles

Dynamic light scattering (DLS, Malvern Instruments Ltd, UK) was conducted to detect the synthesised OBD nanoparticles. Details are as in Section 3.2.3.

6.2.4 Cyclic Voltammetry of OBD in Organic Solvent

The experimental set-up was detailed in Section 3.2.4. For cyclic voltammetry of 1 mM OBD in acetonitrile with 0.1 M TBAP as supporting electrolyte, a glassy carbon (GC, diameter = 3.0 mm) electrode was used as the working electrode, a saturated calomel electrode (SCE) as the reference electrode (Radiometer, Copenhagen), and a platinum mesh as the counter electrode. The scan rates conducted for both the oxidation and the reduction experiments varied from 50mV/s to 500mV/s. Prior to modification the GC electrode was polished using 3.0, 1.0 and 0.1 μm diamond spray and then sonicated in H_2O for 1 min. All solutions were thoroughly degassed with nitrogen before scanning and an oxygen-free environment was maintained during measurements.

6.2.5 Cyclic Voltammetry of OBD Nanoparticles in Aqueous Solution

For the cyclic voltammetry of OBD nanoparticles in aqueous solution, the instrumentations and electrodes were used as same as in Section 6.2.4. The working electrode was modified with drop-casting techniques as shown in Section 2.2.1. The working electrode was modified with a known amount of OBD nanoparticles suspension (2×10^{-4} mol/L, monomer concentration) using the drop-casting technique shown in Section

2.2.1 and dried under nitrogen between each modification. Cyclic voltammetry was then conducted at a scan rate of 50 mV/s for both OBD nanoparticles reactions.

6.2.6 Nano-impacts of OBD Nanoparticles

"Nano-impacts" were previously introduced in Section 2.4. The same reference and counter electrodes were used as in Section 6.2.4 but the working electrode was a carbon microelectrode (diameter = 11 μm), which was calibrated by the same method in Section 3.2.5. For each scan, chronoamperogram was measured in PBS buffer (pH = 6.8) with a duration of 5s and a sample time of 0.5ms. GPES was used to conduct the chronoamperometry and to collect the data, Signal counter was employed for performing the information of impact spikes and Origin Pro 8.5.1 was applied for electrochemical data analysis.

6.3 Results and Discussion

In this section, the electrochemistry of OBD nanoparticles is investigated in both organic solution and in aqueous solution. Cyclic voltammetry was conducted for the electrochemical characterization of OBD in acetonitrile to detect the number of electrons transferred of during both oxidation and reduction of OBD. The oxidative and reductive potential of OBD nanoparticles in PBS (pH = 6.8) was studied by drop-casting and stripping experiments. Furthermore, the electrochemical sizing of individual OBD nanoparticles was carried out using both direct oxidative and reductive nano-impacts experiments showing excellent agreements with DLS analysis.

6.3.1 Electrochemical Characterization of Molecular OBD Dissolved in Acetonitrile

A bare glassy carbon electrode was immersed in 1.0 mM OBD in acetonitrile solution with 0.10 M TBAP as supporting electrolyte. The solution was degassed to remove electroactive dissolved oxygen. Cyclic voltammetry was recorded at different scan rates from 50 mV/s to 500 mV/s as shown in Figure 6.1. The cyclic voltammetry shows two separate cathodic peaks, likely responding to formation of mono and dianions (Scheme 6.2) respectively through two single-electron transfer processes. This is a similar observation to that seen for the reduction of molecular anthraquinone[12-14]. At slow scan rates, peak separations of the first pair of redox peaks are ca. 60 mV, indicating an electrochemically reversible process for the first electron transfer of OBD.

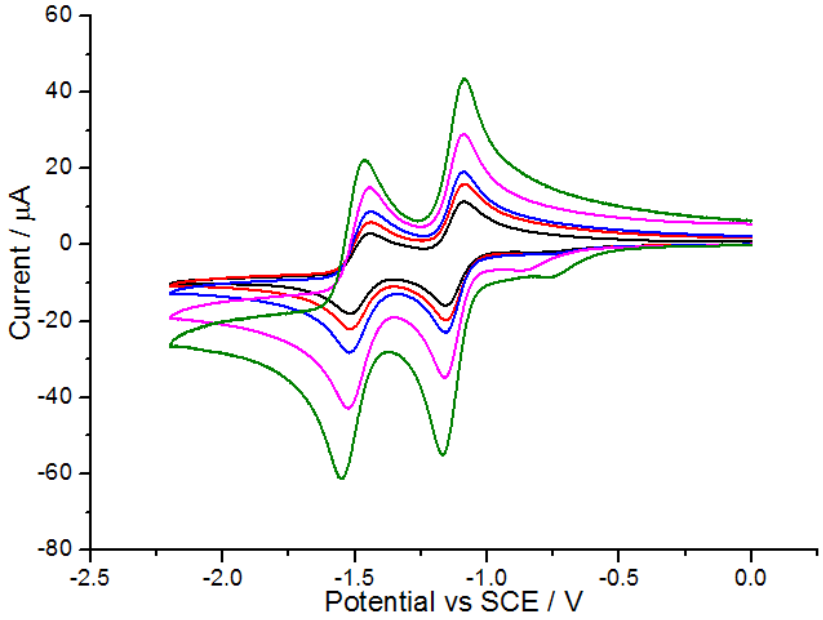
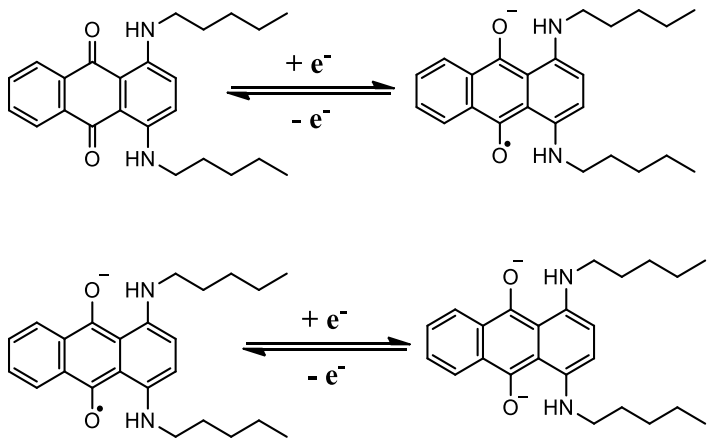


Figure 6.1 The cyclic voltammetric reductive response of 1.0 mM OBD in acetonitrile with 0.10 M TBAP as supporting electrolyte at scan rates of 50 mV/s (black), 75 mV/s (red), 100 mV/s (blue), 200 mV/s (magenta) and 500 mV/s (green)



E^0 ~ -1.15 V

E^0 ~ -1.55 V

Scheme 6.2 Likely mechanism of OBD reduction

To analyse the data in Figure 6.1 to give the diffusion coefficient of OBD in acetonitrile, we assumed that the first electron reduction of OBD is fully reversible and plotted the peak current versus square root of scan rate as shown in Figure 6.2 (measured for the -1.15V peak).

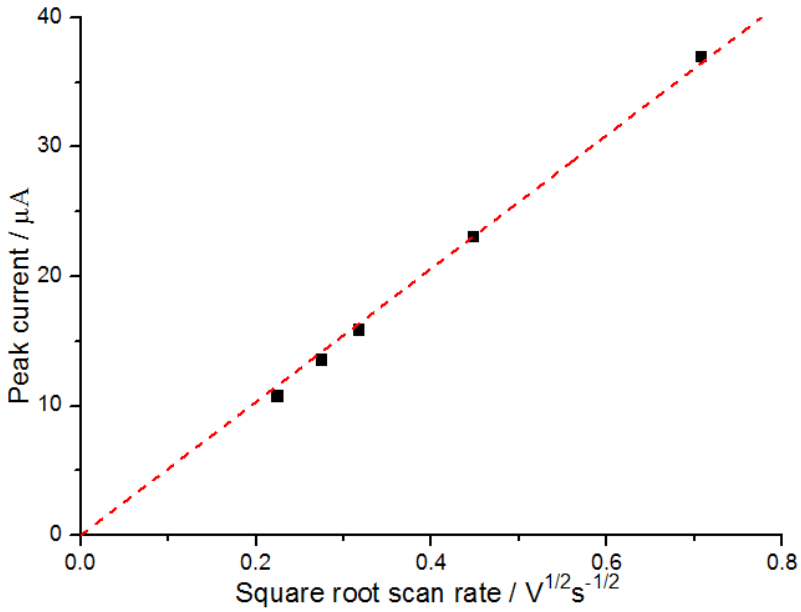


Figure 6.2 First reduction peak current verses square root of scan rate from 50 mV/s to 500 mV/s

By using the Randles-Sevcik equation as discussed in Chapter 1, the diffusion coefficient D of OBD was found to be 7.3×10^{-6} cm^2s^{-1}.

$$I_P = 2.69 \times 10^5 A D^{1/2} C_{OBD} v^{1/2} \quad \text{(Eqn 6.1)}$$

where I_P is the peak current, A is the surface area of the glassy carbon macroelectrode, C_{OBD} is the concentration of OBD in acetonitrile and v is the scan rate.

Next, the oxidative cyclic voltammetry of OBD was investigated (Figure 6.3). In order to explore the mechanism of OBD oxidation reaction, the vertex potentials for cyclic voltammetry were set as +1.4 V or +0.95 V.

Cyclic voltammetry with sweep reversal at +0.95 V at different scan rates from 50 mV/s up to 500 mV/s is shown in Figure 6.3(a). The peak separation between forward and backward peaks is around 62 mV, showing a likely electrochemically reversible oxidation of OBD to OBD monovalent cations corresponding to a single electron transfer process. Next, the cyclic voltammetry with +1.40 V as the vertex potential shows a pair of separate redox peaks as shown in Figure 6.3(b). The positions of the forward and backward peaks for the second oxidation shift with scan rates, indicating that the oxidation of OBD monovalent cations to OBD bivalent cations. However, the position of the backward peak does not show a reversible type of redox shape, indicating that there might be other products generated during the reduction of OBD bivalent cations. The likely mechanism is shown in Scheme 6.3 and is that expected for phenylenediamines [15].

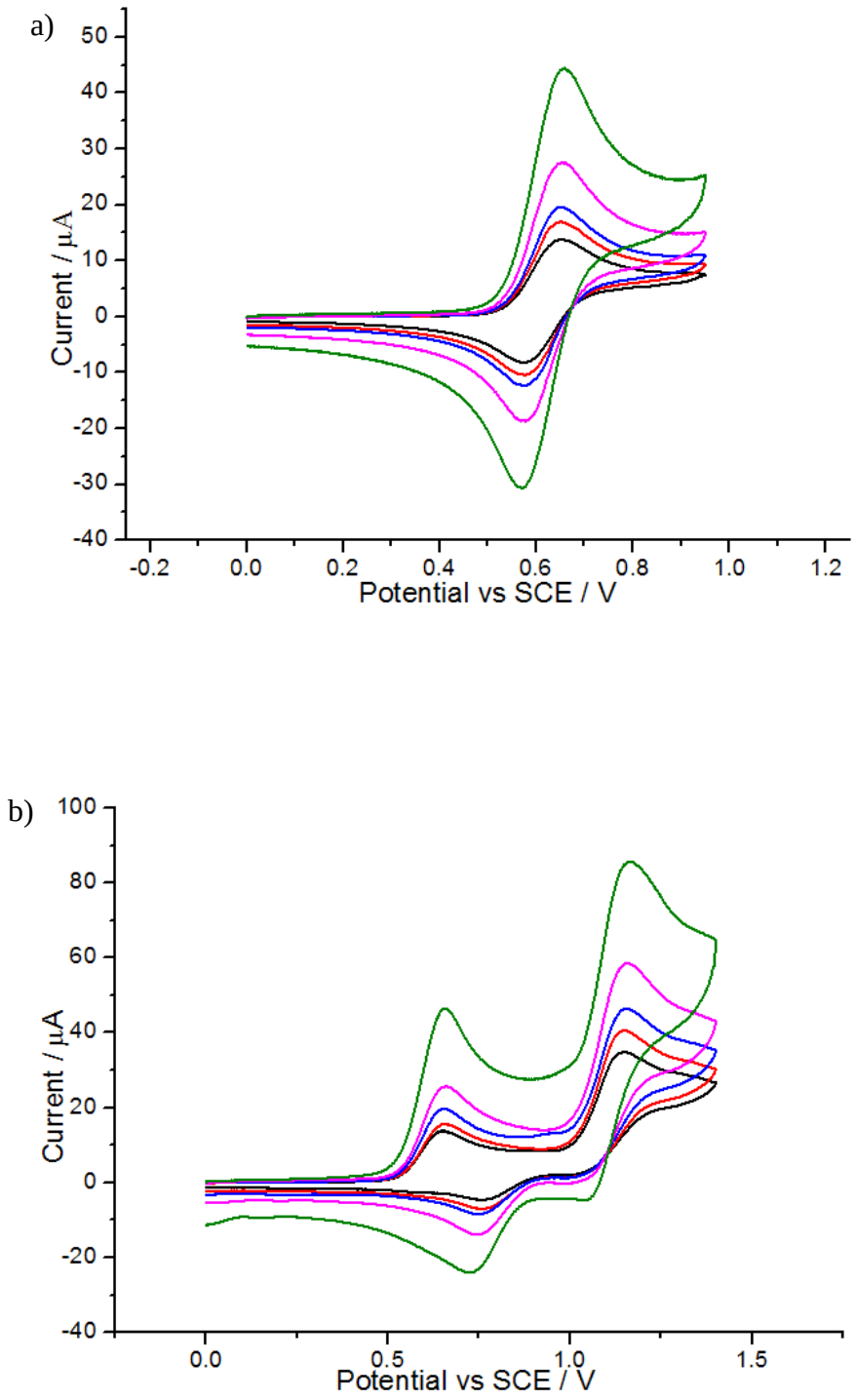
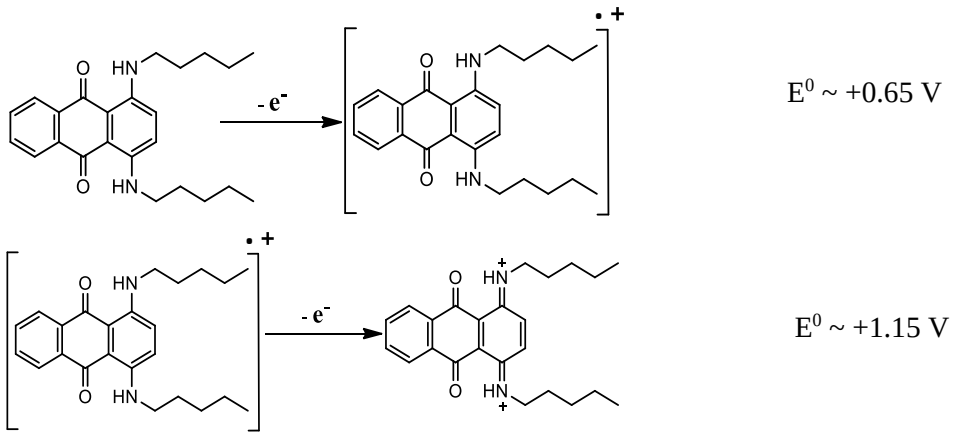


Figure 6.3 The cyclic voltammetric oxidative response of 1.0 mM OBD oxidation in acetonitrile with 0.10 M TBAP as supporting electrolyte at scan rate 50 mV/s (black), 75 mV/s (red), 100 mV/s (blue), 200 mV/s (magenta) and 500 mV/s (green) with vertex potential of cyclic voltammetry set as a) +0.95Vand b) +1.40 V



Scheme 6.3 Likely mechanism of OBD oxidation

6.3.2 Electrochemical Characterization of OBD Nanoparticles in Aqueous Solution

To estimate the reduction and oxidation potentials of OBD NPs for subsequent nano-impact experiments, a glassy carbon macroelectrode was modified by dropping a known amount of a OBD NPs suspension (2×10^{-4} mol/L) onto the surface and letting the electrode dry under nitrogen. Cyclic voltammetry was then recorded with the modified electrode immersed in PBS buffer. A significant reduction peak was observed at -0.75 V,which can be attributed to the reduction of the quinone group via a two electron transfer process [12, 16-18], and an oxidation peak at +0.95 V indicating the oxidation of OBD NPs electrochemical response as shown in Figure 6.4. This peak is similar in size to the reduction peak observed.

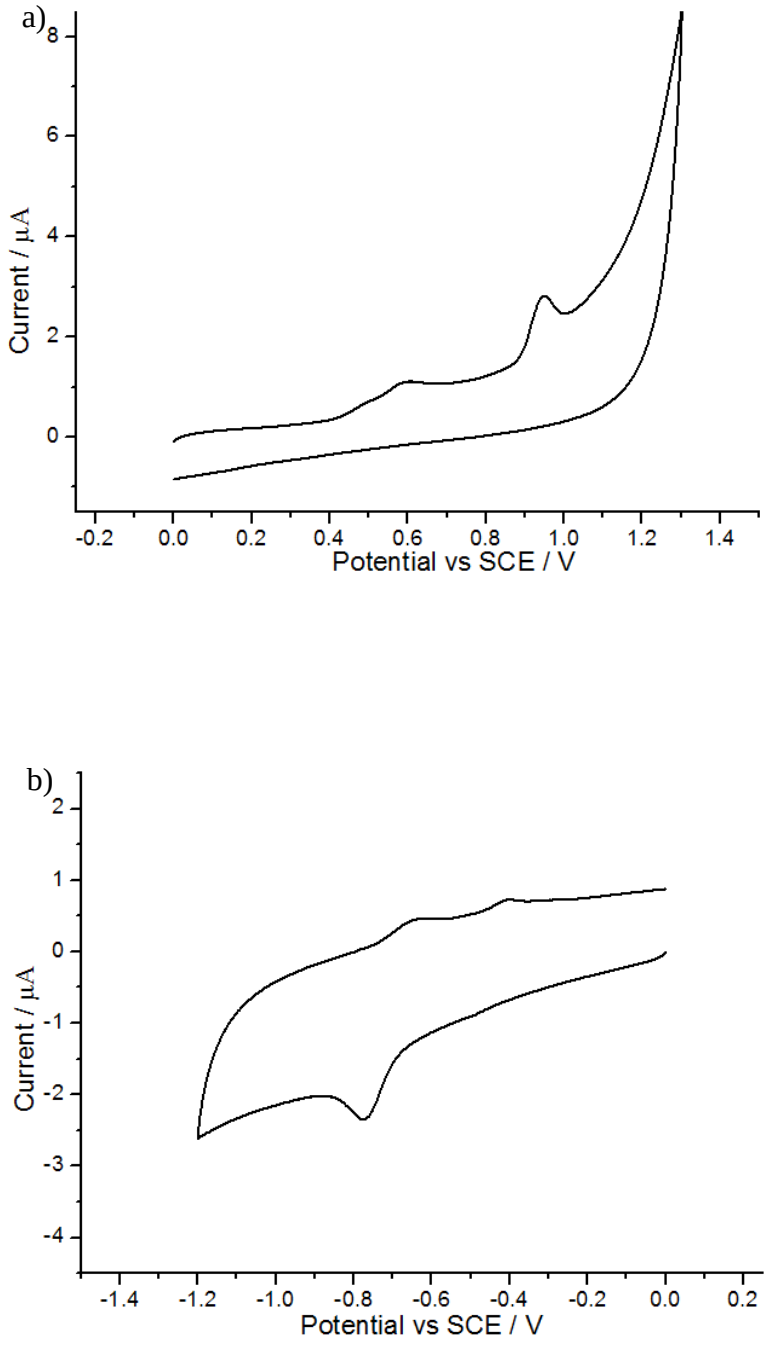


Figure 6.4 Cyclic voltammetric response of an OBD NPs modified GC electrode in a 0.1 M PBS buffer (pH = 6.8) at a scan rate of 50 mV/s a) oxidation and b) reduction

A smaller oxidation peak at +0.60 V was also observed, which likely corresponds to the partial one electron oxidation of OBD nanoparticles on the outer surface of the electrode[19], indicating that the oxidation may be size dependent[20]. To ensure complete oxidation of the OBD nanoparticles thus allowing their accurate sizing, the potential used for oxidation of OBD NPs in nano-impact experiments reported below was set at +1.0 V.

6.3.3 Nano-impacts of OBD Nanoparticles

A carbon microelectrode was placed in 0.1 M PBS buffer solution (pH = 6.8) and a known concentration of pre-dispersed OBD NPs added. Under potentiostatted conditions at -0.80 V *vs.* SCE, reductive (Faradaic) spikes from individual OBD NPs were observed (Figure 6.5(a)), showing that direct reduction of individual OBD nanoparticles during random collision events can be observed and quantified. In these studies, 52 chronoamperograms of 5s duration were recorded at a potential of –0.80 V, yielding 253 spikes for OBD NPs reduction reaction and the potential of +1.0 V was applied over 5s for 58 times, yielding 98 spikes in total for OBD NPs oxidation reaction.

Reductive spikes of OBD NPs at -0.80 V are shown in Figure 6.5(a), showing the reduction of individual OBD NPs during random collisions with the surface of the carbon microelectrode. The onset of these Faradaic spikes was found to be dependent on the reduction potential. Only a very few spikes were observed by reducing reduction potential such as -0.30 V, which may correspond to some OBD NPs undergoing uncomplete reduction. Further it confirms that the spikes at -0.80 V result from the complete Faradaic reduction of OBD NPs. The charge passed during reduction of individual OBD NPs was plotted by integrating the individual spikes as shown in Figure 6.5(b). Then, we quantified

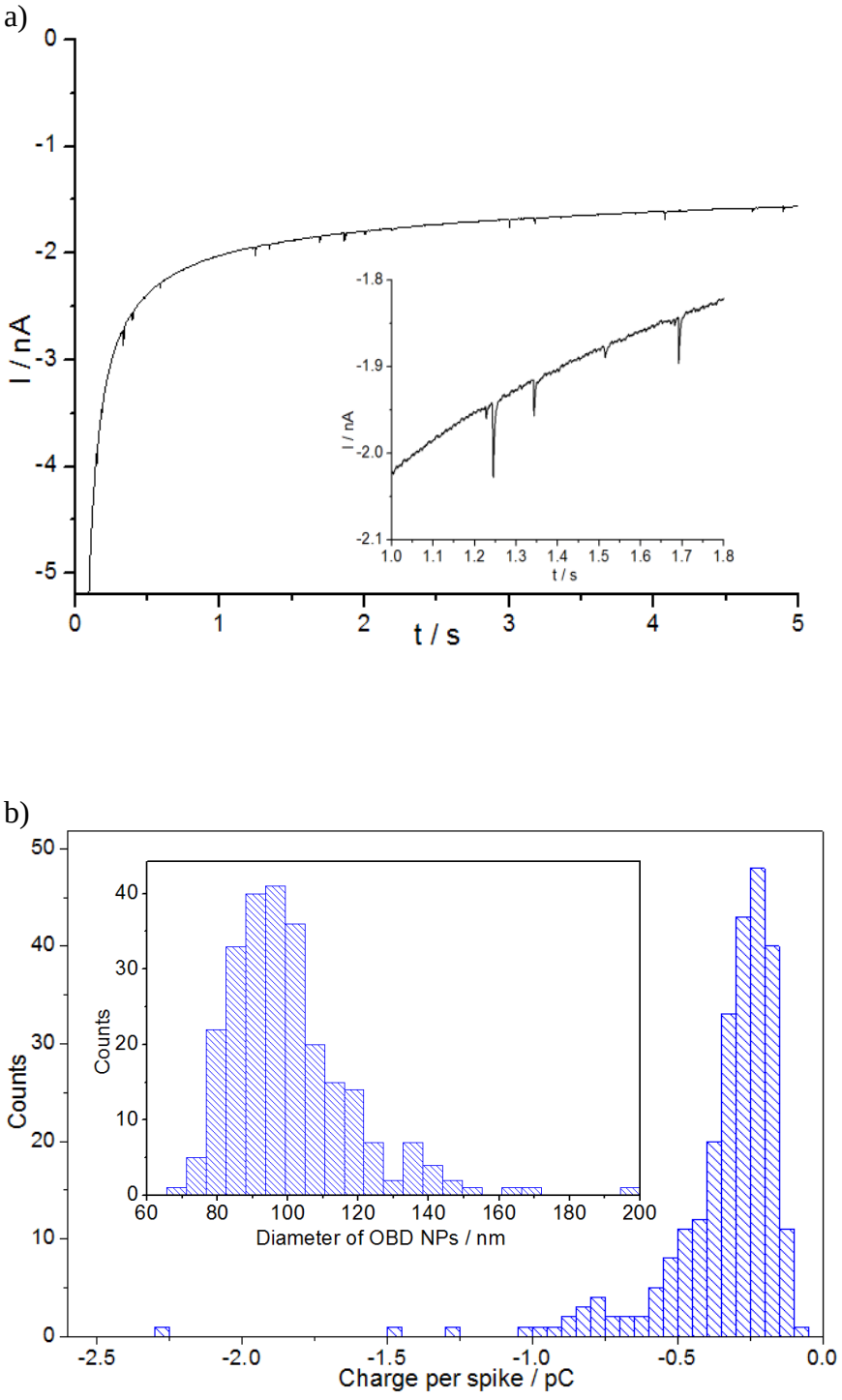


Figure 6.5 a) Chronoamperometric profiles showing reductive Faradaic spikes of OBD NPs in PBS buffer (pH = 6.8) at -0.80 V vs SCE. The inset showing the detailed impact spikes. b) Histogram showing the OBD NPs reductive charge and the inset showing size distribution.

the size of OBD NPs by using the equation between diameter and charge of single OBD NPs. As discussed in Section 2.4, assuming OBD NPs are spherical, the charge Q passed as a result of complete reduction of single OBD NPs is given by Equation 6.2:

$$D_{np} = 2 \times \sqrt[3]{\frac{3MQ}{4nF\pi\rho}} \qquad \text{(Eqn 6.2)}$$

where D_{np} is the diameter of OBD NPs, M is the molar mass of OBD, ρ is the density of OBD and F is the Faraday constant. The parameter n is the number of electrons transferred of OBD NPs reduction (n = 2) as discussed above. The size distribution derived by analysis of the 253 reduction spikes is shown in Figure 6.5(b) (inset), giving the mean diameter and standard deviation of OBD NPs as 100 ± 18 nm.

Similarly, under potentiostatted conditions at +1.00 V *vs.* SCE, oxidative (Faradaic) spikes from individual OBD NPs were also observed (Figure 6.6(a)), showing for the first time that direct oxidation of individual monomeric organic nanoparticles is feasible. The size distribution of OBD NPs can also be determined by analysing the Faradaic charge from the oxidative spikes of individual OBD NPs, as discussed above. The 98 impact spikes observed in anodic chronoamperograms were analysed using the same equation as above. The size distribution shows the mean diameter and standard deviation as 102 ± 26 nm (Figure 6.6(b)), which has an excellent agreement with the sizing from the reductive nano-impacts.

The oxidation spikes (Figure 6.6(a)) show a similar shape to the reduction spikes (Figure 6.5(a)). However, under the same concentration of OBD NPs, the frequency of reductive

spikes is higher than that of the oxidative spikes, which may be due to the electrode surface being blocked by oxidative products adsorptively, physically or covalently[21], while in contrast there is comparatively clean reductive dissolution of the OBD nanoparticles.

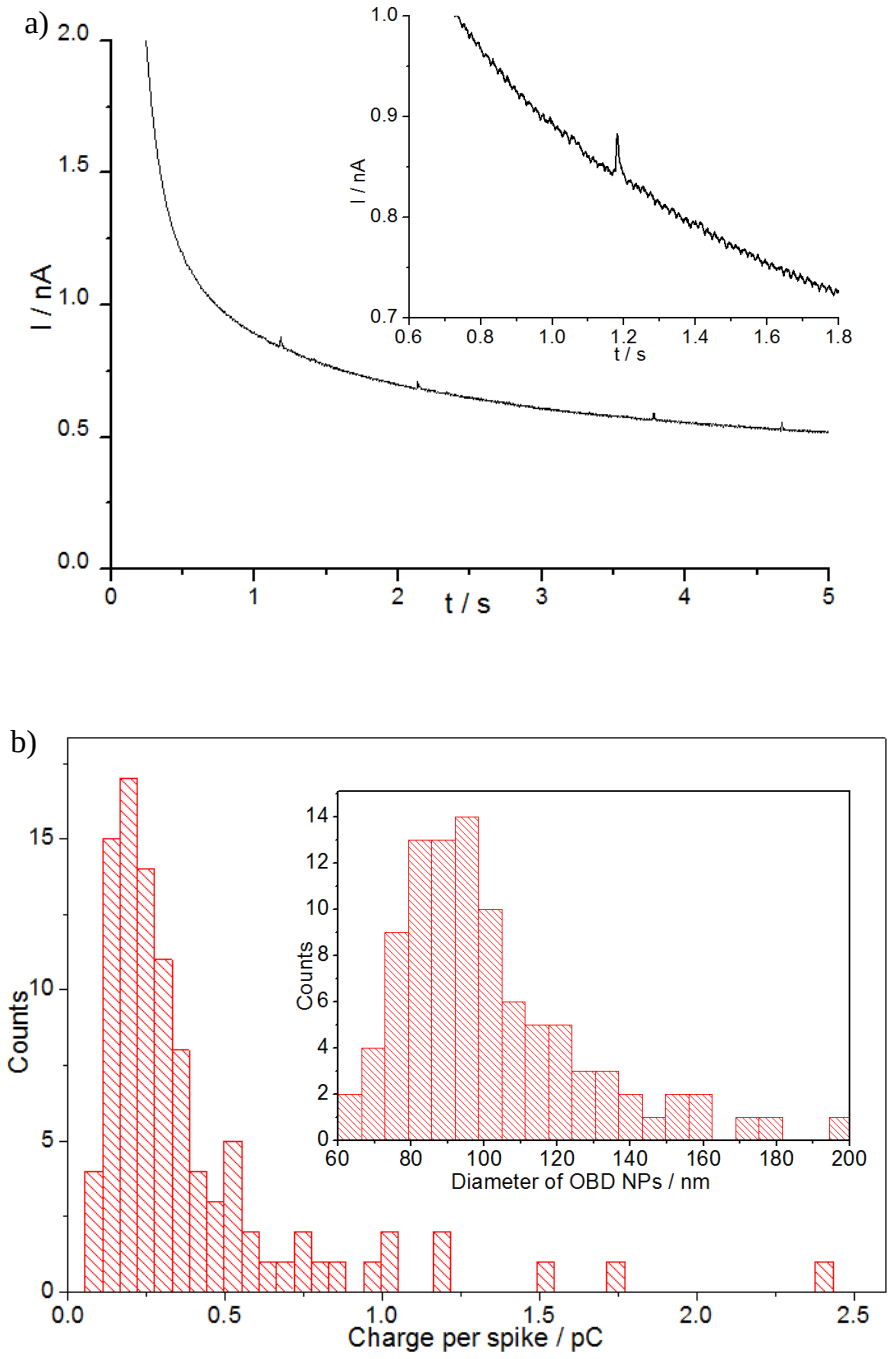


Figure 6.6 a) Chronoamperometric profiles showing oxdative Faradaic spikes of OBD NPs in PBS buffer (pH = 6.8) at +1.00 V vs SCE. The inset showing the detailed impact spikes. b) Histogram showing the OBD NPs oxidative charge and the inset showing size distribution.

6.3.4 Electrochemical Sizing and DLS Sizing of OBD Nanoparticles

To further verify our results from electrochemical sizing through the reduction and oxidation, we used dynamic light scattering (DLS) to characterize the same batch of OBD NPs. Both reduction and oxidation of OBD NPs yield the same size distributions which have an excellent agreement with the results obtained by DLS analysis, as shown in Figure 6.7. Thus we show for the first time that the size of bifunctional organic nanoparticles can be quantitatively determined by both direct oxidation and reduction by the nano-impacts method.

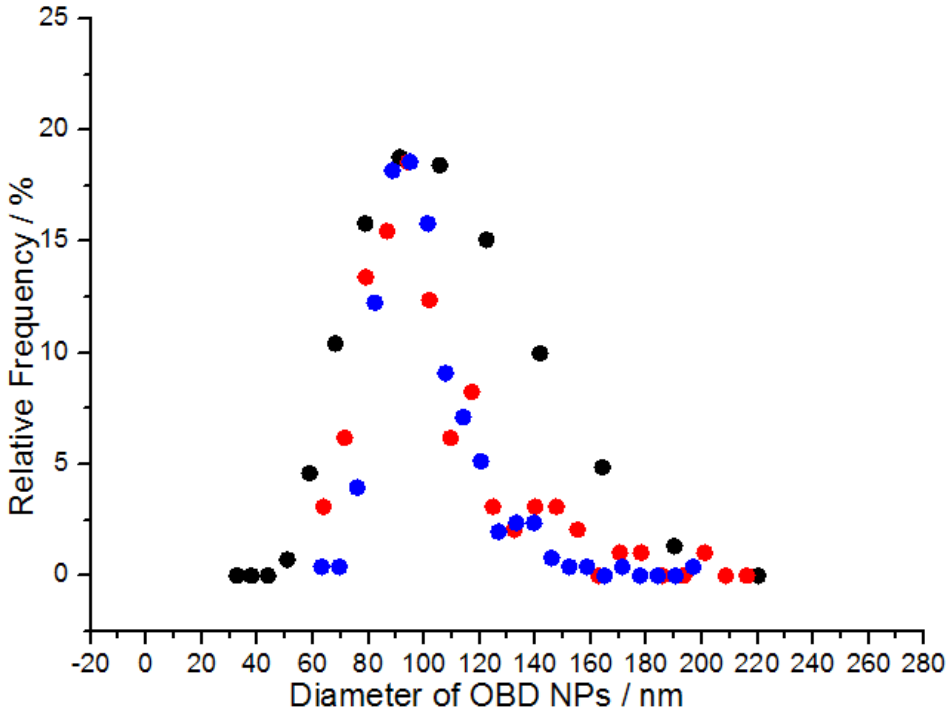


Figure 6.7 Size distribution of OBD NPs obtained from electrochemical sizing of nano-impacts experiments (blue dots: reduction; red dots: oxidation) and DLS analysis (black dots).

6.4 Conclusions

In this chapter, we introduce using electrochemical methods to quantify the size of bifunctional organic nanoparticles for the first time by both direct reduction and oxidation routes of individual bifunctional organic nanoparticles. Figure 6.8 shows schematically the reactions of the OBD nanoparticles during the nano-impact experiments. The agreement between the sizing distributions carried out via oxidation and reduction provides further evidence for the quantitative electroanalysis of nanoparticles during nano-impacts.

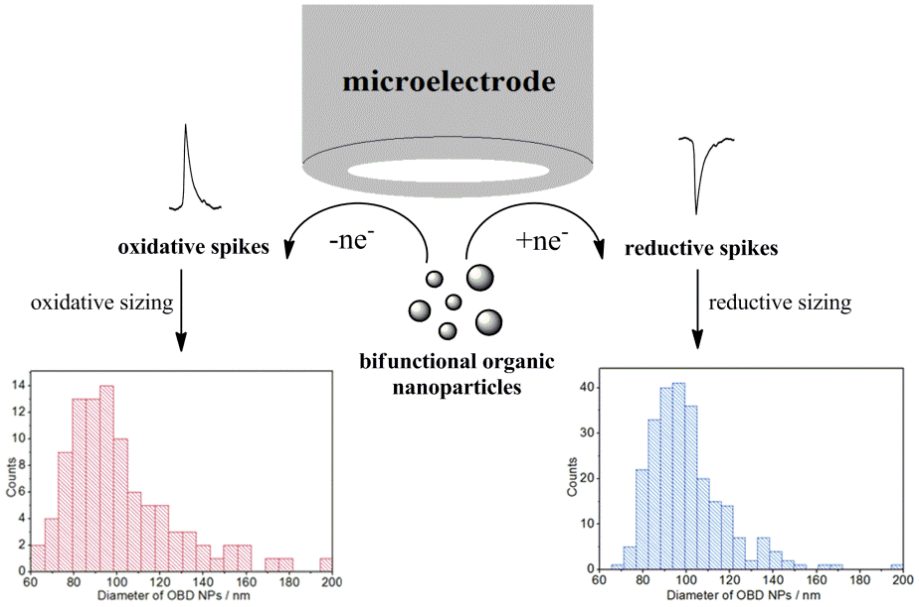


Figure 6.8 Schematic diagrams showing the oxidation and reduction of OBD nanoparticles during nano-impact experiments

By far, nano-impacts method have been successfully used to characterize the size of monomeric organic nanoparticles, polymeric nanoparticles and bifunctional organic

nanoparticles by completed electrochemical oxidation or reduction of individual nanoparticles. In the next chapter, another bifunctional organic nanoparticles sample, 2, 2-Diphenyl-1-picrylhydrazyl (DPPH), is studied by using nano-impacts experiments, giving more information of electrochemical sizing by complete oxidation of nanoparticles and a new core-shell structure by partial reduction of the nanoparticles.

References

1. Y. G. Zhou, N. V. Rees and R. G. Compton, *Angewandte Chemie International Edition*, 2011, **50**, 4219-4221.
2. E. J. E. Stuart, Y. G. Zhou, N. V. Rees and R. G. Compton, *RSC Advances*, 2012, **2**, 6879-6884.
3. Y. G. Zhou, N. V. Rees, J. Pillay, R. Tshikhudo, S. Vilakazi and R. G. Compton, *Chemical Communications*, 2012, **48**, 224-226.
4. J. Ellison, K. Tschulik, E. J. E. Stuart, K. Jurkschat, D. Omanovic, M. Uhlemann, A. Crossley and R. G. Compton, *ChemstryOpen*, 2013, **2**, 69-75.
5. B. Haddou, N. V. Rees and R. G. Compton, *Physical Chemistry Chemical Physics*, 2012, **14**, 13612-13617.
6. E. J. E. Stuart, N. V. Rees, J. T. Cullen and R. G. Compton, *Nanoscale*, 2013, **5**, 174-177.
7. E. J. E. Stuart, K. Tschulik, D. Omanovic, J. T. Cullen, K. Jurkschat, A. Crossley and R. G. Compton, *Nanotechnology*, 2013, **24**.
8. N. V. Rees, Y. G. Zhou and R. G. Compton, *RSC Advances*, 2012, **2**, 379-384.
9. K. Tschulik, B. Haddou, D. Omanovic, N. V. Rees and R. G. Compton, *Nano Research*, 2013, **6**, 836-841.
10. W. Cheng, C. Batchelor-McAuley and R. G. Compton, *ChemElectroChem*, 2014, **1**, 714-717.
11. E. I. Rogers, D. S. Silvester, D. L. Poole, L. Aldous, C. Hardacre and R. G. Compton, *The Journal of Physical Chemistry C*, 2008, **112**, 2729-2735.
12. C. Batchelor-McAuley, B. R. Kozub, D. Menshykau and R. G. Compton, *The Journal of Physical Chemistry C*, 2011, **115**, 714-718.

13. J. Katsumi, T. Nakayama, Y. Esaka and B. Uno, *Analytical Sciences*, 2012, **28**, 257-265.

14. I. Piljac and R. W. Murray, *Journal of The Electrochemical Society*, 1971, **118**, 1758-1764.

15. X. B. Ji and R. G. Compton, *Analytical Sciences*, 2007, **23**, 1317-1320.

16. M. A. G. Trindade and M. V. B. Zanoni, *Sensors and Actuators B: Chemical*, 2009, **138**, 257-263.

17. B. Zinger, *Journal of Electroanalytical Chemistry*, 1988, **239**, 209-225.

18. M. A. G. Trindade and M. V. B. Zanoni, *Electroanalysis*, 2007, **19**, 1901-1907.

19. A. Adenier, M. M. Chehimi, I. Gallardo, J. Pinson and N. Vila, *Langmuir*, 2004, **20**, 8243-8253.

20. O. S. Ivanova and F. P. Zamborini, *Journal of the American Chemical Society*, 2010, **132**, 70.

21. E. O. Barnes and R. G. Compton, *Journal of Electroanalytical Chemistry*, 2013, **693**, 73-78.

Chapter 7

Contrasts between Single Nanoparticle and Ensemble Electron Transfer: The Oxidation and Reduction of DPPH Nanoparticles in Aqueous Media

In the previous chapter, an electrochemical study of bifunctional organic nanoparticles (OBD NPs) was reported. This chapter focuses on another bifunctional organic nanoparticle, 2, 2-Diphenyl-1-picrylhydrazyl (DPPH), and makes contrasts between single organic nanoparticle and ensemble electron transfer in aqueous media. The oxidative and reductive electrochemistry of DPPH nanoparticles is studied via the nano-impacts method and drop-casted layers used to modify an electrode surface. In the former case the currents associated with single NP impacts are used to measure the electron transfer kinetics, whereas in contrast it is shown that the reduced diffusion caused by the overlap of adjacent diffusion layers in the latter case leads to more electrochemically reversible behaviour. This work presented herein was published in *ChemElectroChem* 2, (2015), 691-699.

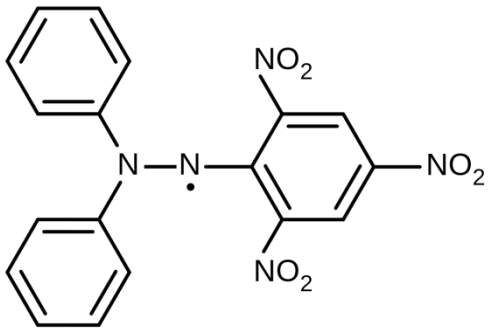
7.1 Introduction

The fundamental understanding of the electrochemical interface between electrodes and nanoparticles and the associated reactions and kinetics at the nanoscale is of significant importance to many important applications, such as alternative systems for clean energy production, storage and conversion[1-3].

Most previous studies to understand the electrochemistry of nanoparticles rely on the use of ensembles of nanoparticles[4], where only averaged properties can be obtained. However, the electrochemical behaviour of nanoparticle ensembles may be significantly different to the individual nanoparticles because of a combination of several complicated effects, such as the interparticle spacing[5], the surface coverage of the ensembles of nanoparticles[6, 7], and the agglomeration and aggregation[8-10] of the individual particles. Those combined effects make true effects or catalytic behaviour of nanoparticles[11, 12] unlikely be fully explored with the possibility for qualitatively changed reactivity for single nanoparticles at the nanoscale hard to prove. In addition, structural heterogeneity[13] prevalent at the individual particle level, particularly important for catalysis activity, is often masked in conventional ensemble-averaged activity measurements.

Directly probing the electrochemistry of single nanoparticles is challenging. Recent studies include the use of electrochemical scanning microscopy to scan a nanoelectrode over spatially separated nanoparticles supported on an electrode surface[14] or immobilizing a single nanoparticle at the surface of a nanoelectrode[15]. In this thesis, we show that the "nano-impacts" method can not only detect and count individual nanoparticles and but also measure the mediated electron transfer by such impacting single nanoparticles[16-20]. As

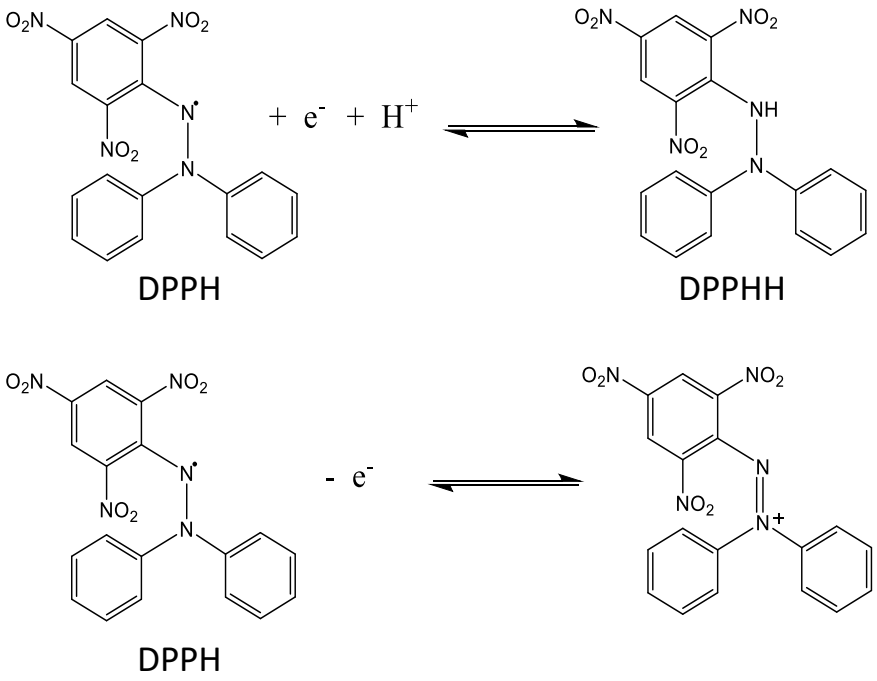
of now, this method has enabled sizing of impacting metal[21-23] and organic nanoparticles[24] (see also Chapter 3 and Chapter 6), the quantification of the doping level of polymeric nanoparticles (see Chapter 5), and can quantitatively analyse the drug load of single liposomes[25]. However, due to their complex properties, the electrochemistry of organic nanoparticles has been much less studied as compared to metal or inorganic nanoparticles. In this chapter, we turn our attention to radical organic nanoparticles, 2,2-diphenyl-1-picrylhydrazyl (DPPH, as shown in Scheme 7.1) nanoparticles. DPPH is employed as a calibrant for EPR measurements and widely used in electrochemical assay for determination of total antioxidant capacity in food[26-30]. Due to its free radical structure DPPH can undergo scavenging reaction both in reduction and oxidation processes (Scheme 7.2). Despite DPPH radical molecules being electrochemically characterized in both aqueous and organic solutions[31-33] or ionic liquids[34], its electrochemistry in single nanoparticle form has not yet been investigated, although such material can now be synthesised[35].



Scheme 7.1 Structure of a DPPH molecule

In this study, both the electrochemical reduction and oxidation of single radical DPPH nanoparticles are studied using the nano-impacts method. Complete oxidation of

individual DPPH nanoparticles is inferred, with electron transfer kinetics analysed via "Butler-Volmer analysis" of single nanoparticle impacts. The reduction of DPPH nanoparticles quantitatively suggests a partial reduction process, likely leading to formation of DPPH/DPPHH core-shell nanoparticles, whereas the oxidation is quantitative. More importantly the latter shows a marked apparent difference in the overpotential required for reaction. The clear excess overpotential needed for single nanoparticle chemistry is likely a result of the greatly increased divergent mass transport seen for a single nanoparticle as compared to the appropriate linear diffusion expected for a nanoparticle ensemble. It is clear that the single nanoparticle measurements can provide information absent in cyclic voltammetry of ensembles. In particular, the oxidation of DPPH nanoparticles ensembles is electrochemically reversible whereas electrode kinetic information arose from the single particle data.



Scheme 7.2 Mechanism of DPPH reductive and oxidative reactions[32]

7.2 Experimental Section

7.2.1 Chemicals and Materials

2, 2-Diphenyl-1-picrylhydrazyl (DPPH) was obtained from Fluka Chemical Co. Acetone (ACS reagent, 99.5%), acetonitrile (anhydrous, 99.8%), tetra-n-butylammonium perchlorate (TBAP, electrochemical grade, 99%) were purchased from Sigma-Aldrich and used as received. The phosphate buffer solution (pH = 6.8) was composed of 50 mM monobasic and dibasic potassium phosphates; 0.1 M KCl used as further supporting electrolyte. All solutions were made up using ultrapure water of resistivity 18.2 MΩ cm (Millipore) at 25 °C and degassed thoroughly with N_2 (oxygen-free, BOC Gases plc) before use.

7.2.2 UV-Vis Spectroscopy

UV-Vis spectroscopy was performed using a spectrometer (U-2001, Hitachi, Mannheim, Germany) with a wavelength scan from 700 nm to 250 nm at a scan rate of 400 nm min^{-1}. A tungsten iodide and a deuterium light source were used to characterise a 50 μM OBD/acetone solution.

7.2.3 Synthesis of DPPH Nanoparticles

DPPH nanoparticles were synthesised by using the reprecipitation method [36]as detailed in Section 2.1. First, DPPH was dissolved in acetone, giving a concentration of 5 mM. Next,

200 μL DPPH/acetone solution was added to 25 mL di-ionized water in a glass round-bottom flask and thoroughly mixed by magnetic vortexing stirring at 800 rpm for 5 minutes. The solution was then subjected to sonication for 10 mins at a temperature of 25℃. The resulting mixture was a transparent purple dispersion with the appearance of a solution.

7.2.4 Characterisation of DPPH Nanoparticles

The size distributions of synthesised DPPH nanoparticles were measured by dynamic light scattering (DLS, Malvern Instruments Ltd, UK). The detailed measurements were introduced in Section 3.2.3. The size of the DPPH nanoparticles was approximately 125 nm as discussed further in Section 7.3.

7.2.5 Cyclic Voltammetry of Molecular DPPH in Organic Solvent

The instrumentations were detailed in Section 3.2.4. Cyclic voltammetry of a 1.0 mM DPPH/acetonitrile solution with 0.1 M TBAP as supporting electrolyte was measured at different scan rates from 25 mV/s up to 500 mV/s. A glassy carbon macroelectrode (GC, diameter 3.0 mm) was used as the working electrode, saturated calomel electrode (SCE) as the reference electrode while a carbon rod acted as the counter electrode. The working electrode was polished to a mirror finish on diamond sprays (Kemet, Kent, UK) in the sequence of size 3.0, 1.0 and 0.1 μm. All electrochemical measurements were thermostated at 25 °C. Additional data analysis and curve fitting was made by using GPES and Origin Pro 9 (Origin Lab Corporation).

7.2.6 Cyclic Voltammetry of DPPH Nanoparticles in Aqueous Solution

The electrochemical set-up and electrodes were used as same as in Section 7.2.5. For the modification of the working electrode, 2 μL of freshly prepared DPPH nanoparticle suspension (molecular concentration: 4×10^{-5} mol L^{-1}) was dropped on the surface of the glassy carbon electrode, then the electrode was left in nitrogen for about 20 mins to evaporate the solvent. Cyclic voltammetry was subsequently used for electrochemical studies with the modified electrode in three electrolytes: 0.1 M PBS buffer (pH = 6.8) with 0.1 M KCl as supporting electrolytes, 1 M KNO_3 and 1 M $NaNO_3$ at different scan rates from 25 mV/s to 100 mV/s at a temperature of 25 °C. The working electrode was also polished before each scan.

7.2.7 Nano-impacts of DPPH Nanoparticles

The detailed "nano-impacts" method was described in Section 2.4. For the study of electrochemistry and sizing of single DPPH nanoparticles, a same carbon microelectrode as in Section 6.2.6 (diameter = 11 μm) was used as the working electrode and the same reference and counter electrodes as in Section 7.2.5 were employed. The chronoamperometry was performed in a PBS buffer (pH = 6.8) at various potentials from +0.55 V to + 0.9 V for single DPPH nanoparticles oxidation and at - 0.1V and 0 V for single DPPH nanoparticles reduction. Solutions were thoroughly degassed with nitrogen (oxygen-free, BOC Gases plc) prior to all the experiments. Signal Counter was used for analysis of the impact spikes observed and OriginPro 9 for statistical analysis on nanoparticle size.

7.3 Results and Discussion

First, to explore the reduction and oxidation of molecular DPPH, cyclic voltammetry was applied to study *molecular* DPPH in acetonitrile with TBAP as supporting electrolyte. We then studied the electrochemistry of an ensemble of DPPH nanoparticles drop-casted on the electrode in three different aqueous solutions and in particular the electrochemical properties in 0.1 M PBS buffer. Finally, the nano-impacts method was applied to study the reduction and oxidation of single DPPH nanoparticles and characterize the size as well as the electron transfer kinetics of single DPPH nanoparticles for comparison with those seen from the ensemble.

7.3.1 UV-Vis Spectroscopy of DPPH in Acetone

A solution of 50 µM DPPH in acetone was prepared and then characterised by UV-Vis spectroscopy as shown in Figure 7.1. A significant absorption band was observed at the wavelength of 517 nm, which is in agreements with previous literatures[38-40], suggesting the DPPH staying stable in acetone phase.

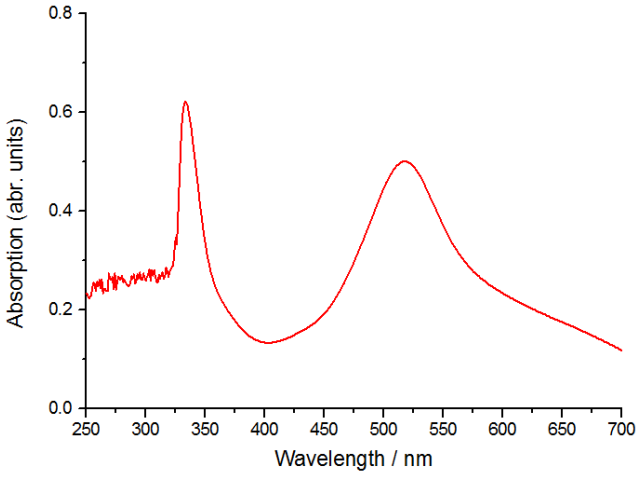


Figure 7.1 UV-Vis spectroscopy of 0.05 mM DPPH in acetone

7.3.2 Electrochemistry of DPPH in Acetonitrile/TBAP

Cyclic voltammetry of 1.0 mM DPPH in acetonitrile with 0.1 M TBAP as supporting electrolyte was measured at a bare glassy carbon immersed in at different scan rates from 25 mV/s to 500mV/s as shown in Figure 7.2. The term 'reductive' implies that the potential was initially set at + 0.5 V and then scanned in a cathodic direction and that the term 'oxidative' implies a scan in an anodic direction. The cyclic voltammetric response shows a cathodic peak at +0.22 V and an anodic peak at +0.81 V. These are attributed to the formation of a DPPHH and a DPPH monocation respectively (see Scheme 7.2). A similar observation was seen for the reduction of and oxidation of molecular DPPH in other organic solvents[34, 41]. Both the reductive process and the oxidative process are thought to involve one electron transfer as shown in Scheme 7.2.

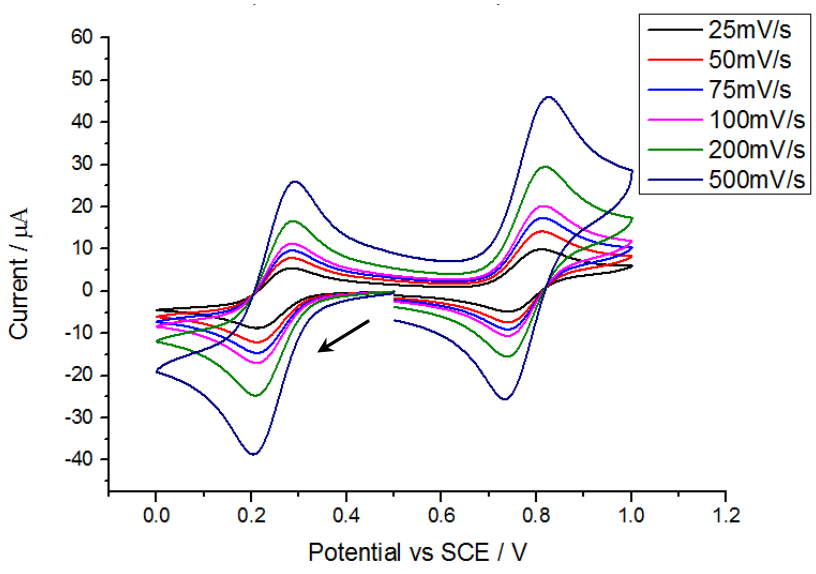


Figure 7.2 The cyclic voltammetric response of 1.0 mM DPPH in acetonitrile with 0.10 M TBAP as supporting electrolyte at scan rates of 25 mV/s (black), 50 mV/s (red), 75 mV/s (blue), 100 mV/s (magenta),200 mV/s (green) and 500 mV/s (dark blue).

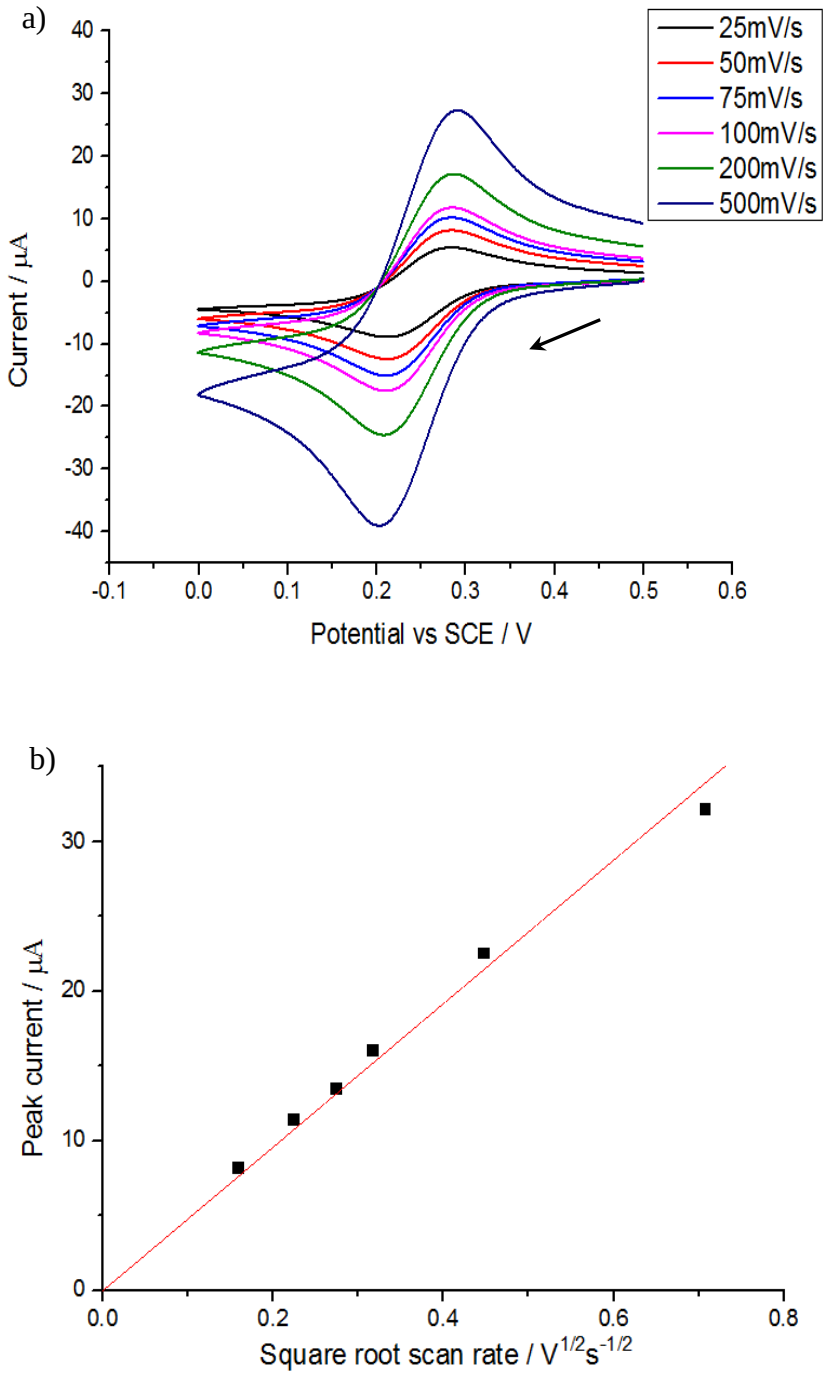


Figure 7.3(a) The cyclic voltammetric reductive response of 1.0 mM DPPH in acetonitrile with 0.10 M TBAP as supporting electrolyte at scan rates of 25 mV/s (black), 50 mV/s (red), 75 mV/s (blue), 100 mV/s (magenta), 200 mV/s (green) and 500 mV/s (dark blue); (b) Reductive peaks current versus Square root of scan rates from 25 mV/s to 500 mV/s.

Figure 7.3(a) shows the electrochemical reductive response of DPPH at scan rates from 25 mV/s to 500 mV/s. The peak separation between the forward peaks and backward peaks is around 60 mV which indicates that the reduction of DPPH is a one electron electrochemically reversible process. By plotting the peak current versus square root of scan rate, a linear relationship was observed (Figure 7.3(b)). By using the Randles–Sevcik equation as given in Chapter 1 and Section 6.3.1, diffusion coefficient of DPPH was then calculated to be 6.4×10^{-6} cm^2s^{-1}.

$$I_P = 2.69 \times 10^5 A D^{1/2} C_{DPPH} v^{1/2} \qquad \text{(Eqn 7.1)}$$

where I_P is the peak current, A is the surface area of the glassy carbon macroelectrode, C_{DPPH} is the concentration of DPPH in acetonitrile and v is the scan rate.

Next the cyclic voltammetric oxidative response of DPPH was conducted at different scan rates ranging from 25 mV/s to 500 mV/s as shown in Figure 7.4(a), which again gave a peak to peak separation of ca. 60 mV/s, indicating a one electron electrochemically reversible process for the oxidation of DPPH. By plotting the current of the anodic peaks versus square root of scan rate (Figure 7.4(b)) and using Equation 7.1, the diffusion coefficient of DPPH was found as 6.5×10^{-6} cm^2s^{-1}, which is in excellent agreement with that estimated from the reduction of DPPH. Together these results further confirm that one electron oxidation and reduction processes are taking place.

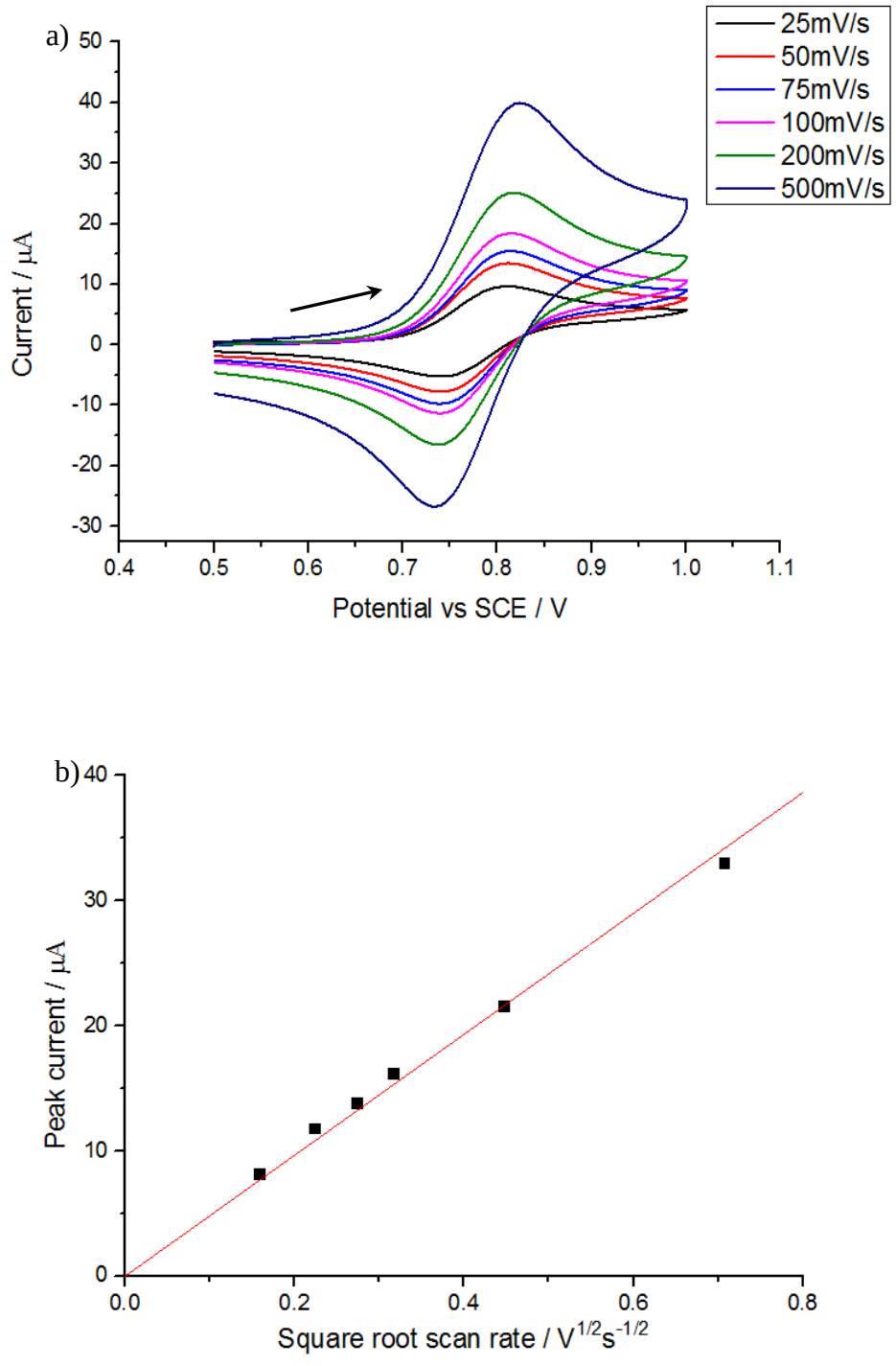


Figure 7.4(a) The cyclic voltammetric oxidative response of 1.0 mM DPPH in acetonitrile with 0.10 M TBAP as supporting electrolyte at scan rates of 25 mV/s (black), 50 mV/s (red), 75 mV/s (blue), 100 mV/s (magenta), 200 mV/s (green) and 500 mV/s (dark blue); (b) Oxidative peaks current versus square root of scan rate from 25 mV/s to 500 mV/s.

7.3.3 Electrochemical Characterization of DPPH Nanoparticles Drop Cast on an Electrode Surface

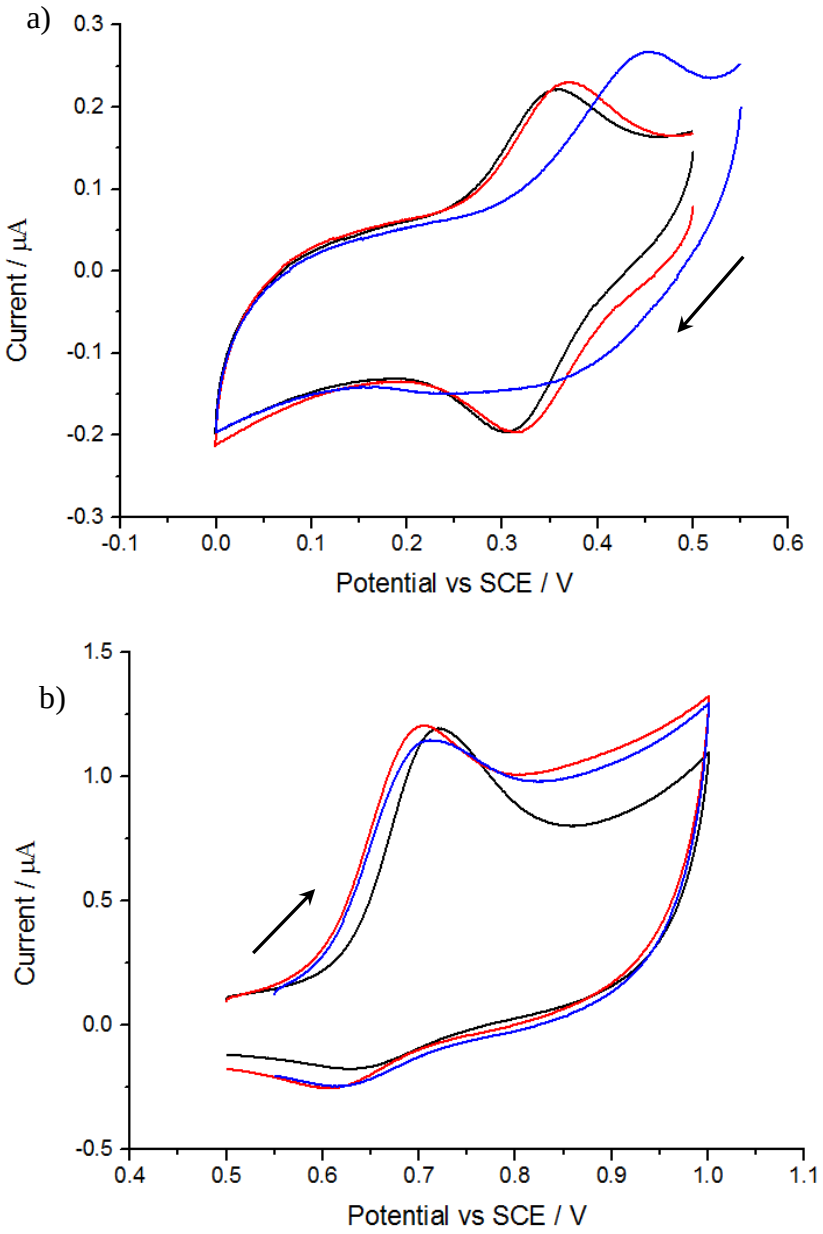


Figure 7.5 Cyclic voltammetric response of a DPPH nanoparticles modified GC electrode in a 0.1 M PBS buffer (black) (pH = 6.8), 1 M KNO_3 solution (red) and 1 M $NaNO_3$ solution (blue) at a scan rate of 25 mV/s (a) reduction and (b) oxidation.

Cyclic voltammetry was recorded for a DPPH nanoparticle modified glassy carbon electrode made by the drop casting method in 0.1 M PBS buffer (pH = 6.8), 1 M KNO_3 and 1 M $NaNO_3$, at a scan rate of 25 mV/s at room temperature (25 ± 0.2°C) as shown in

Figure 7.5. The redox properties of DPPH nanoparticles were studied. Suitable potentials of reduction (about +0.30 V in 0.1 M PBS buffer and 1 M KNO_3; +0.45 V in 1 M $NaNO_3$) and oxidation (the oxidative potentials of approximate +0.75 V in three electrolytes) of DPPH nanoparticles were determined.

In Figure 7.5(a), it can be seen that the cyclic voltammetry of reduction of DPPH nanoparticles show a similar shape in 0.1 PBS buffer (pH = 6.8, 0.1 M KCl as supporting electrolyte) and in 1 M KNO_3, while a less well-defined reductive peak was observed, with the backward peak shifted to a more positive potential around +0.45 V in 1 M $NaNO_3$. We assume that reduction of the nanoparticles is accompanied by uptake of H^+, K^+ and/or Na^+ with the nanoparticles as discussed further below. Analogous different insertion capacity of various cations has also been observed for various organic films[42-44]. The cyclic voltammetry of the oxidation of DPPH nanoparticles in three electrolytes is shown in Figure 7.5(b). Similar peak shapes and oxidative potentials (of approximately +0.75 V) were seen in all three electrolytes.

Cyclic voltammetry of the oxidation and reduction of DPPH nanoparticles in 0.1 M PBS buffer, 1 M KNO_3 solution and 1 M $NaNO_3$ solution at different scan rates were recorded as shown in Figure 7.6. Variable scan rate data showed a loss of a back peak at low scan rates so the dissolution of the generated oxidised DPPH nanoparticles were inferred contrasting with the reduction process which was chemically reversible.

By plotting the peaks currents versus scan rate in each electrolyte, linear relationships were observed as shown in Figure 7.7. (Due to the poor-defined peak, the data of reduction of DPPH nanoparticles in 1 M $NaNO_3$ solution was not plotted in the Figure 7.7(a)).

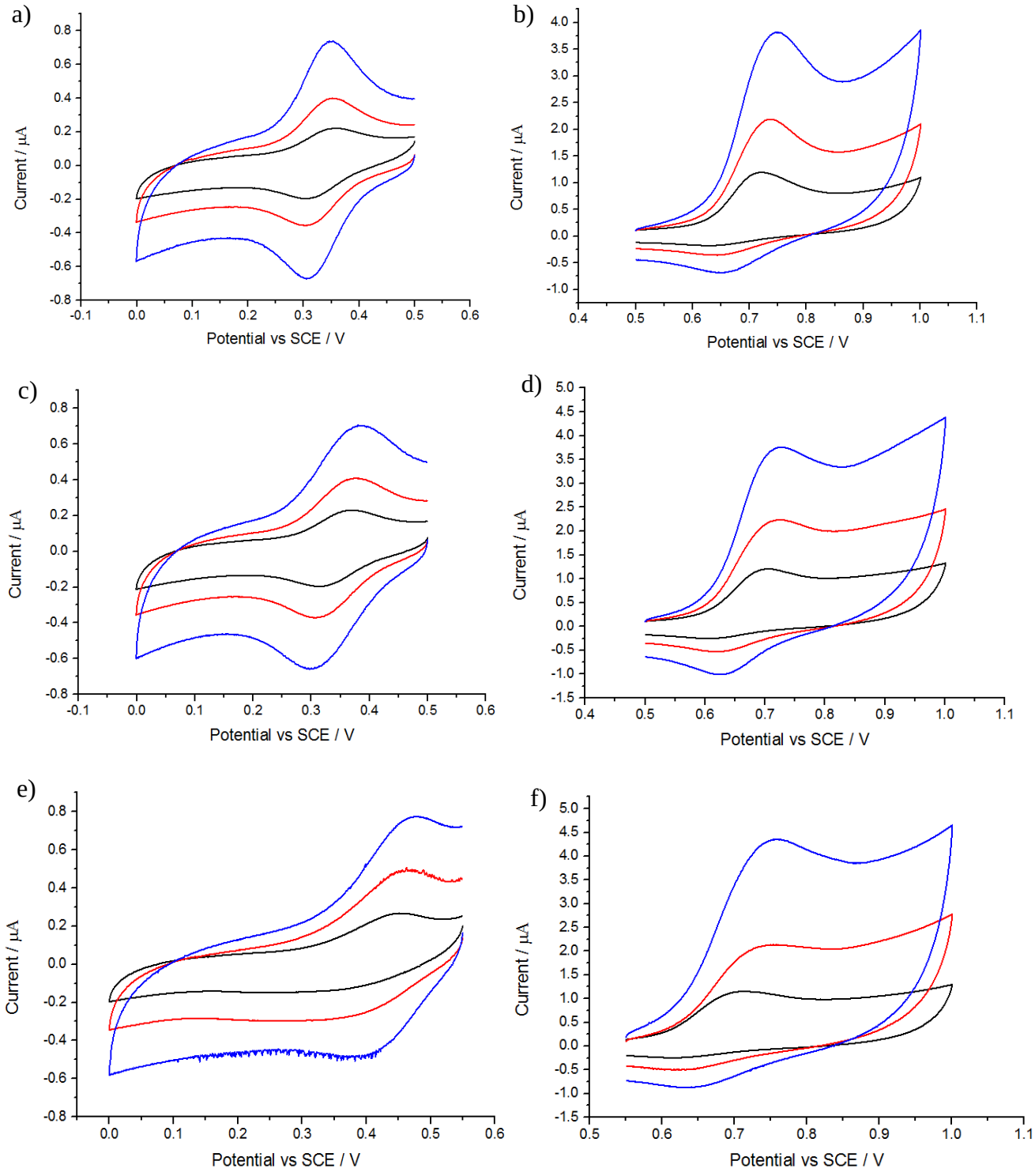


Figure 7.6 Cyclic voltammetric response of a DPPH nanoparticles modified GC electrode in three electrolytes at different scan rates of 25 mV/s (black), 50 mV/s (red) and 100 mV/s (blue). Reduction (a) in 0.1 M PBS buffer (pH = 6.8), (c) in 1M KNO_3 solution and (e) in 1 M $NaNO_3$ solution and oxidation (b) in 0.1 M PBS buffer (pH = 6.8), (d) in 1 M KNO_3 solution and (f) in 1 M $NaNO_3$ solution

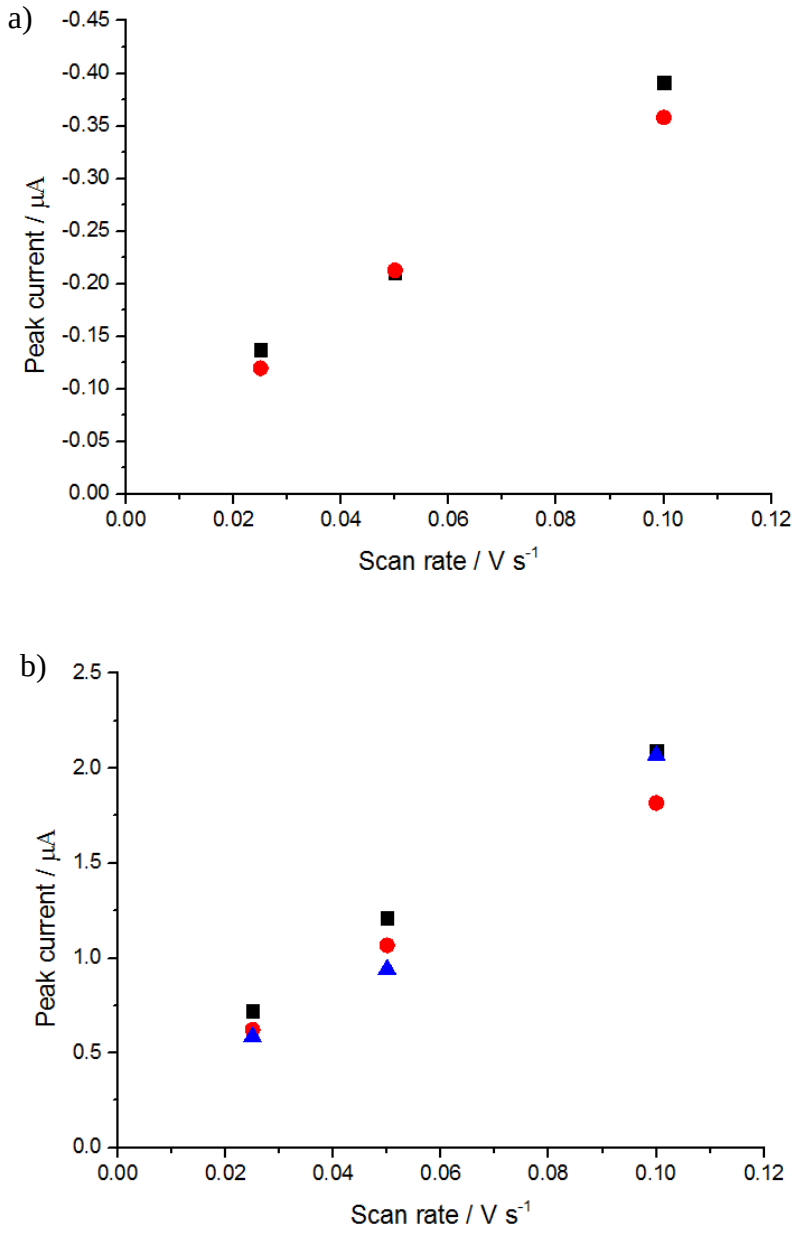


Figure 7.7 (a) Reductive and (b) Oxidative peaks current versus scan rates of 25 mV/s,50 mV/s and 100 mV/s in 0.1 M PBS buffer (pH = 6.8) (black), 1M KNO_3 solution (red) and 1 M $NaNO_3$ solution (blue).

Figure 7.8 shows the first scan and second scan of reduction and oxidation of DPPH nanoparticle modified glassy carbon electrode in 0.1 M PBS buffer. For the reductive behaviour shown in Figure 7.8(a), there is a significant cathodic peak at +0.30 V for the first scan, which likely corresponds to the DPPH reduction on the surface of the glassy carbon electrode. The backward peak around +0.35 V may be attributed to a re-oxidation

process. The second scan then reveals an almost superposition of the first scan, which indicates there was nearly the exact same charge passed during oxidation and reduction between the two consecutive scans. Therefore, it suggests that for DPPH nanoparticles drop-casted on the electrode, the reduction of DPPH nanoparticles shows a chemically reversible process which involves the transition between DPPHH (or $DPPH^- Na^+$ or $DPPH^- K^+$) nanoparticles to DPPHH nanoparticles on the surface of the electrode.

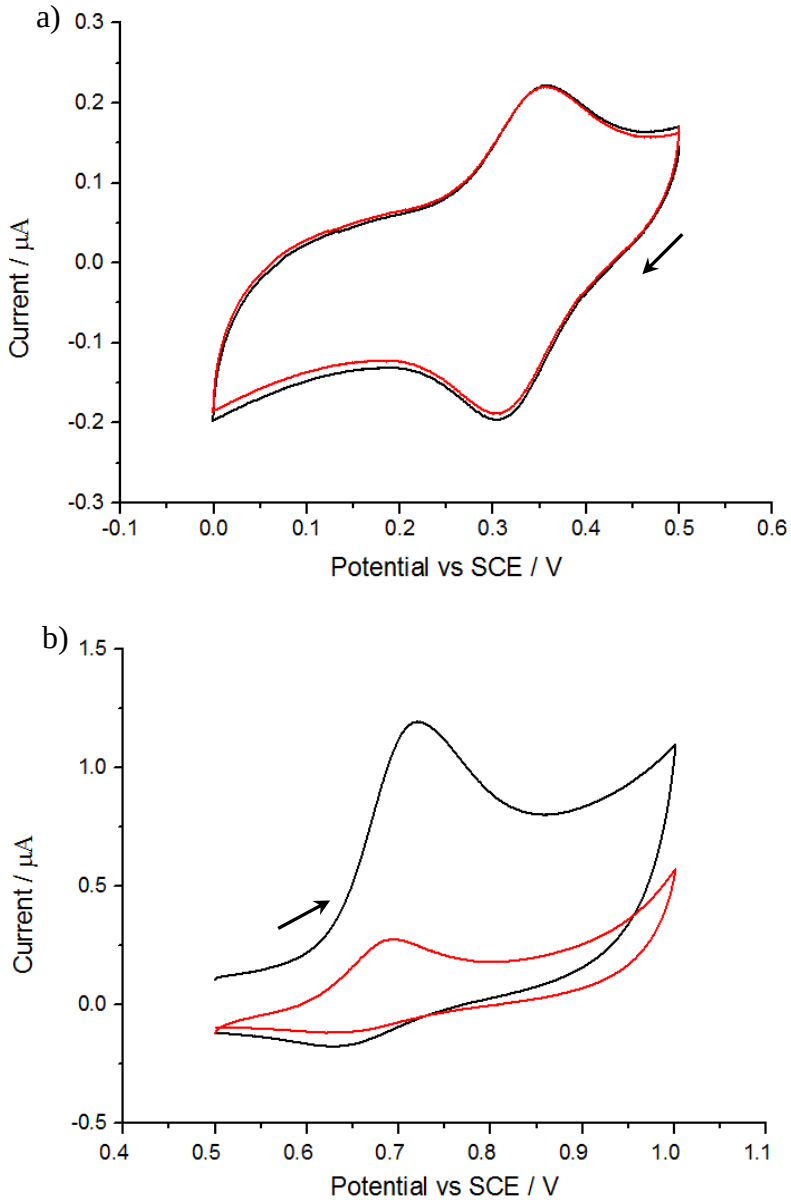


Figure 7.8 Cyclic voltammetric response of a DPPH nanoparticles modified GC electrode in a 0.1 M PBS buffer (pH = 6.8), at a scan rate of 25 mV/s (black: first scan, red: second scan) (a) reduction and (b) oxidation.

The cyclic voltammetry of the oxidative response of DPPH nanoparticles is shown in Figure 7.8(b). An anodic peak was observed around +0.75 V at the first scan, which was attributed to the oxidative reaction of DPPH nanoparticles. The loss of signal at back peak is related to some dissolution of oxidized DPPH nanoparticles.

Further, if it is assumed that there is a monolayer of DPPH nanoparticles drop-casted on the electrode surface with a consistent spacing between nanoparticles, the average separation between DPPH nanoparticles can be estimated. Specifically, The number of DPPH nanoparticles N on the electrode is calculated as 2.20×10^7 by Equation 7.2:

$$N = \frac{nM}{\frac{4}{3}\pi r_{np}^3 \rho} \quad \text{(Eqn 7.2)}$$

where n is the number of monomer moles of DPPH drop-casted on the surface of the glassy carbon electrode in the form of DPPH nanoparticles, M is molecular weight of DPPH, ρ is density of DPPH, r_{np} is radius of DPPH nanoparticles obtained from DLS measurement.

If the nanoparticles stay as monolayer on the surface of the electrode, the surface coverage of DPPH nanoparticles S occupied on the glassy carbon electrode then can be estimated as ca 3.8 % by using Equation 7.3:

$$S = \frac{N\pi r_{np}^2}{A} \quad \text{(Eqn 7.3)}$$

where A is the surface area of the glassy carbon electrode.

Then the area unit for one DPPH nanoparticle array can be calculated as 3.21×10^{-13} m^2 and the separation d_{np} between DPPH nanoparticles can be estimated to be around 580 nm by Equation 7.4:

$$d_{np} = \sqrt[2]{\frac{A}{N}} \qquad \text{(Eqn 7.4)}$$

Figure 7.9 shows the DPPH nanoparticles array on the surface of the glassy carbon electrode. $\sqrt{2Dt}$ was estimated to be 36 μm $\gg$ d_{np} (diffusion coefficient of DPPH was taken from Result and Discussion 7.3.1 as 6.4×10^{-6} cm^2 s^{-1}), indicating this is the so called Case 4[45] where diffusion layers from adjacent particles heavily overlap. In this case, a linear diffusion model to or from the surface arise at the scan rate used [45, 46] here for ensembles of DPPH nanoparticles, where diffusion layers heavily overlap and peak-shaped voltammetry is obtained, as shown in Figure 7.8.

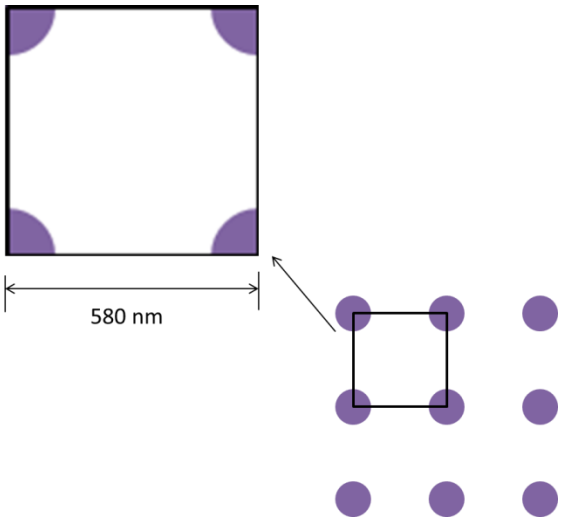


Figure 7.9 DPPH nanoparticles array on the surface of a GC electrode

The oxidative charge and reductive charge can be obtained from the integration of the peaks from first scans (Figure 7.8) as 3.4×10^{-6} C and 6.8×10^{-7} C. Assuming the DPPH nanoparticles undergo a one electron transfer per one monomer unit, 44.1% and 8.8% of that expected for 100% oxidation and reduction of drop-cast films was estimated respectively. The incomplete stripping may be due to the aggregation of DPPH nanoparticles where only the nanoparticles inside the aggregated particle that are in contact with the electrode are oxidised or reduced[10]. Overall, the mechanism of reduction and oxidation of DPPH nanoparticles is difficult to be elucidated from ensembles of nanoparticles drop-casted on the electrode. The mechanism of reduction and oxidation of single DPPH nanoparticles will be discussed next using the nano-impacts method.

7.3.4 Nano-impacts of DPPH nanoparticles

To study the oxidation of single DPPH nanoparticles, a micro carbon electrode was immersed in a PBS buffer (pH = 6.8) solution and a known concentration of DPPH nanoparticles solution added. The oxidative potential was fixed at a potential selected between +0.55 V and +0.90 V for chronoamperometric measurements of individual DPPH nanoparticle collisions with the electrode, as recorded by current spikes in the current time response with each spike representing a single impact[21]. The onset of spikes were found to be dependent on the oxidative potentials and no oxidative spikes of DPPH nanoparticles at lower the oxidative potentials of +0.65 V or below, further confirming by comparing with Figure 7.12(b) that the spikes correspond to Faradaic oxidation of DPPH nanoparticles. In addition, the amplitude of these Faradaic spikes was also found to be dependent on the oxidative potential. Figure 7.10(a) shows a typical chronoamperometric profile of

oxidative Faradaic spikes of individual DPPH nanoparticles at +0.80 V vs. SCE in PBS buffer.

The oxidative charge from complete oxidation of single DPPH nanoparticles was calculated by integrating the area of each spikes by analysing a total number of 333 impact spikes observed at sufficient or more positive potential than +0.8 V. Figure 7.10(b) shows the histogram of the charge obtained from DPPH nanoparticles, giving an average charge of 3.5×10^{-13} C.

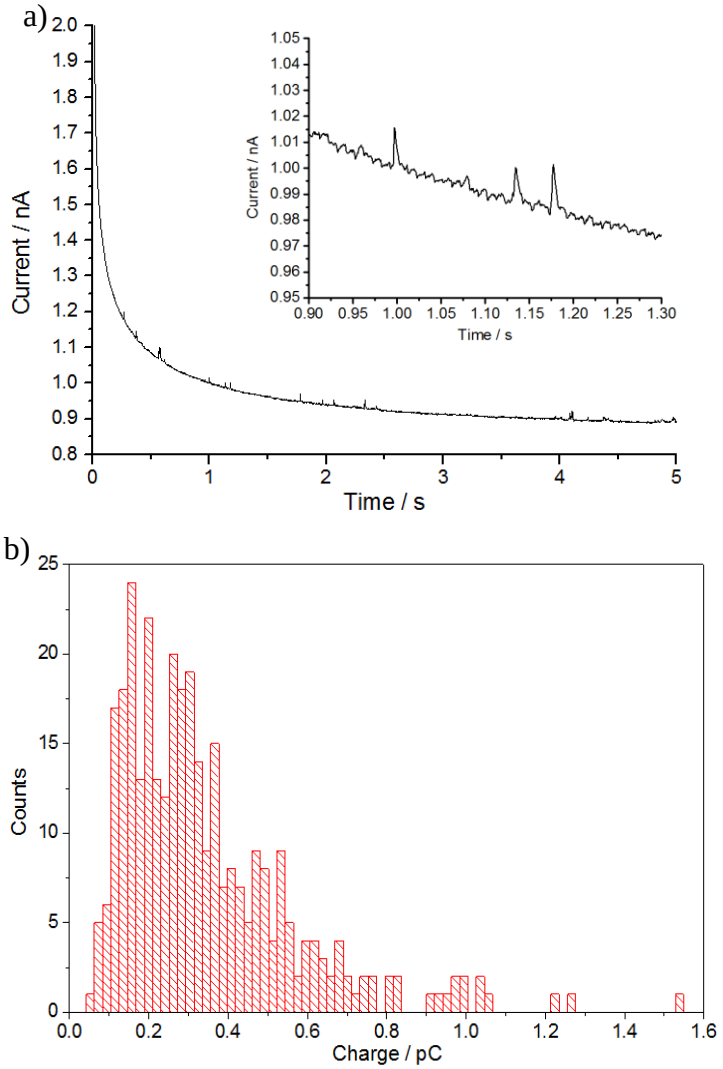


Figure 7.10 (a) Chronoamperometric profiles showing oxidative and reductive Faradaic spikes of DPPH nanoparticles in PBS buffer (pH = 6.8) at +0.80 V vs. SCE. The inset showing the detailed impact spikes. (b) Histogram showing the DPPH nanoparticles completed oxidative charge at potentials between +0.80 V and +1.0 V.

The size of DPPH nanoparticles was then determined by Equation 7.5, assuming DPPH nanoparticles are spherical, with an average size of DPPH nanoparticles estimated to be 125 ± 25 nm.

$$D_{np} = 2 \times \sqrt[3]{\frac{3MQ}{4nF\pi\rho}} \qquad \text{(Eqn 7.5)}$$

where D_{np} is the diameter of the DPPH nanoparticles, M is the molar mass of DPPH, ρ is the density of DPPH and F is the Faraday constant. The parameter n is the number of electrons transferred per DPPH molecule (n = 1) as discussed above.

The size distribution was also determined and was in a good agreement with the size distribution from dynamic light scattering as shown in Figure 7.11, confirming a complete oxidation of the single DPPH nanoparticles.

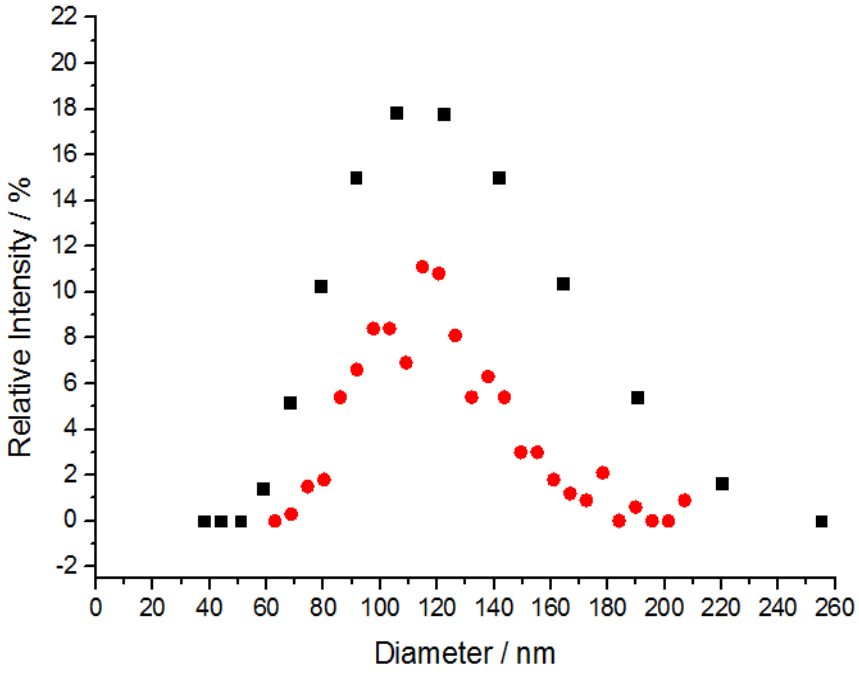


Figure 7.11 size distributions of DPPH nanoparticles obtained from electrochemical sizing of completed oxidative nano-impacts experiments (red dots) and DLS analysis (black dots).

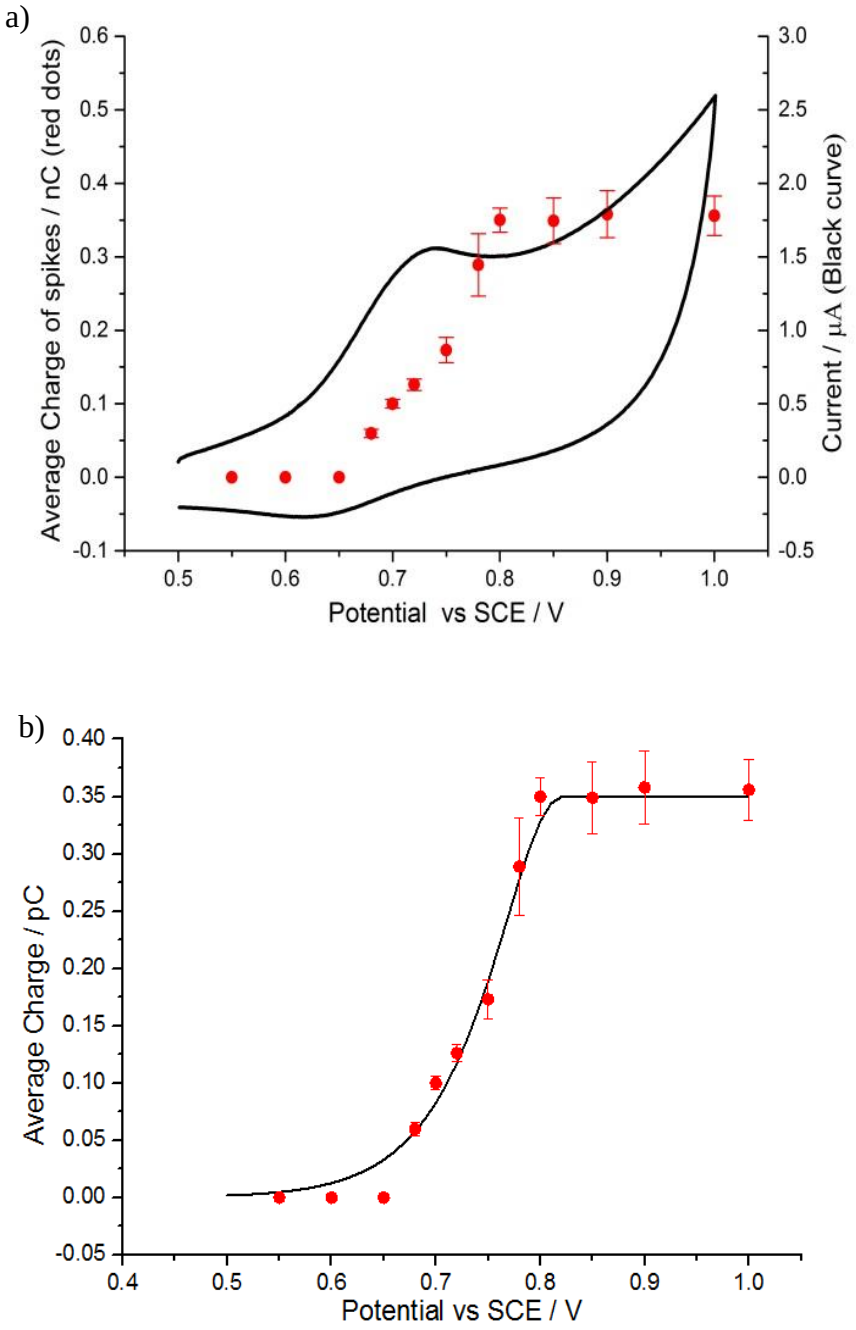


Figure 7.12(a) average charge Q for oxidation vs. potential E (red dots) of individual DPPH nanoparticles and cyclic voltammogram of oxidation of the ensemble of DPPH nanoparticles. (b) fitted "voltammogram" of single DPPH nanoparticles (red dots), showing average charge Q for oxidation of individual DPPH nanoparticles vs. potential E. A plot of Q vs. E for experimental data points against theoretical fitting for irreversible electron transfer given by Equations 7.6, 7.7 and 7.8. The parameters used for the fitting are r_i = 62.5 nm, ρ = 1.40 g cm^{-3}, (n' + α) = 0.5 (so n' = 0) and $k^0 exp\left(\frac{(n'+\alpha)F}{RT}E_f^\theta\right)$ = 1 x10^{-9} m s^{-1} (vs. SCE).

Secondly, to further investigate the electron transfer kinetics of single DPPH nanoparticles, an "effective voltammogram" of single DPPH nanoparticles is measured using the average charge transfer to the nanoparticles as a function of potential, as illustrated in Figure 7.12. By comparing with the cyclic voltammetry of an ensemble of DPPH nanoparticles (Figure 7.12(a)), the latter shows electrochemically reversible behaviour because of relatively slow mass transport; in contrast the single nanoparticles shows much faster transport and hence irreversible behaviour; a clear 50 mV overpotential is seen for complete oxidation of individual DPPH nanoparticles as compared to the reversible ensemble limit.

By using the Butler-Volmer equation as discussed in Chapter 1, the electrochemical flux can be given by Equation 7.6 for the oxidation of individual DPPH nanoparticles, which relates the change in particle size to the applied potentials[20, 47].

$$j = -\frac{\rho}{M}\frac{dr}{dt} = k^0[C]^0 \exp\left(-(n' + \alpha)\theta\right) \qquad \text{(Eqn 7.6)}$$

where j is the flux (mol m^{-2} s^{-1}), ρ is the density of the material (g m^{-3}), M is the molecular weight of the monomer (g mol^{-1}), r is the radius of the nanoparticle (m),t is time (s), k^0 is the electrochemical rate constant (m s^{-1}), $[C]^0$ is the standard concentration (1 mol dm^{-3}), $n' = 0$ in the present case, as $n'$is the number of electrons transferred prior to the rate determining step, α is the transfer coefficient of the rate determining electron transfer and θ is the dimensionless potential $\frac{F}{RT}(E - E_f^{\theta})$.

Integration of Equation 7.6 readily yields an expression for the change in the nanoparticle radius as a function of impact time and the applied potential:

$$r_f = r_i - \frac{M}{\rho} t_L k^0 [C]^0 \exp\left(\frac{(n'+\alpha)F}{RT} E_f^\theta\right) \exp\left(\frac{-(n'+\alpha)F}{RT} E\right) \quad \text{(Eqn 7.7)}$$

where r_i is the average initial particle radius (m) and r_f is the average final particle radius after impact (m), t_L is the average nanoaprticle impact time and all other symbols are the same as stated above.

Further this change in radius can be also related to the charge passed during the reduction of the nanoparticle using the following expression:

$$Q = \frac{4nF\pi\rho}{3M}(r_i^3 - r_f^3) \quad \text{(Eqn 7.8)}$$

where Q is the charge passed during the impact and n is the number of electrons transferred for the full reduction of the monomer unit.

By plotting the average charge passed during the oxidation of individual nanoparticles against the applied electrode potential and fitting the above theoretical model to the experimental data through the use of Equations 7.7 and 7.8 (Figure 7.12(b)), the transfer coefficient α of the single DPPH nanoparticles can be determined to be 0.5 ± 0.05, with the combined parameter $k^0 \exp\left(\frac{\alpha F}{RT} E_f^\theta\right)$ found to have the value of 1×10^{-9} m s^{-1}.

Next, the electrode was held at a selected reductive potential for chronoamperometric measurements of reduction of individual DPPH. The potentials were selected at 0 V and -0.1 V which is much more negative than the ensemble reduction potential of DPPH (as

suggested by the data in Figures 7.10), ensuring the reduction of DPPH nanoparticles are not limited by the potentials so that fully driven electron transfer can be seen. Figure 7.13 shows an example of chronoamperometry of reductive faradaic spikes of DPPH nanoparticles at -0.1 V vs. SCE in PBS buffer (pH = 6.8).

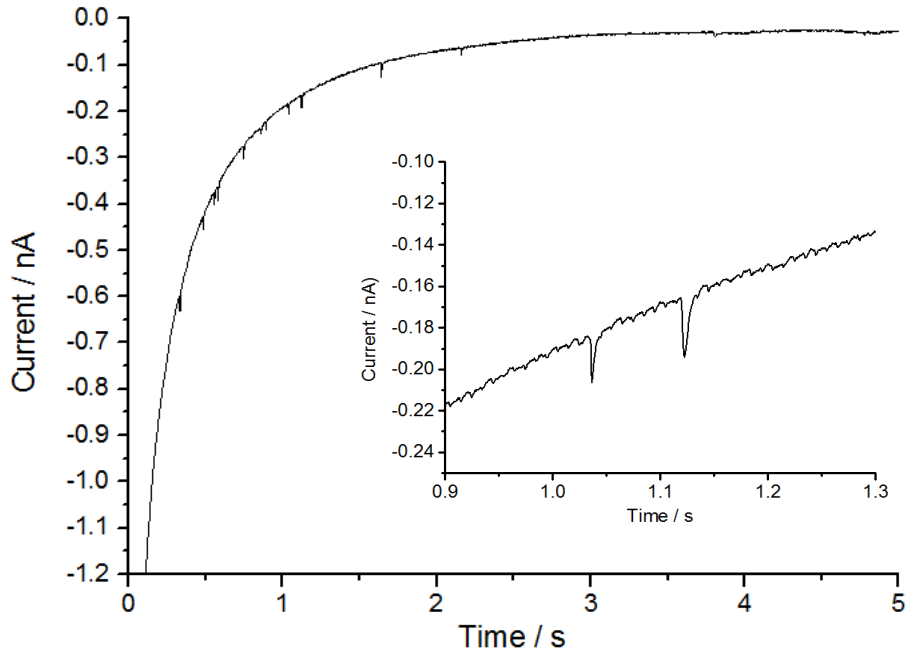


Figure 7.13 Chronoamperometric profiles showing and reductive Faradaic spikes of DPPH nanoparticles in PBS buffer (pH= 6.8) at -0.1 V vs. SCE. The inset showing the detailed reductive impact spikes.

Reductive nano-impacts of DPPH nanoparticles were conducted at 0 V and -0.1 V, giving an average charge of -1.95×10^{-13} C from analysing 436 reductive spikes (Figure 7.14(a)) and -1.91×10^{-13} C from 464 reductive spikes (Figure 7.14(b)), respectively. The charge is seen potential independent (the same value at 0 V or at -0.1 V), suggesting the maximum charge injection is realised. No reductive spikes were observed at more positive potential than 0 V, indicating the onset of reductive spikes was also found to be dependent on the

reductive potentials. A total number of 900 reductive spikes from 0 V and -0.1 V gives an average charge of -1.93×10^{-13} C, as shown in Figure 7.14(c).

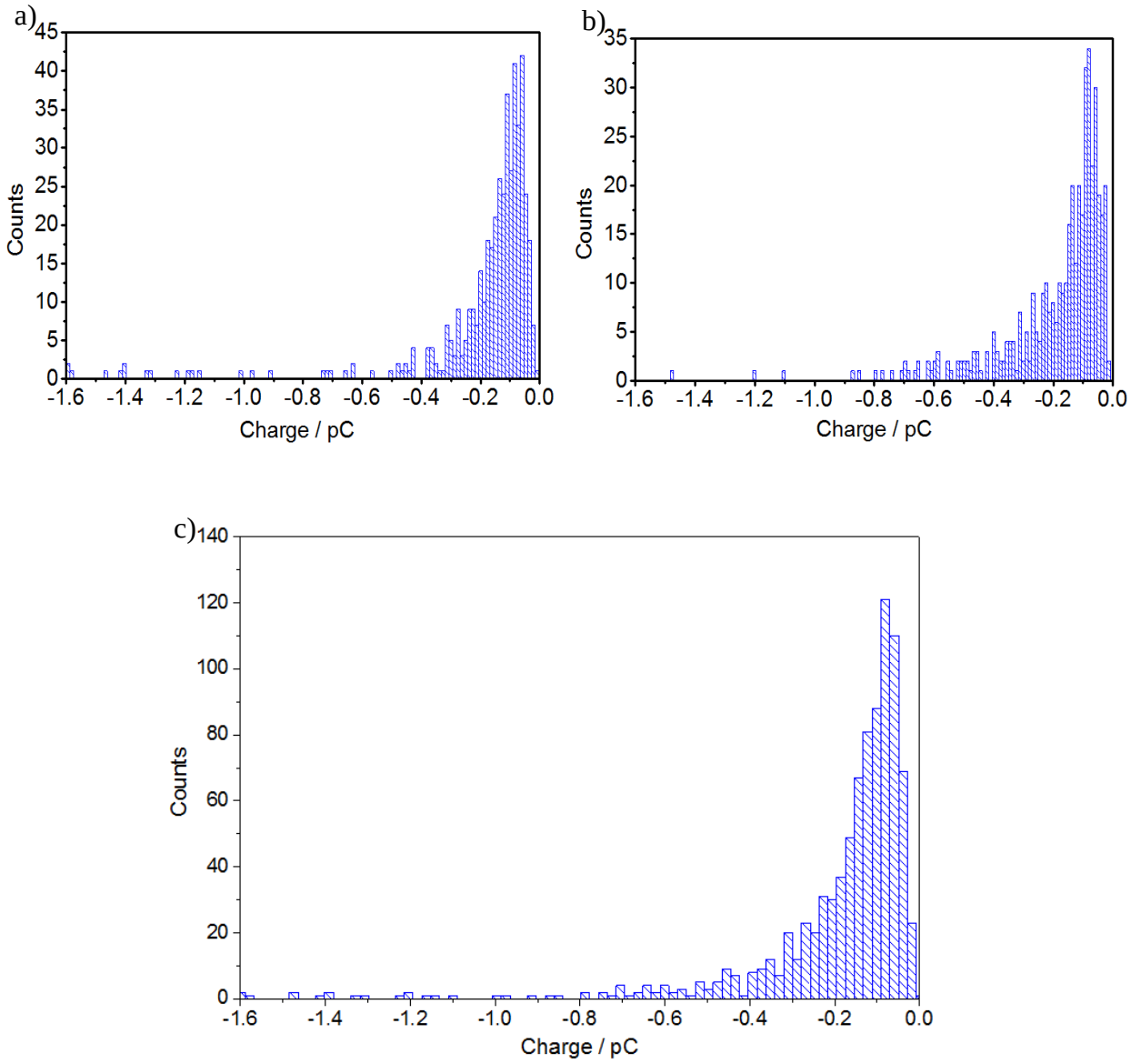


Figure 7.14 Histograms showing the reductive charge distribution from reduction of single DPPH nanoparticles at a potential of (a) 0 V, (b) -0.1 V and (c) charge from accumulative spikes at 0 V and -0.1V

To investigate the nature of the reduction of single DPPH nanoparticles, we then plotted absolute charge distribution from oxidation and reduction from nano-impacts, as shown in Figure 7.15. It can be seen that the absolute charge of the reductive spikes is less than that of completed oxidative spikes.

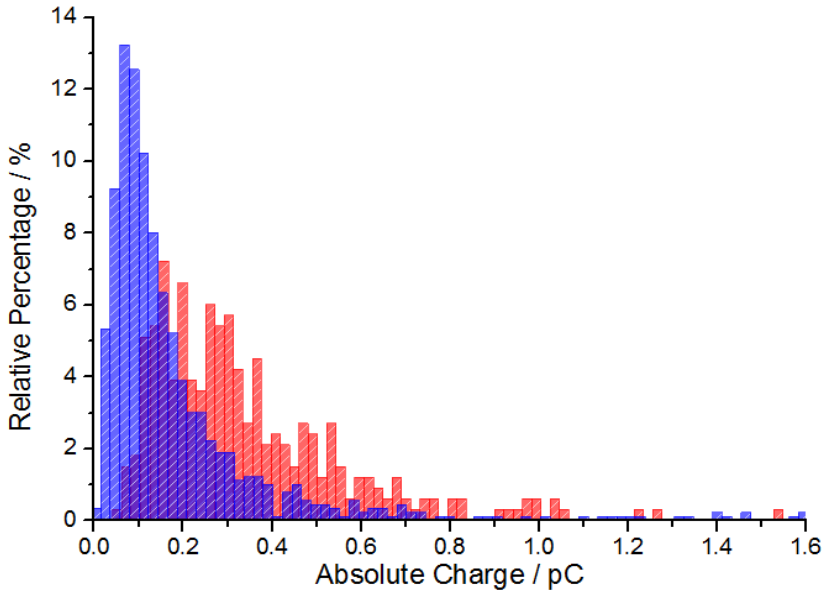


Figure 7.15 Relative percentage vs. absolute charge of oxidative spikes (red) and reductive spikes (blue) from nano-impacts.

This may be attributed to the fact that there is full oxidative dissolution of the DPPH nanoparticles by the formation of DPPH cations (Scheme 7.2), while a layer of reduced DPPH is formed so there is partial reduction of the nanoparticles as illustrated in Figure 7.16. In the latter case, cations were inserted to achieve charge neutralization of the reduced DPPH, where the electro insertion of sodium and potassium cations exhibit different capacities (Figure 7.5).

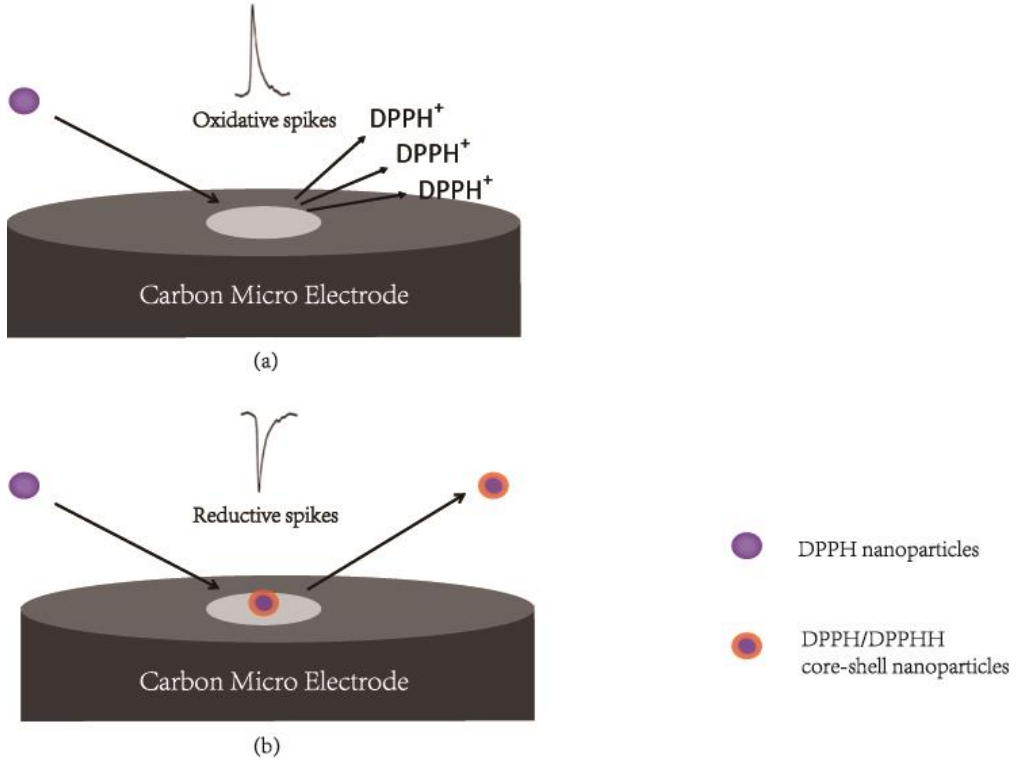


Figure 7.16 Schematic diagrams illustrating (a) the oxidation and (b) the reduction of single DPPH nanoparticles collision process during nano-impacts.

Further, if we assume the DPPH nanoparticle is sphere, and the partial reduction on the single DPPH nanoparticle is homogeneous on the surface of nanoparticle, the remaining diameter of the DPPH nanoparticle D_r after reduction can be estimated to be 96 nm, with an "outer shell" of DPPHH thickness approximately ca. 14.5 nm, according to Equation 7.9:

$$D_r = 2 \times \sqrt[3]{\frac{3M(Q-Q_r)}{4nF\pi\rho}} \qquad \text{(Eqn 7.9)}$$

where D_r is the remaining diameter of DPPH nanoparticles, Q is the total charge if there is full reduction for a DPPH nanoparticle of diameter 125 nm, Q_r is the actual reductive charge from individual DPPH nanoparticle, M is the molar mass of DPPH, ρ is the density of DPPH and F is the Faraday constant. The parameter n is the number of electron transferred of DPPH nanoparticles (n = 1).

7.4 Conclusions

In this chapter, the electrochemical reduction and oxidation of single DPPH nanoparticles using the nano-impacts method is studied. Complete oxidation of individual DPPH nanoparticles was inferred, with electron transfer kinetics analysed via the Butler-Volmer theory for single nanoparticles. The reduction of DPPH nanoparticles quantitatively suggests a partial reduction process, likely leading to formation of DPPH/ reduced DPPH core-shell nanoparticles. An important difference between the ensemble and the single nanoparticles chemistry is the emergence of a clear overpotential in the oxidation as a result of the greatly increased mass transport seen for a single nanoparticle as compared to the approximately linear diffusion expected for a nanoparticle ensemble. It is clear that the single nanoparticle measurement can provide information absent in the cyclic voltammetry of ensembles.

In the next chapter, the nano-impacts method is applied in the quantification of ion insertion into organic nanoparticles. The insertion process is inferred to be limited and controlled by the formation of a thin shell of salt formed near the surface of the nanoparticle.

References

1. Z. Fan and F. B. Prinz, *Nano Letters*, 2011, **11**, 2202-2205.
2. N. M. Markovic, *Nature Materials*, 2013, **12**, 101-102.
3. X. C. Jiang, J. S. Hu, E. R. Petersen, L. A. Fitzgerald, C. S. Jackan, A. M. Lieber, B. R. Ringeisen, C. M. Lieber and J. C. Biffinger, *Nature Communications*, 2013, **4,** 2751-2756.
4. C. Burda, X. B. Chen, R. Narayanan and M. A. El-Sayed, *Chemical Reviews*, 2005, **105**, 1025-1102.
5. Y. Wang, E. Laborda, C. Salter, A. Crossley and R. G. Compton, *Analyst*, 2012, **137**, 4693-4697.
6. S. R. Belding, E. J. Dickinson and R. G. Compton, *The Journal of Physical Chemistry C*, 2009, **113**, 11149-11156.
7. S. R. Belding and R. G. Compton, *The Journal of Physical Chemistry C*, 2010, **114**, 8309-8319.
8. H. S. Toh, C. Batchelor-McAuley, K. Tschulik, M. Uhlemann, A. Crossley and R. G. Compton, *Nanoscale*, 2013, **5**, 4884-4893.
9. C. C. Neumann, E. Laborda, K. Tschulik, K. R. Ward and R. G. Compton, *Nano Research*, 2013, **6**, 511-524.
10. S. J. Cloake, H. S. Toh, P. T. Lee, C. Salter, C. Johnston and R. G. Compton, *ChemistryOpen*, 2014,**4**, 22-26.
11. Y. Wang, K. R. Ward, E. Laborda, C. Salter, A. Crossley, R. M. Jacobs and R. G. Compton, *Small*, 2013, **9**, 478-486.
12. Y. Wang, E. Laborda, K. Tschulik, C. Damm, A. Molina and R. G. Compton, *Nanoscale*, 2014, **6**, 11024-11030.

13. E. J. Stuart, K. Tschulik, C. Batchelor-McAuley and R. G. Compton, *ACS Nano*, 2014, **8**, 7648-7654.

14. A. J. Bard, H. Zhou and S. J. Kwon, *Israel Journal of Chemistry*, 2010, **50**, 267-276.

15. Y. X. Li, J. T. Cox and B. Zhang, *Journal of the American Chemical Society*, 2010, **132**, 3047-3054.

16. J. H. Park, S. N. Thorgaard, B. Zhang and A. J. Bard, *Journal of the American Chemical Society*, 2013, **135**, 5258-5261.

17. D. Wakerley, A. G. Güell, L. A. Hutton, T. S. Miller, A. J. Bard and J. V. Macpherson, *Chemical Communications*, 2013, **49**, 5657-5659.

18. R. Dasari, D. A. Robinson and K. J. Stevenson, *Journal of the American Chemical Society*, 2013, **135**, 570-573.

19. S. E. Fosdick, M. J. Anderson, E. G. Nettleton and R. M. Crooks, *Journal of the American Chemical Society*, 2013, **135**, 5994-5997.

20. J. M. Kahk, N. V. Rees, J. Pillay, R. Tshikhudo, S. Vilakazi and R. G. Compton, *Nano Today*, 2012, **7**, 174-179.

21. Y. G. Zhou, N. V. Rees and R. G. Compton, *Angewandte Chemie International Edition*, 2011, **50**, 4219-4221.

22. Y. G. Zhou, E. J. Stuart, J. Pillay, S. Vilakazi, R. Tshikhudo, N. V. Rees and R. G. Compton, *Chemical Physics Letters*, 2012, **551**, 68-71.

23. K. Tschulik, B. Haddou, D. Omanović, N. V. Rees and R. G. Compton, *Nano Research*, 2013, **6**, 836-841.

24. W. Cheng and R. G. Compton, *Trends in Analytical Chemistry*, 2014, **58**, 79-89.

25. W. Cheng and R. G. Compton, *Angewandte Chemie International Edition*, 2014, **53**, 13928-13930.

26. O. P. Sharma and T. K. Bhat, *Food Chemistry*, 2009, **113**, 1202-1205.

27. V. Andrei, A. I. Bunea, A. Tudorache, S. Gáspár and A. Vasilescu, *Electroanalysis*, 2014, **26**, 2677-2685.

28. L. L. Mensor, F. S. Menezes, G. G. Leitão, A. S. Reis, T. C. d. Santos, C. S. Coube and S. G. Leitão, *Phytotherapy Research*, 2001, **15**, 127-130.

29. W. Brand-Williams, M. Cuvelier and C. Berset, *LWT-Food Science and Technology*, 1995, **28**, 25-30.

30. B. Yang, M. Zhao, J. Shi, N. Yang and Y. Jiang, *Food Chemistry*, 2008, **106**, 685-690.

31. S. Milardovic, D. Iveković, V. Rumenjak and B. S. Grabarić, *Electroanalysis*, 2005, **17**, 1847-1853.

32. E. Solon and A. J. Bard, *Journal of the American Chemical Society*, 1964, **86**, 1926-1928.

33. G. M. Abouelenien, *Journal of Electroanalytical Chemistry*, 1993, **345**, 303-321.

34. A. W. Taylor, S. Puttick and P. Licence, *Journal of the American Chemical Society*, 2012, **134**, 15636-15639.

35. O. Chen, J. Zhuang, F. Guzzetta, J. Lynch, A. Angerhofer and Y. C. Cao, *Journal of the American Chemical Society*, 2009, **131**, 12542-12543.

36. D. Horn and J. Rieger, *Angewandte Chemie International Edition*, 2001, **40**, 4331-4361.

37. E. Stuart, K. Tschulik, D. Omanović, J. T. Cullen, K. Jurkschat, A. Crossley and R. G. Compton, *Nanotechnology*, 2013, **24**, 444002-444009.

38. T. Yamaguchi, H. Takamura, T. Matoba and J. Terao, *Bioscience, Biotechnology, and Biochemistry*, 1998, **62**, 1201-1204.

39. N. D. Yordanov and A. G. Christova, *Fresenius' Journal of Analytical Chemistry*, 1997, **358**, 610-613.

40. M. S. Alger, *Polymer Science Dictionary*, Springer Science & Business Media, 1997.

41. J. F. Arteaga, M. Ruiz-Montoya, A. Palma, G. Alonso-Garrido, S. Pintado and J. M. Rodriguez-Mellado, *Molecules*, 2012, **17**, 5126-5138.

42. R. Vittal, K.-J. Kim, H. Gomathi and V. Yegnaraman, *The Journal of Physical Chemistry B*, 2008, **112**, 1149-1156.

43. A. M. Bond, F. Marken, E. Hill, R. G. Compton and H. Hügel, *Journal of the Chemical Society, Perkin Transactions 2*, 1997, 1735-1742.

44. K. Naoi, M. M. Lien and W. H. Smyrl, *Journal of Electroanalytical Chemistry*, 1989, **272**, 273-275.

45. T. J. Davies, C. E. Banks and R. G. Compton, *Journal of Solid State Electrochemistry*, 2005, **9**, 797-808.

46. Y. G. Zhou, F. W. Campbell, S. R. Belding and R. G. Compton, *Chemical Physics Letters*, 2010, **497**, 200-204.

47. W. Cheng, C. Batchelor-McAuley and R. G. Compton, *ChemElectroChem*, 2014, **1**, 714-717.

Chapter 8

Ion Insertion into Individual 7,7,8,8-Tetracyanoquinodimethane (TCNQ) Nanoparticles

In the previous chapters, we used the nano-impacts method to study the electrochemical sizing, the extent of doping and the electron transfer kinetics of organic nanoparticles during their reduction or/and oxidation. In this chapter, we investigate the quantification of *partial* ion insertion into *individual* 7,7,8,8-Tetracyanoquinodimethane (TCNQ) nanoparticles. The study shows that both potassium and sodium ions can be inserted into single TCNQ nanoparticles from aqueous solution. The extent of both potassium and sodium insertion into individual nanoparticles is quantitatively measured and shown to be partial and that the sodium ion shows a higher extent of insertion. The insertion process is inferred to be limited and controlled by the formation of a thin shell of salt, Na^+/K^+ $TCNQ^{\cdot -}$ formed at the surface of the nanoparticle. This work presented herein was published in *Nanoscale* 7.38 (2015), 15719-15726.

8.1 Introduction

Ion extraction and insertion is a central process in energy transformation using batteries and fuel cells. The improved electron/ion transport due to the superior contact between electrolyte solutions makes micro/nanostructures and nanoparticles attractive as electrode materials for lithium or sodium ion batteries[1, 2]. Studying the extraction and insertion of ions is challenging, because the charge transfer is strongly coupled to mass transport processes which typically can only be approximately quantified when using an ensemble of nanoparticles supported on an electrode surface. To date, the real-time characterisation and quantification of ion insertion into single nanoparticles has not been possible[3] although currently there are rapidly increasing applications using nanostructured/ nanoparticles anodes for excellent lithium ion storage[4, 5].

As concern rises for the toxicity and limited natural resources of lithium, sodium or potassium ion batteries (SIBs or KLBs) as an alternative to lithium ions batteries have recently attracted significant attention [6, 7]. However, the mechanism of Na or K ion transport into nanostructured materials at nanoscale has been rarely experimentally explored. The quantitative analysis of such ion insertion is important to understand the underlying mechanism of different cations insertion[8] and to the rational design of intermolecular structures of electrodes for ideal battery performance[9].

The method of "Nano-impacts", introduced in Section 2.4 and discussed through at the whole thesis, can induce oxidation/reduction of, or catalytic reaction by, the nanoparticle[10-20]. Previous chapters gave some detailed examples of nano-impact experiments in the applications of electrochemical sizing, the quantificaiton of doping of

polymerical NPs and the electron transfer kinetics of ensembles. In this chapter, using 7,7′,8,8′-tetracyanoquinodimethane(TCNQ) nanoparticles in aqueous solution as a model, we explore ion insertion into single nanoparticles. The quantification of the cation insertion at single nanoparticle level is established and a limiting mechanism proposed. Figure 8.1 shows the stucture of a TCNQ molecule.

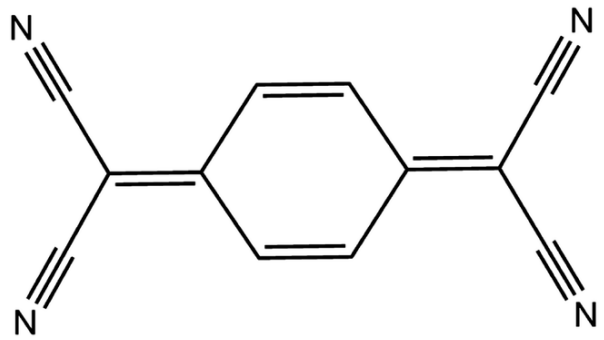


Figure 8.1 The structure of a TCNQ molecule

TCNQ is a well-known organic charge-transfer salt that has a well-defined quasi-one-dimensional structure with a high electronic conductivity[21] and has been recently used as a new organic nanomaterials-based electrode[18] which builds on traditional inorganic nanomaterials for possible future large-scale applications[9, 22]. TCNQ has previously been characterised by modifying the electrode with the ensemble of TCNQ microcrystals immobilised on an electrode surface[23, 24] or studying the chemical reactions occurring in TCNQ micro/nanoparticles[25, 26]. In this chapter, the potassium and sodium insertion into single TCNQ nanoparticles has been quantitatively analysed at single nanoparticle level, showing a higher extent of insertion for sodium ions, and a thin layer limiting mechanism was proposed with the formation of a thin shell of salt, Na^+/K^+ $TCNQ^{\bullet -}$ formed on the

surface of the nanoparticle, whilst the thickness of shell is independent on the nanoparticle size but does reflect the cation type.

8.2 Experimental

8.2.1 Chemicals and Materials

7,7,8,8-Tetracyanoquinodimethane (TCNQ, 98%) was purchased from Sigma-Aldrich. Dimethyl sulfoxide (DMSO, ≥99.7%) was obtained from Fisher Scientific and used as received. The phosphate buffer solution (pH = 6.8) containing only K^+ was composed of 50 mM monobasic and dibasic potassium phosphates; 0.1 M KCl used as further supporting electrolyte. The phosphate buffer solution (pH = 6.8) containing only Na^+ was composed of 50 mM monobasic and dibasic sodium phosphates; 0.1 M NaCl was again used as further supporting electrolyte. All solutions were made up with deionised water of resistivity not less than 18.2 MΩ cm (Millipore) at 298 K and degassed with nitrogen (oxygen-free, BOC Gases plc) before use.

8.2.2 Synthesis of TCNQ Nanoparticles

TCNQ nanoparticles were synthesised using the reprecipitation method[27] as detailed in Section 2.1. To prepare different sizes of nanoparticles, 5 mM or 10 mM TCNQ/DMSO solutions were added into 10 mL deionised water respectively under vigorously stirring by magnetic vortexing at 800 rpm. Both of the nanoparticles suspensions were subjected to sonication for 10 min a temperature of 25℃, resulting transparent yellow dispersions with the appearance of TCNQ nanoparticle solutions.

8.2.3 Characterisation of TCNQ Nanoparticles

8.2.3.1 DLS measurements of TCNQ Nanoparticles

Dynamic light scattering (DLS, Malvern Instruments Ltd, UK) measurements were performed to characterize the size distribution of the synthesised TCNQ nanoparticles. DLS measurements were detailed in Section 3.2.3.

8.2.3.2 SEM measurements of TCNQ Nanoparticles

Scanning electron microscopy (SEM) was performed by Dr. Chris Salter. It was carried out on a glassy carbon wafer with a Jeol 6480L SEM (Jeol, Japan) to study the shape and size of the TCNQ particles dispersed in Milli-Q water (100 times diluted from the stock suspension).Image J (Version 1.38) was used to analyse the nanoparticle size determined via SEM.

8.2.4 Cyclic Voltammetry of TCNQ Nanoparticles

The electrochemical experiments were conducted at 25℃ with the same instrumentation as detailed in Section 3.2.4. For cyclic voltammetry measurements, a glassy carbon macroelectrode (GC, diameter 3.0 mm) was used as the working electrode, saturated calomel electrode (SCE) as the reference electrode while a carbon rod acted as the counter electrode. The GC macroelectrode was modified by dropping varying amounts of the TCNQ NPs suspension onto the surface and letting the electrode dry under nitrogen.

Cyclic voltammetry was conducted at a scan rate of 50 mV/s in 0.1 M K^+ or Na^+ PBS buffer, 0.1 M KCl, 0.1 M NaCl and 0.1 M HCl. All solutions were degassed thoroughly with nitrogen before scanning. Working electrode was polished with three grades of diamond spray (3, 1 and 0.1 microns) before sonication in water and drying with nitrogen prior to each scan.

8.2.5 Ion Insertion into Single TCNQ Nanoparticles

The method of "nano-impacts" was introduced in Section 2.4. For the electrochemical study of single TCNQ nanoparticles, chronoamperometry was performed with a carbon microelectrode (diameter = 10 μm) as the working electrode and the same reference and counter electrodes as in Section 8.2.3. The carbon microelectrode was calibrated in the same way as shown in Section 3.2.5. The impact experiments was conducted in 0.1 M PBS buffer with a known concentration of TCNQ nanoparticles solution (32 pM) added. GPES was employed to perform the chrnoamperometry. Software "Signal Counter" was used for analysis of the impact spikes observed and OriginPro2015 for statistical analysis of the charge passed per spike.

8.3 Results and Discussion

In this section, characterisations of TCNQ nanoparticles are made using DLS and SEM techniques to establish their size and shape. Cyclic voltammetry is then conducted to study the electrochemical behaviour of ensembles of TCNQ nanoparticles on electrodes in 0.1 M K^+ or Na^+ PBS buffer, 0.1 M KCl, 0.1 M NaCl and 0.1 M HCl solutions. The reductive potentials are found dependently on the cation insert from the solution. Then, the

quantification of cations insertion into *single* TCNQ nanoparticles is studied by using the "nano-impacts" method. Quantitative analysis shows that for both potassium and sodium ion insertion into individual TCNQ nanoparticles is partial and sodium ion has a higher extent of insertion, forming a thin shell of salt at the surface of the nanoparticles.

8.3.1 DLS measurements of TCNQ Nanoparticles

Two sizes of TCNQ nanoparticles were synthesised using the reprecipitation method[29] as introduced in Section 8.2.2. DLS measurements were used to detect the size of TCNQ nanoparticles in aqueous solution, giving mean diameters of 116 nm and 71nm for the large and small TCNQ nanoparticles respectively (Figure 8.2).

8.3.2 SEM measurements of TCNQ Nanoparticles

To further characterize the shape and double confirm the size of TCNQ nanoparticles, SEM was carried out on a glassy carbon wafer showing that the TCNQ nanoparticles are spherical and giving mean size of 124 ± 38 nm for the large TCNQ nanoparticles and 76 ± 20 nm for the small TCNQ nanoparticles (Figure 8.3), which are similar to those from DLS estimation.

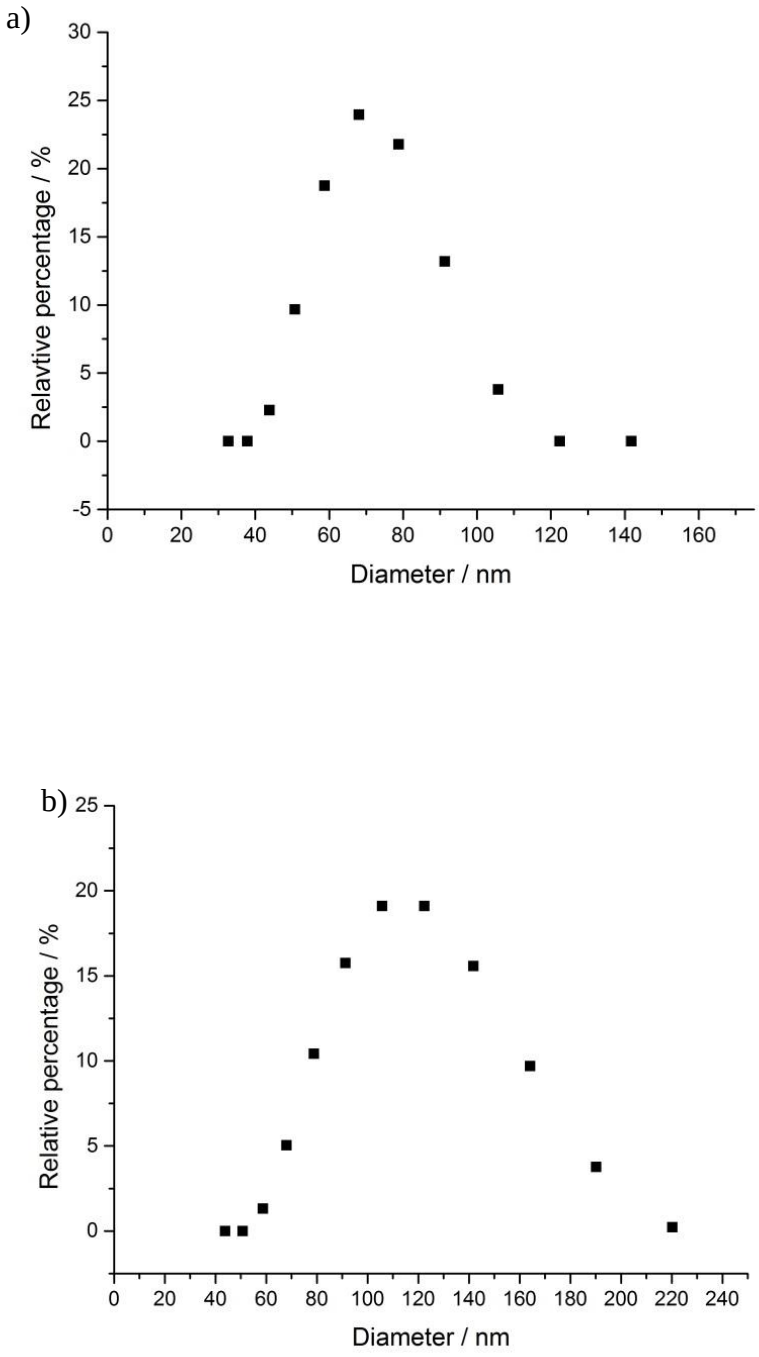
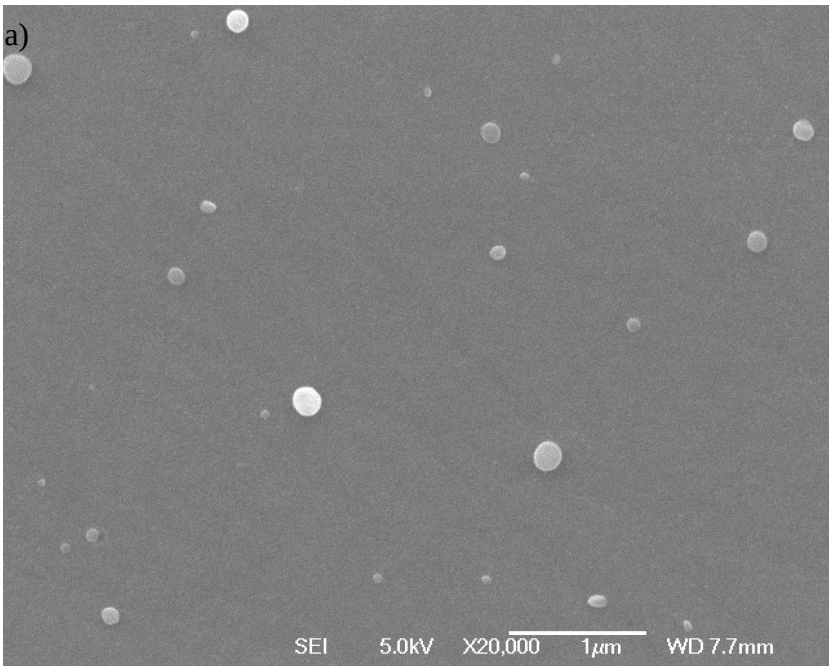


Figure 8.2 Size distribution of the synthesised (a) small TCNQ nanoparticles and (b) large TCNQ nanoparticles measured via DLS analysis.



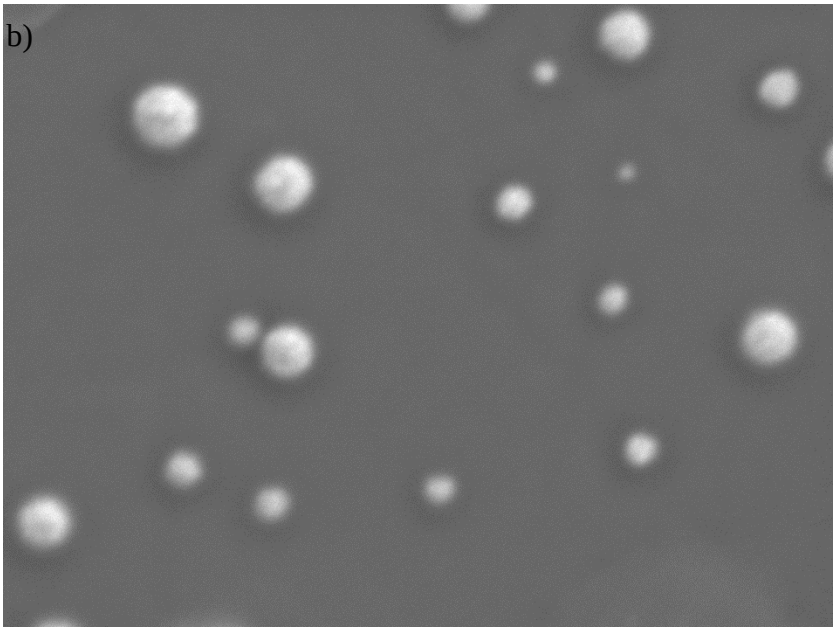


Figure 8.3 SEM images of the TCNQ nanoparticles synthesised by the reprecipitation method

8.3.3 Cyclic Voltammograms of Ensembles of TCNQ Nanoparticles

Before studying single TCNQ nanoparticles, the electrochemical behaviour of ensembles of TCNQ nanoparticles were investigated. First, a macro glassy carbon (GC) electrode (diameter = 3 mm) was modified with different amounts of TCNQ nanoparticles and cyclic voltammograms recorded. Figure 8.4 shows the cyclic voltammograms recorded for a glassy carbon macroelectrode modified with various loadings of TCNQ nanoparticles of two sizes immersed in phosphate buffered saline (PBS) buffer (pH = 6.8) containing either only K^+ as cation (K^+ buffer), or only Na^+ as cation (Na^+ buffer). In K^+ buffer, a reduction peak potential at -0.03 V and an oxidation peak potential at +0.25 V versus the saturated calomel reference electrode (SCE) likely correspond to one-electron transfer between TCNQ and $TCNQ^{\cdot-}$ as shown in Equation 8.1:

$$K^+ + TCNQ + e^- \rightleftharpoons K^+ TCNQ^{\cdot-} \qquad \text{(Eqn 8.1)}$$

consistent with previous literature[28, 29]. An inert zone exists which is characteristic of ion insertion between the two peaks also observed in Na^+ buffer with a reduction peak potential at -0.05 V and oxidation peak potential at +0.28 V, corresponding to the reaction as given in Equation 8.2:

$$Na^+ + TCNQ + e^- \rightleftharpoons Na^+ TCNQ^{\cdot-} \qquad \text{(Eqn 8.2)}$$

The voltammetric peaks decay when the potential is cycled (Figure 8.5), which are partly due to the partial dissolution of K+/Na+ TCNQ·-, or chemically reversible process of

oxidation from TCNQ·- back to TCNQ may not be complete during the first cycle. The reductive charge is therefore estimated from the reduction peak of the first scans for all loadings of TCNQ nanoparticles. The peak charge (obtained from the integration of the peak area from Figure 8.4) was found to linearly increase with the TCNQ nanoparticle loadings on the electrode surface (Figure 8.6), and the total reductive charge likely reflect the state of agglomeration/aggregation of nanoparticles where only the nanoparticles at the periphery of the aggregated particles that are in contact with the electrode are reduced[30], and the overlapping of adjacent diffusion layers[31], as well as the charge insertion into individual TCNQ nanoparticles.

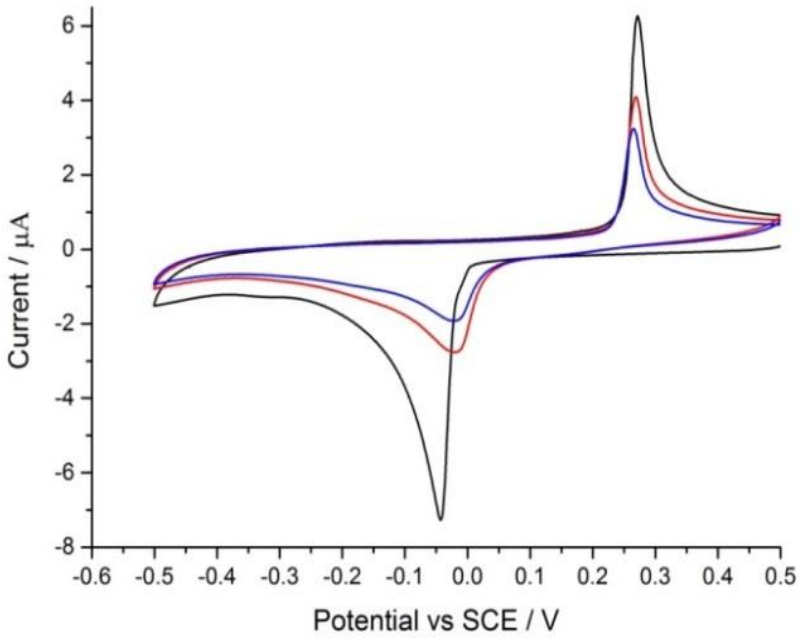


Figure 8.5 Cyclic voltammograms recorded for a glassy carbon macroelectrode modified with TCNQ nanoparticles (monomer mole: 2×10^{-10} mol) in 0.1 M PBS buffer (pH = 6.8) at a scan rate of 50 mV/s (black: first scan; red: second scan; blue: third scan).

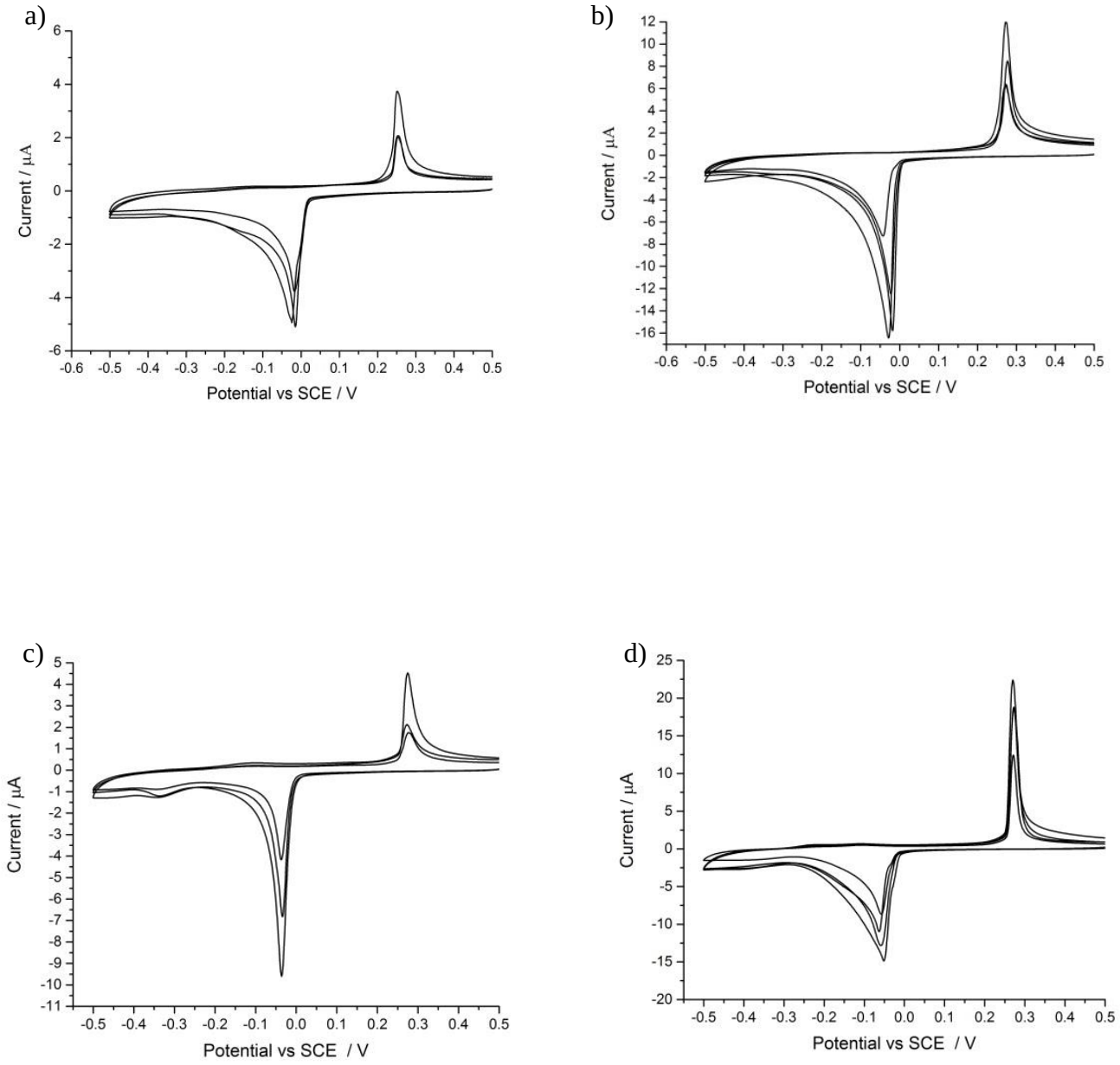


Figure 8.4 Cyclic voltammograms (the first cycle) recorded for a glassy carbon macroelectrode modified with various loading of TCNQ nanoparticles of two sizes in 0.1 M PBS buffer solution containing only K^+ or Na^+ as cation at a scan rate of 50 mV/s: (a) various amounts of 71 nm TCNQ nanoparticles (monomer moles): 1×10^{-10} mol, 1.5×10^{-10} mol, 2×10^{-10} mol in K^+ buffer (b) various amounts of 116 nm TCNQ nanoparticles (monomer moles): 2×10^{-10} mol, 3×10^{-10} mol, 4×10^{-10} mol, 5×10^{-10} mol in K^+ buffer (c) various amount of 71 nm TCNQ nanoparticles (monomer moles): 2×10^{-10} mol, 3×10^{-10} mol, 4×10^{-10} mol in Na^+ buffer (d) various amount of 116 nm TCNQ nanoparticles (monomer moles): 2×10^{-10} mol, 3×10^{-10} mol, 4×10^{-10} mol, 5×10^{-10} mol in Na^+ buffer.

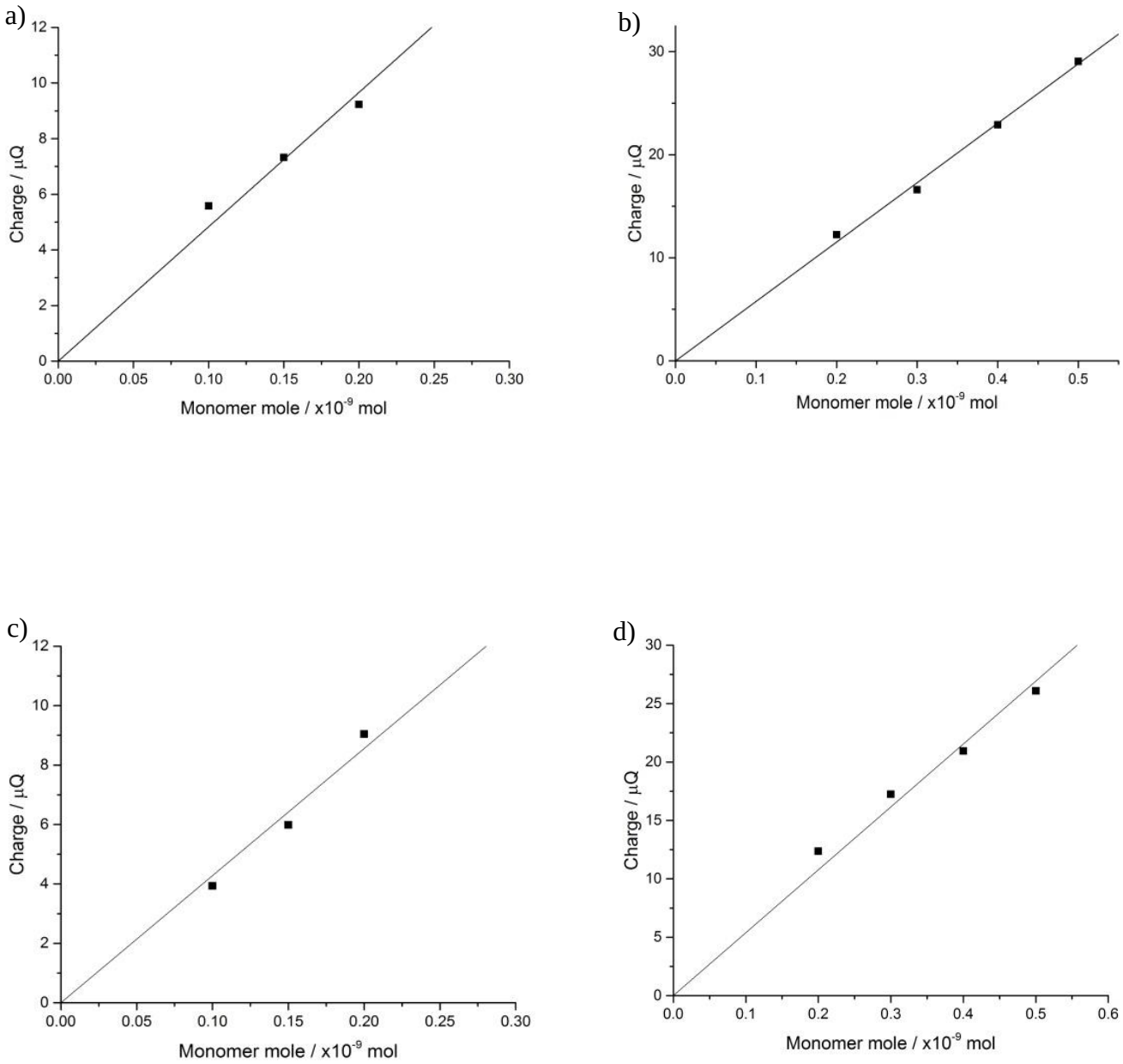


Figure 8.6 Linear relation between the cathodic peak charges (obtained from the integration of the peak area from Figure 8.4) and the TCNQ nanoparticle loadings on the electrode surface (a) 71 nm TCNQ nanoparticles modified electrode in K^+ buffer (b) 116 nm TCNQ nanoparticles modified electrode in K^+ buffer (c) 71 nm TCNQ nanoparticles modified electrode in Na^+ buffer (d) 116 nm TCNQ nanoparticles modified electrode in Na^+ buffer.

Cyclic voltammograms of TCNQ nanoparticles modified GC electrode were also conducted in hydrochloric acid, sodium chloride, and potassium chloride as shown in Figure 8.7. The reduction of TCNQ nanoparticles shows a chemically reversible process in 0.1 M KCl, with a reduction peak potential seen at -0.03 V. The voltammogram is similar to that observed in 0.1 M PBS buffer only containing K^+ as cation. A similar chemically reversible process was also recorded in 0.1 M NaCl with a reduction peak potential at -0.05 V and similar voltammogram to 0.1 M PBS buffer containing only Na^+ as cation. The reduction of TCNQ nanoparticles in both 0.1 M KCl and 0.1 M NaCl are in contrast to that in 0.1 M HCl, where the reduction peak was not seen with the potential range from -0.5 V to 0.5 V, indicating that potassium or sodium ions insertion was accompanied by the reduction of TCNQ nanoparticles as shown in Scheme 8.1.

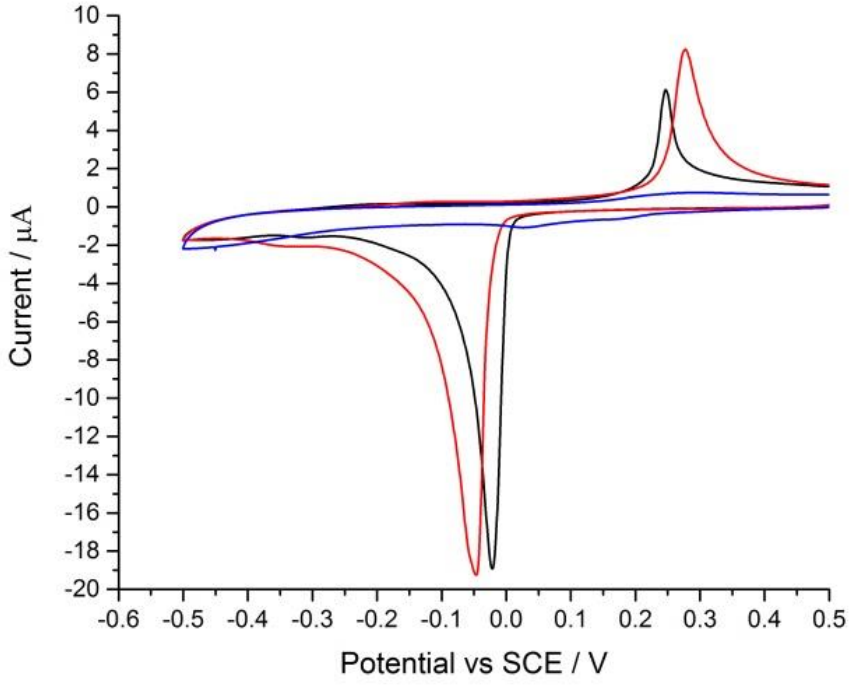
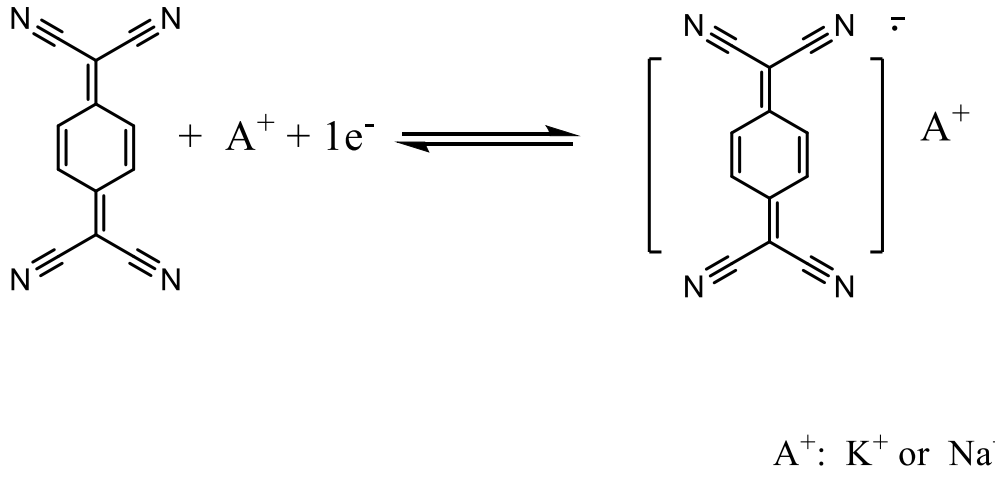


Figure 8.7 Cyclic voltammograms recorded for a glassy carbon macroelectrode modified with 4×10^{-10} mol (monomer mole) TCNQ nanoparticles (diameter: 116 nm) in 0.1 M KCl (black), 0.1 M NaCl (red) and 0.1 M HCl (blue) at a scan rate of 50 mV/s



Scheme 8.1 Potassium or sodium ions insertion into TCNQ nanoparticles during their reduction

8.3.4 Nano-impacts of individual TCNQ nanoparticles

To study the reduction of individual TCNQ nanoparticles, a carbon microelectrode was immersed in a PBS buffer (pH = 6.8) solution containing either only K^+ or Na^+ as cation (other than protons) and known concentrations of a TCNQ nanoparticle suspension (32 pM) added. The reduction potential was selected to be -0.3 V for chronoamperometric measurements of individual TCNQ nanoparticle collisions with the electrode, as recorded by current spikes in the current-time response, with each spike representing a single impact, as shown in Figure 8.8.

No reductive spikes at potentials of 0 V or more positive were observed, suggesting the monitored spikes only correspond to potassium or sodium insertion accompanying Faradaic reduction of TCNQ nanoparticles. Another control experiment was conducted at

the potential of -0.30 V with no TCNQ nanoparticles in the solution and again no spikes were detected, further suggesting that the occurrence of reductive spikes is due to the random collisions of TCNQ nanoparticles with the electrode. The charge from ion insertion into individual TCNQ nanoparticles was then calculated by integrating the area of each spike as shown in Figure 8.9.

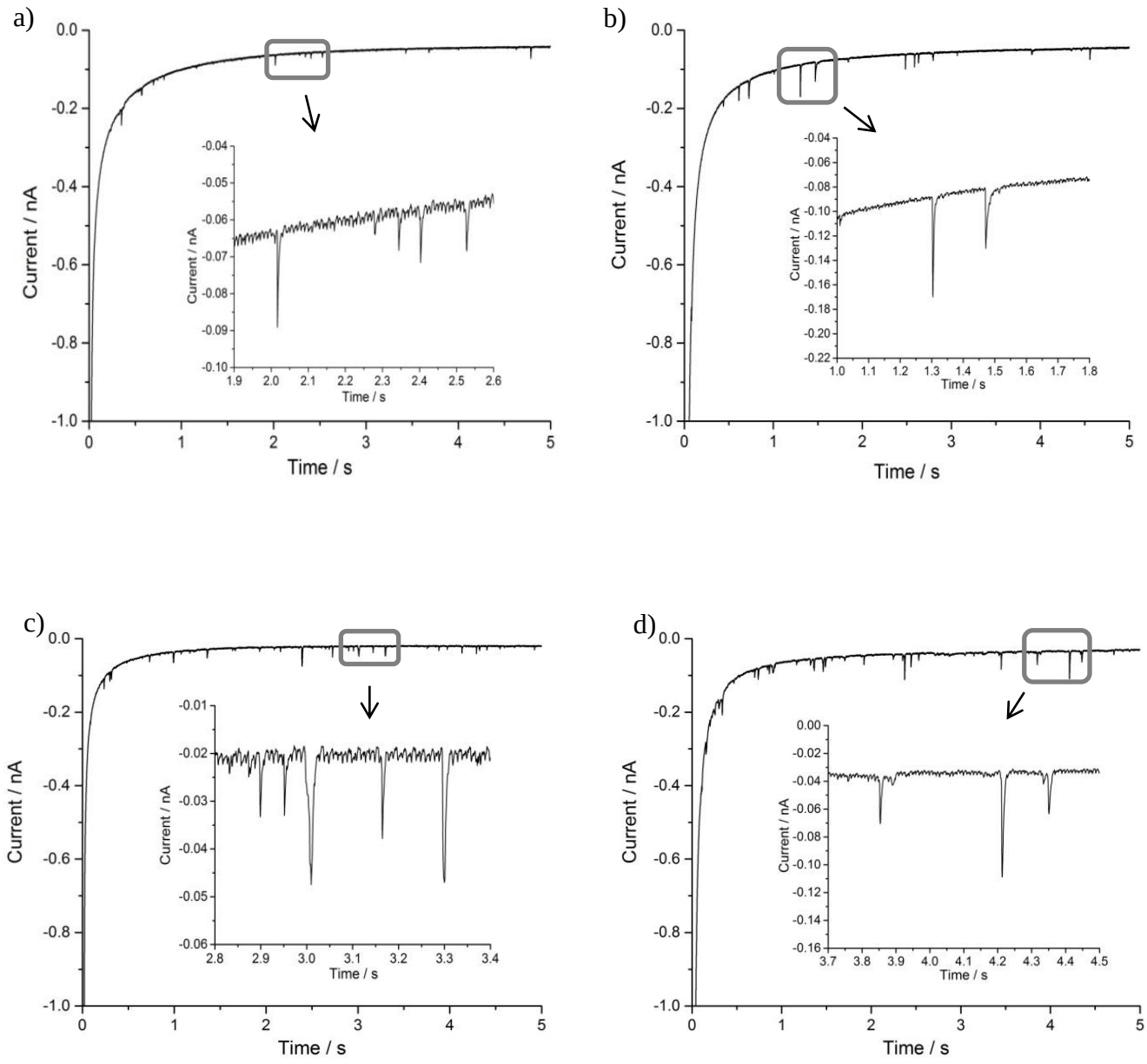


Figure 8.8 Chronoamperometric profiles showing reductive Faradaic spikes of (a) 71nm and (b) 116nm TCNQ nanoparticles at -0.30 V vs. SCE. in K^+ PBS buffer (pH = 6.8), and (c) 71nm and (d) 116nm TCNQ nanoparticles at -0.30 V vs. SCE. in Na^+ PBS buffer (pH = 6.8). The inset showing the detailed impact spikes.

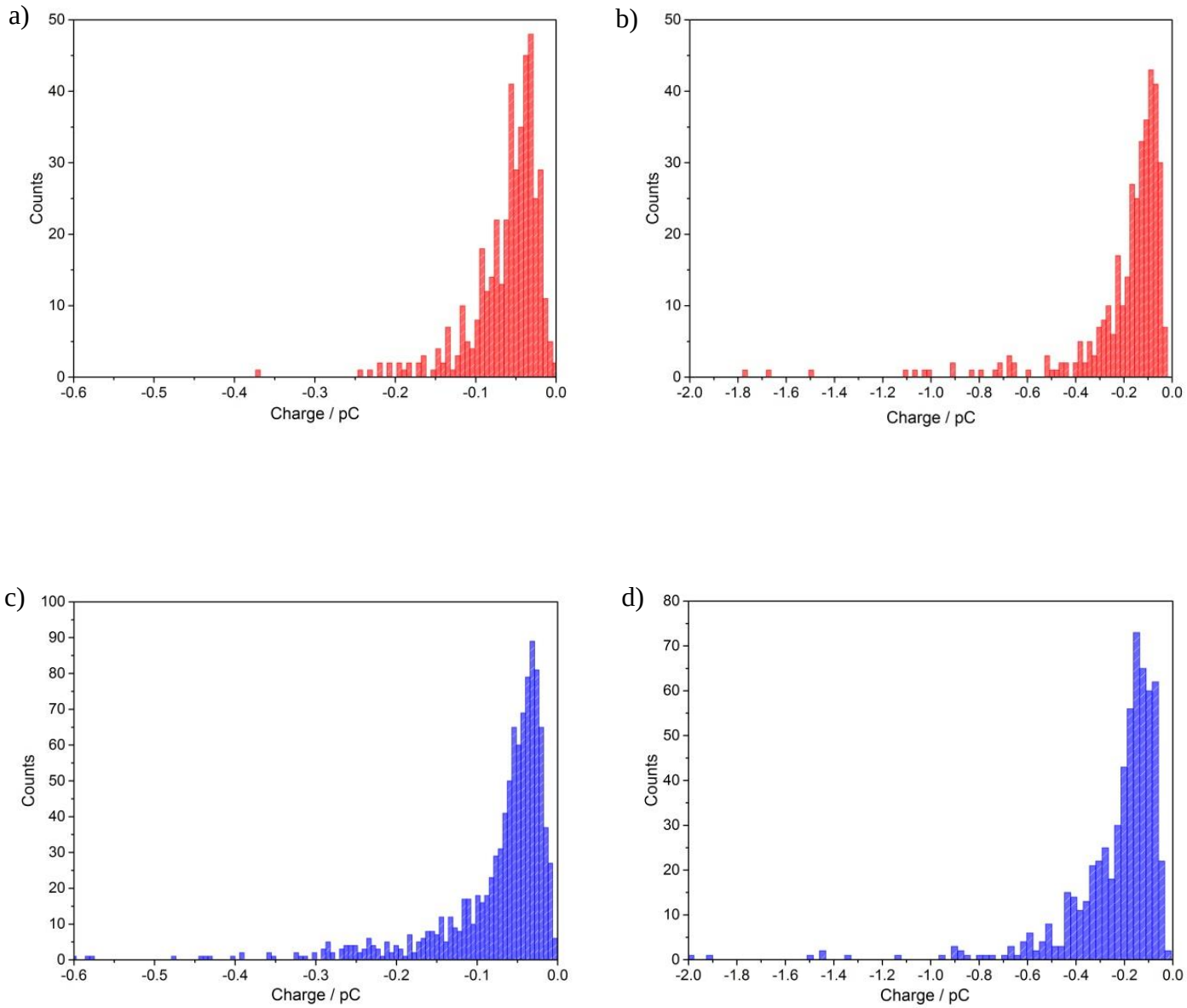


Figure 8.9 Histograms of the reductive charge resulting from ion insertion into individual TCNQ nanoparticles in PBS buffer (pH = 6.8) at -0.30 V vs. SCE. (a) 71 nm nanoparticles in K^+ PBS buffer (pH = 6.8), with average charge Q_{K1} = 6.10 ×10^{-14} C from 433 individual spikes; (b) 116 nm nanoparticles in K^+ PBS buffer (pH = 6.8), with average charge Q_{K2} = 1.96 ×10^{-13} C from 360 individual spikes; (c) 71 nm nanoparticles in Na^+ PBS buffer (pH = 6.8), with average charge Q_{Na1} = 7.71 ×10^{-14} C from 1019 individual spikes; (d) 116 nm nanoparticles in Na^+ PBS buffer (pH = 6.8), with average charge Q_{Na2} = 2.38 ×10^{-13} C from 605 individual spikes.

8.3.5 Quantification of Potassium and Sodium Insertion into Individual TCNQ Nanoparticles

To quantify ion insertion into TCNQ nanoparticles, the mean diameters (D_{np}) of the two batches of TCNQ nanoparticles was estimated to be 71 nm and 116 nm through dynamic light scattering (Figure 8.2). If the charge is passed as a result of complete (100%) ion insertion of single TCNQ nanoparticles, then the ideal charge (Q_i) of electron transfer from ion insertion of single TCNQ nanoparticles can be determined by Equation 8.3 given that TCNQ nanoparticles formed via reprecipitation are spherical (see Figure 8.3).

$$Q_i = \frac{D_{np}^3 nF\pi\rho}{6M} \quad \text{(Eqn 8.3)}$$

where D_{np} is the diameter of TCNQ nanoparticles, M is the molar mass of TCNQ, ρ is the density of TCNQ and F is the Faraday constant. The parameter n is the number of electrons transferred per molecule during ion insertion into nanoparticles, where n = 1 for TCNQ reduction to $TCNQ^{\cdot-}$. Note that microcrystals of TCNQ formed via solvent evaporation have quite different shapes[23, 24, 28].

By comparing the average reductive charge Q_r resulting from ion insertion into all the measured individual TCNQ nanoparticles (Figure 8.9) with a diameter of 71 nm or 116 nm from experimental nano-impacts against the ideal charge Q_i assuming the complete ion insertion (Q_{i1} = 1.24×10^{-13} C for single 71 nm TCNQ nanoparticles or Q_{i2} = 5.48×10^{-13} C for single 116 nm TCNQ nanoparticles, according to Equation 8.3), the yield of ion insertion into single TCNQ nanoparticle ($y=Q_r/Q_i$) can be determined. Specifically, as for

potassium insertion into single TCNQ nanoparticles of 71 nm, we calculated the average charge resulting from all individual spikes to be 6.10 $\times 10^{-14}$ C (Figure 8.9(a)), and the potassium insertion yield to be 49%. Then the value of yield observed at -0.2 V as at −0.3 V was found to be same to each other as shown in Figure 8.10. Thus the charge is potential-independent, suggesting that a maximum yield of ion insertion is realised.

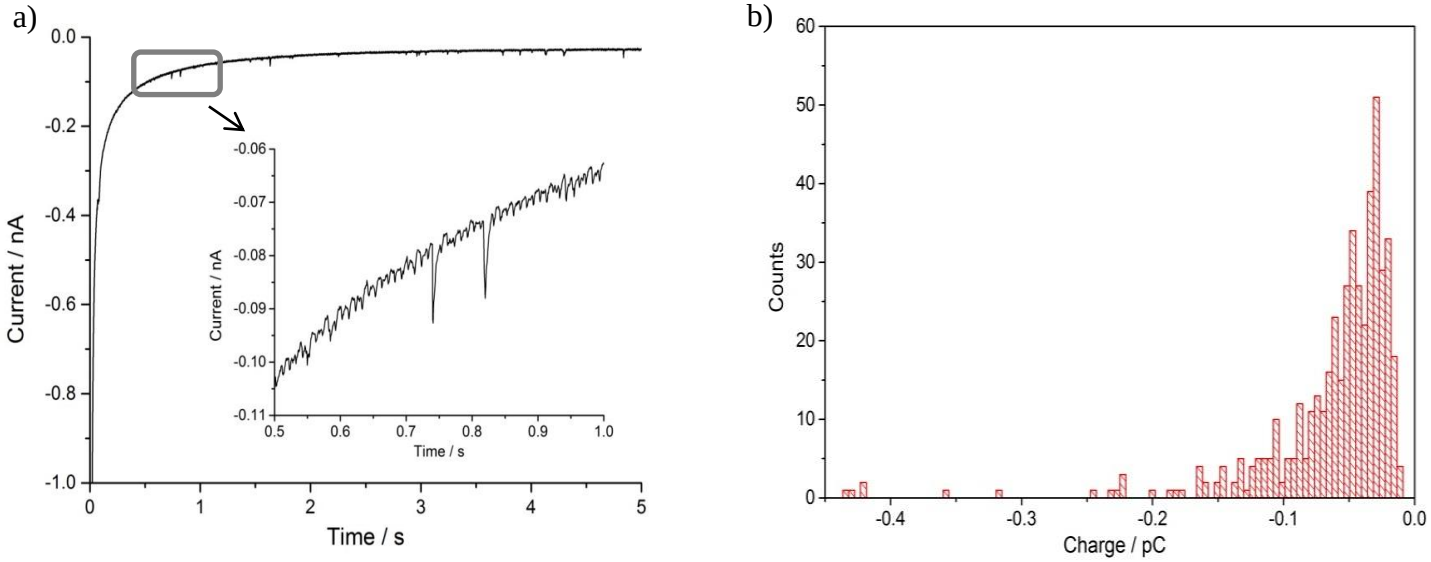


Figure 8.10 (a) Chronoamperometric profiles showing reductive Faradaic spikes of TCNQ nanoparticles (71 nm) in K^+ PBS buffer (pH = 6.8) at -0.20 V vs. SCE. The inset showing the detailed impact spikes. (b) Histograms showing the TCNQ nanoparticles completed reductive charge in PBS buffer (pH = 6.8) at potentials of -0.20 V.

Further, considering there is a size distribution of TCNQ nanoparticles, the distributions of charge from ion insertion into a single nanoparticle of both 71 nm and 116 nm TCNQ NPs (Figure 8.11) were plotted for both potassium and sodium insertion. We found there were good agreements between the distribution of charge from ion insertion into a single nanoparticle, as analysed for single TCNQ nanoparticles and the theoretical estimation, although some discrepancy is seen for large particles. This is because large nanoparticles

have a lower diffusion coefficient, which leads to a lower probability of observing impacts[32].

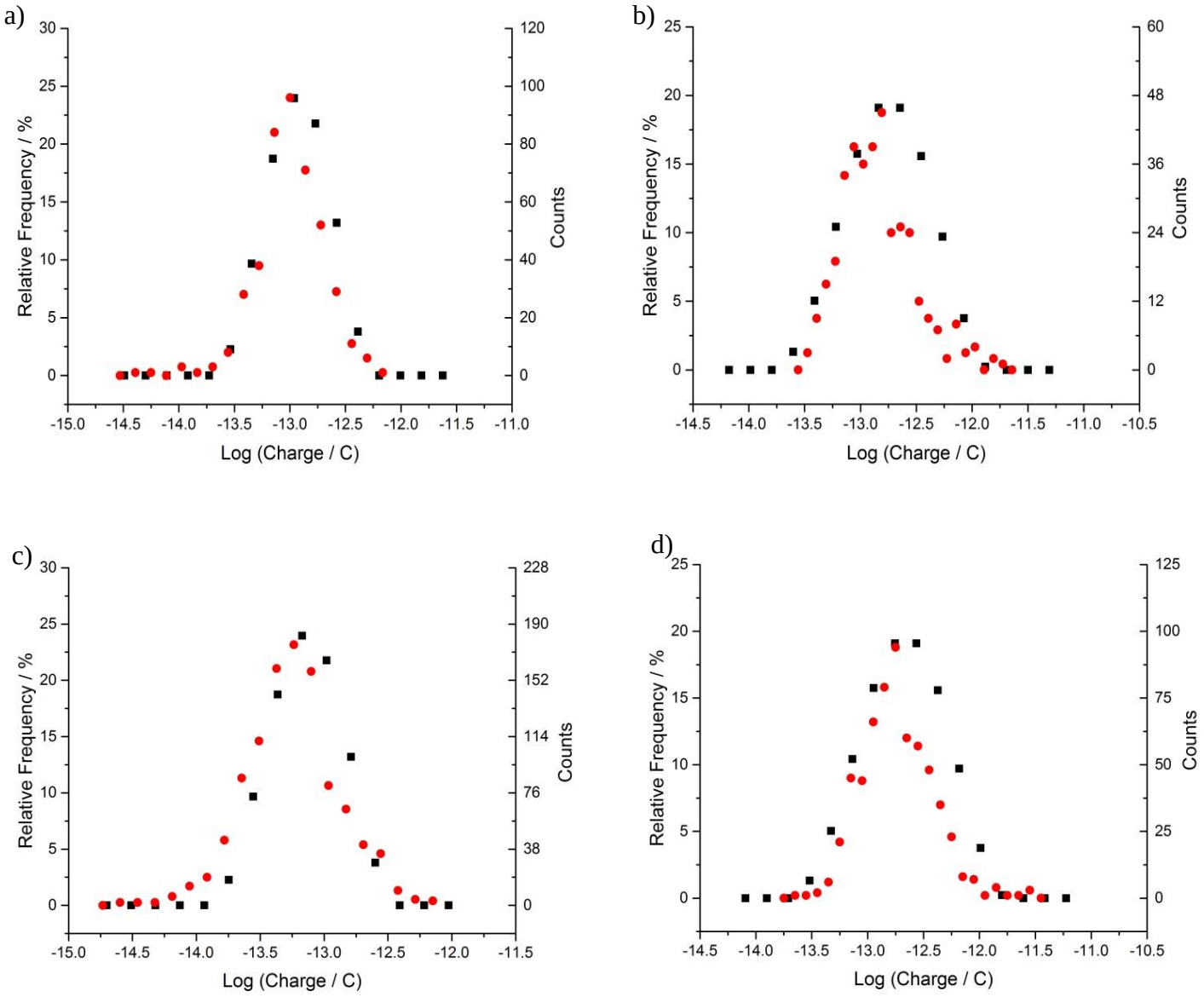


Figure 8.11 Histogram showing the log normal distribution of the reductive charge resulting from potassium or sodium ion insertion into single TCNQ nanoparticle calculated from nano-impact experiments (red dots), and the theoretical estimation (black dots), assuming the potassium insertion yield (y_K) in K^+ PBS buffer is (a) 49% for 71 nm NPs, (b) 36% for 116 nm NPs; and sodium insertion yield (y_{Na}) in Na^+ PBS buffer is (c) 62% for 71 nm NPs, (d) 43% for 116 nm NPs.

The yield of ion insertion into single TCNQ nanoparticle (y) is estimated as 49% (y_{K1}), and 36% (y_{K2}), respectively for potassium insertion into 71 nm and 116 nm TCNQ NPs, and 62% (y_{Na1}), and 43% (y_{Na2}), respectively for sodium insertion into 71 nm and 116 nm TCNQ NPs (the yield values were derived according to Equation 8.3). To our knowledge, this is the first time that the quantitative determination of the extent of cation insertion at the single nanoparticle level has been demonstrated. The charge injection into individual nanoparticles is similar to that of TCNQ nanoparticles immobilised on the electrode, where the ratio of charge from partial reduction of TCNQ is 60% and 50%, in K^+ PBS buffer, 56% and 45% in Na^+ PBS buffer, respectively for 71 nm and 116 nm, and may be limited by short impact times as shown in Figure 8.12

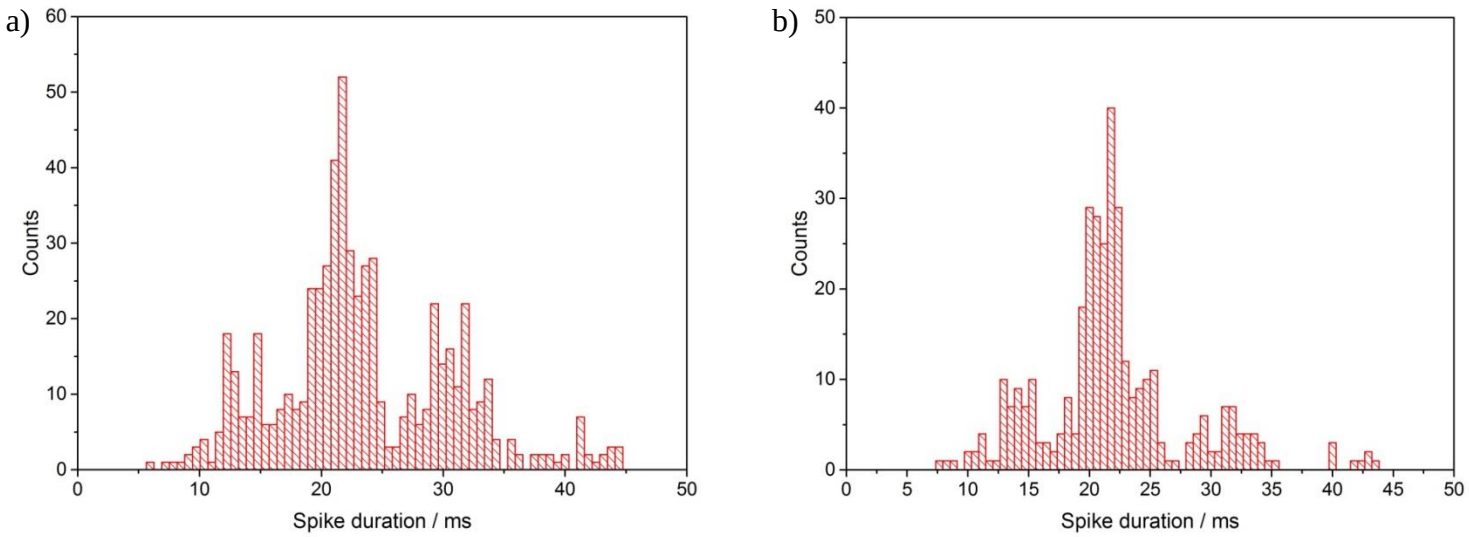


Figure 8.12 Histograms showing the duration of impact time from ion insertion of single TCNQ nanoparticles (116 nm) in (a) Na^+ PBS buffer (pH = 6.8) and (b) K^+ PBS buffer (pH = 6.8) at a potential of -0.30 V.

As can be seen from Figure 8.9, the resulting charge from potassium or sodium insertion into single nanoparticles increases with particle size, corresponding to current spikes of

higher amplitudes ($Q_{K2} > Q_{K1}$, $Q_{Na2} > Q_{Na1}$). However, the yield of ion insertion into larger TCNQ nanoparticles is less than that into smaller TCNQ nanoparticles ($y_{K2} < y_{K1}$, $y_{Na2} < y_{Na1}$). The sodium insertion occurs a higher extent than potassium insertion under the same conditions ($y_{Na1} > y_{K1}, y_{Na2} > y_{K2}$) possibly due to the smaller radius of sodium ion. For both potassium and sodium insertion, partial rather than complete ion insertion is found which may reflect the formation of a layer of solid $TCNQ^{\bullet-}A^+$ ($A^+ = K^+$ or Na^+) on the surface of TCNQ nanoparticles, the thickness of which for potassium insertion t_K can be estimated to be 7.1 nm (t_{K1}) and 8.0 nm (t_{K2}), respectively for 71 nm and 116 nm nanoparticles, and for sodium insertion t_{Na} to be 9.8 nm (t_{Na1}) and 10.0 nm (t_{Na2}) into 71 nm and 116 nm TCNQ NPs, according to Equation 8.4, assuming a perfect core-shell structure.

$$t = R_{np} - \sqrt[3]{\frac{3M(Q_i - Q_r)}{4nF\pi\rho}} \qquad \text{(Eqn 8.4)}$$

where t is the thickness of ion insertion of TCNQ nanoparticles, R_{np} is the radius of TCNQ nanoparticles, Q_i is the ideal charge, Q_r is the actual charge resulting from ion insertion, M is the molar mass of TCNQ, ρ is the density of TCNQ and F is the Faraday constant. The parameter n is the number of electrons transferred for ion insertion of TCNQ (n = 1).

The similar thickness t ($t_{K1} \approx t_{K2}$) for potassium or sodium insertion ($t_{Na1} \approx t_{Na2}$) into different sizes of nanoparticles indicates that the formed shell during ion insertion is largely independent on the particle size, while the thicker layer ($t_{Na} > t_K$) formed by sodium ion insertion than potassium ion insertion suggests that the ion insertion thickness

is related to the cation type which may be attributed to a higher diffusivity of sodium ions into TCNQ nanoparticles. Here we propose a thin layer limiting mechanism for ion insertion of single TCNQ nanoparticles, where a thin shell of Na^+/K^+ $TCNQ^{\bullet -}$ is formed during ion insertion and this thin layer of solid $TCNQ^{\bullet -}$ A^+ (A^+: Na^+/K^+) in turn limits further ion insertion process. Notably, the size and cation dependent ion insertion into microcrystalized TCNQ NPs contracted with the full insertion seen into polymeric nanoparticles as discussed in Chapter 5 indicates that the structures of substrates into which ion were inserted plays an important role[9]. The strategy we describe here may also provide new quantitative information for the customised design and synthesis of desirable nanostructures.

8.4 Conclusions

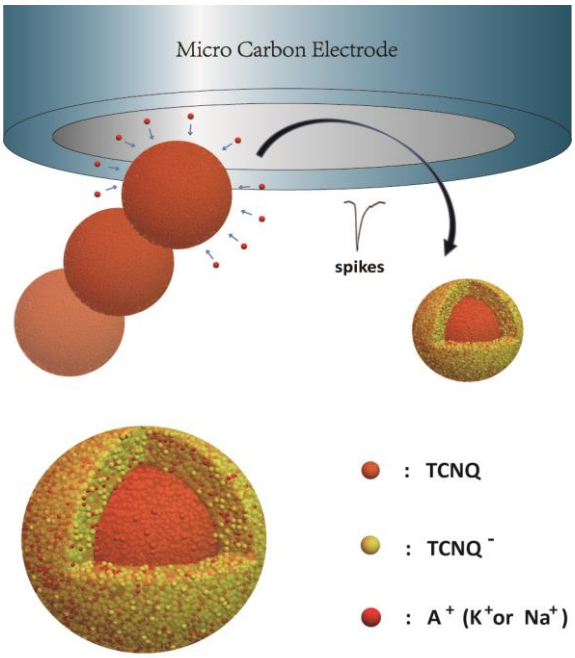


Figure 8.13 Schematic diagrams showing limiting potassium and sodium ion insertion into TCNQ nanoparticles in aqueous solution with formation of a thin shell of salt Na^+/K^+ $TCNQ^{\bullet -}$ on the surface of the nanoparticle

In this chapter, cation insertion into individual nanoparticles was observed, and the quantitative determination of the extent for cation insertion into single nanoparticles demonstrated. The extent of insertion is inferred to be limited and controlled by the formation of a thin shell of salt, Na^+/K^+ $TCNQ^{\cdot -}$ formed on the surface of the nanoparticle as shown in Figure 8.13. Ion insertion thickness (t) of single nanoparticles is found to be not dependent on particle size but cation types, while the extent of ion insertion (y) is found to be quantitatively dependent on both particle size and the cation types.

The strategy we study here is general and can be applied to characterise cation/anion insertion into nanoparticles of all types and used to rationalise the molecular design of nanoparticles/nanostructured electrodes for improving ion insertion and subsequently the battery performance. In addition, we believe that the real-time characterisation of ion insertion into single nanoparticles may provide a completely new insight into quantitatively tracking the fast-charge and -discharge of single individual nanoparticles for searching and selecting new nanomaterials for wide energy applications.

References

1. Q. Zhang, E. Uchaker, S. L. Candelaria and G. Cao, *Chemical Society Reviews*, 2013, **42**, 3127-3171.
2. P. Simon and Y. Gogotsi, *Nature Materials*, 2008, **7**, 845-854.
3. C. Rao and K. Biswas, *Annual Review of Analytical Chemistry*, 2009, **2**, 435-462.
4. V. Etacheri, G. A. Seisenbaeva, J. Caruthers, G. Daniel, J.-M. Nedelec, V. G. Kessler and V. G. Pol, *Advanced Energy Materials*, 2015, **5**, 1401289-1401297.
5. B. Genorio, K. Pirnat, R. Cerc-Korosec, R. Dominko and M. Gaberscek, *Angewandte Chemie International Edition*, 2010, **49**, 7222-7224.
6. N. Yabuuchi, K. Kubota, M. Dahbi and S. Komaba, *Chemical Reviews*, 2014, **114**, 11636-11682.
7. C. D. Wessells, S. V. Peddada, R. A. Huggins and Y. Cui, *Nano Letters*, 2011, **11**, 5421-5425.
8. S. C. Jung, H. J. Kim, J. W. Choi and Y. K. Han, *Nano Letters*, 2014, **14**, 6559-6563.
9. C. Wang, Y. Xu, Y. Fang, M. Zhou, L. Liang, S. Singh, H. Zhao, A. Schober and Y. Lei, *Journal of the American Chemical Society*, 2015, **137**, 3124-3130.
10. Y. G. Zhou, N. V. Rees and R. G. Compton, *Angewandte Chemie International Edition*, 2011, **50**, 4219-4221.
11. E. J. Stuart, K. Tschulik, C. Batchelor-McAuley and R. G. Compton, *ACS Nano*, 2014, **8**, 7648-7654.
12. W. Cheng and R. G. Compton, *Trends in Analytical Chemistry*, 2014, **58**, 79-89.
13. M. Pumera, *ACS Nano*, 2014, **8**, 7555-7558.
14. N. V. Rees, *Electrochemistry Communications*, 2014, **43**, 83-86.

15. X. Xiao and A. J. Bard, *Journal of the American Chemical Society*, 2007, **129**, 9610-9612.

16. X. Xiao, F. R. F. Fan, J. Zhou and A. J. Bard, *Journal of the American Chemical Society*, 2008, **130**, 16669-16677.

17. A. J. Bard, H. Zhou and S. J. Kwon, *Israel Journal of Chemistry*, 2010, **50**, 267-276.

18. R. Dasari, D. A. Robinson and K. J. Stevenson, *Journal of the American Chemical Society*, 2013, **135**, 570-573.

19. S. E. Fosdick, M. J. Anderson, E. G. Nettleton and R. M. Crooks, *Journal of the American Chemical Society*, 2013, **135**, 5994-5997.

20. W. Cheng and R. G. Compton, *Angewandte Chemie International Edition*, 2015, **54**, 7082-7085.

21. H. Alves, A. S. Molinari, H. Xie and A. F. Morpurgo, *Nature Materials*, 2008, **7**, 574-580.

22. R. Precht, R. Hausbrand and W. Jaegermann, *Physical Chemistry Chemical Physics*, 2015, **17**, 6588-6596.

23. T. J. Wooster, A. M. Bond and M. J. Honeychurch, *Analytical Chemistry*, 2003, **75**, 586-592.

24. T. J. Wooster and A. M. Bond, *Analyst*, 2003, **128**, 1386-1390.

25. J. Xiao, Z. Yin, Y. Wu, J. Guo, Y. Cheng, H. Li, Y. Huang, Q. Zhang, J. Ma, F. Boey, H. Zhang and Q. Zhang, *Small*, 2011, **7**, 1242-1246.

26. J. Xiao, Z. Yin, H. Li, Q. Zhang, F. Boey, H. Zhang and Q. Zhang, *Journal of the American Chemical Society*, 2010, **132**, 6926-6928.

27. G. Zhao, T. Ishizaka, H. Kasai, H. Oikawa and H. Nakanishi, *Chemistry of Materials*, 2007, **19**, 1901-1905.

28. M. F. Suárez, A. M. Bond and R. G. Compton, *Journal of Solid State Electrochemistry*, 1999, **4**, 24-33.

29. A. M. Bond, S. Fletcher, F. Marken, S. J. Shaw and P. G. Symons, *Journal of the Chemical Society, Faraday Transactions*, 1996, **92**, 3925-3933.

30. S. J. Cloake, H. S. Toh, P. T. Lee, C. Salter, C. Johnston and R. G. Compton, *ChemistryOpen*, 2015, **4**, 22-26.

31. T. J. Davies, C. E. Banks and R. G. Compton, *Journal of Solid State Electrochemistry*, 2005, **9**, 797-808.

32. S. V. Sokolov, C. Batchelor-McAuley, K. Tschulik, S. Fletcher and R. G. Compton, *Chemistry-A European Journal*, 2015, **21**, 10741-10746.

Chapter 9

Overall Conclusions

This thesis has presented the experimental work for the detection and characterization of organic nanoparticles by electrochemical methodologies. The investigation showed great promise for the efficient detection and quantification of individual organic nanoparticle properties such as size, concentration, and aggregation/agglomeration state, the surface structure and kinetics of individual nanoparticles and chemical reactions at the nanoscale involving nanoparticles as a mediator.

A variety of organic nanoparticles with different size were synthesized by reprecipitation method. The detection of organic nanoparticles is demonstrated via two main electrochemical methods: stripping voltammetry and "nano-impacts". Stripping voltammetry is employed to quantify the number of electrons transferred and oxidative/reductive potential required for the organic nanoparticle oxidation/reduction while the novel "nano-impacts" method is applied to characterize single organic nanoparticles. First, we use the direct "nano-impacts" method to study the synthesized indigo nanoparticles, showing novelly that individual monomeric organic nanoparticles can be electrochemically sized during their reduction. Next, the complete oxidative doping of polymeric organic nanoparticles (PVK) was shown in aqueous solution by the "nano-impacts" method, giving the doping yield from single organic nanoparticles. The "stick and strip" method was also carried out, showing that polymeric nanoparticles in aqueous solution can be immobilized, pre-concentrated and quantified. To further confirm the application of "nano-impacts" for electrochemical sizing, bifunctional organic

nanoparticles (OBD) were next detected. Both reductive and oxidative results lead to a size distribution in good agreement with dynamic light scattering (DLS) measurements. Then, the contrasts for electron transfer to single organic nanoparticles and ensembles of nanoparticles were investigated. Both stripping voltammetry and "nano-impacts" were conducted indicating the size of DPPH nanoparticles from complete oxidation and a core-shell structure from partial reduction of DPPH nanoparticles. Finally, we applied the "nano-impacts" method to ion insertion into individual TCNQ nanoparticles, demonstrating a quantitative determination of the extent for cation insertion into single organic nanoparticles. The insertion process is inferred to be limited and controlled by the formation of a thin shell salt at the surface of the TCNQ nanoparticles.

Overall, we began and developed the application of the "nano-impacts" method for the detection of the organic nanoparticles. The achievements in this thesis make a significant contribution to the applications of electrochemical techniques in characterization of various organic nanoparticles.